NEW MODALITIES FOR STRAIN ENGINEERING OF LEAD-FREE PEROVSKITE FERROELECTRIC THIN FILMS

BY

ANOOP RAMA DAMODARAN

DISSERTATION

Submitted in partial fulfillment of the requirements
for the degree of Doctor of Philosophy in Materials Science and Engineering
in the Graduate College of the
University of Illinois at Urbana-Champaign, 2014

Urbana, Illinois

Doctoral Committee:

Professor Lane W. Martin, Chair
Professor David G. Cahill
Professor Jian-Min Zuo
Professor Lance Cooper

ABSTRACT

Over the last few decades, considerable attention has been given to the development of lead-based ferroelectric systems such as $PbZr_{1-x}Ti_xO_3$ due to their robust high temperature ferroelectric properties, as well as the presence of the so-called morphotropic phase boundary (MPB) – a temperature-independent composition-driven structural instability that results in superior dielectric and piezoelectric properties. However, increasing environmental concerns are driving efforts towards the development of lead-free ferroelectrics such as $BiFeO_3$, $BaTiO_3$, and others. Previous work on epitaxial $BiFeO_3$ thin films have shown that large compressive strains can drive the formation of complex mixed-phase structures with enhanced electromechanical responses (4-5% strains). In this work, we probe the nanoscale distribution of phases present in these mixed-phase structures using a combination of epitaxial thin-film growth and characterization techniques such as x-ray diffraction and piezoresponse force microscopy. We show, for the first time, the presence of monoclinic distortions and intermediate phases (akin to conventional MPB systems) in the mixed-phase films that are crucial for enhanced electromechanical responses. We then present thickness- and temperature- dependent phase-evolution studies that indicate the presence of a strain-spinodal between the various structural polymorphs of $BiFeO_3$ to be the origin of mixed-phase formation. Finally, we discuss limitations due to a breakdown in epitaxy that occurs in thicker films and present chemical alloying-based approaches to mitigate these challenges. Having highlighted strain relaxation with increasing film thickness as a fundamental limitation to epitaxial-strain control, we explore an alternative route involving the use of a combination of defect-engineering and epitaxial strain to stabilize enhanced deformation states in materials. For this, we present a systematic study of $BaTiO_3$ thin films, and show that epitaxial strain can be used to control the ordering of growth-induced defects driving deterministic additional out-of-plane strains that can enhance the ferroelectric Curie temperature to values exceeding 800°C without any need to change substrates. Such a combined control of epitaxial strain and engineered defect-structures provides a new pathway to extend the limits of strain-control of materials and properties. Lastly, we investigate a new route involving the use of epitaxial strain in conjunction with controlled composition- and strain- gradients to tune the thermal stability of dielectric responses of ferroelectric thin films. We present preliminary studies that reveal enhanced relative dielectric permittivity values of ~750, that change by less than 10% over a wide temperature range from 25-350ºC in compositionally-

graded epitaxial $Ba_xSr_{1-x}TiO_3$ thin films, which is promising for next-generation microwave applications.

To Accha, Amma, Deepu Etta and Ambika

ACKNOWLEDGEMENTS

There are many people without whom this thesis research would not have been possible. First and foremost, I would like to thank Professor Lane W. Martin for his guidance throughout the years, and for challenging me and providing me with such a great environment to work in. I would also like to thank my committee members, Dr. David G. Cahill, Dr. Jian-Min Zuo, and Dr. Lance Cooper for their advice. Special thanks to Dr. Pascal Bellon, who was always there to advise me and help me out both personally and professionally.

I am greatly indebted to the Army Research Office for funding the work presented in this thesis and the Department of Materials Science for providing me financial assistance through teaching assistantship and travel awards. The staff at CMM and MRL Microfab has been an invaluable resource throughout my graduate career. I especially want to thank Dr. Scott McLaren, Dr. Mauro Sardela, Dr. Rick Hasch and Doug Jeffers for their advice, expertise, and enthusiasm. I am grateful to the organizers of the MRS and the Physics of Ferroelectrics meetings for providing me a platform to present my work and interact with a broader research community.

I have had the privilege of working with an exceptional group of colleagues at MRL. I wish to thank the multitude of graduate students, post-docs and undergraduates whom I have worked with directly on these and other projects including: Karthik, Sungki, Eric, Brent, Vengadesh, Ruijuan, Shishir, Ran, Liv, Josh, Jialan, Jarret, Zuhuang, Chen-Wei, Christoph, Zachary, Justin, Amber, Jay, Gabe and Issac. I have also thoroughly enjoyed working with many excellent collaborators including Bikram and Rich.

Thanks to my friends Shankar, Bharat, Martin, Sonal, Tomasz, and Vesna who have made the grad school experience so much fun. Thank you for all your encouragement and all the great memories.

Finally, I would like to thank my parents and my brother for their support, and strength. I would like to especially thank my wife, Ambika, who has been a constant support throughout my graduate life and without whom I could not have completed this degree.

TABLE OF CONTENTS

LIST OF ABBREVIATIONS

AFM	Atomic force microscopy
BST	$Ba_xSr_{1-x}TiO_3$
DRAM	Dynamic random access memory
EPR	Electron paramagnetic resonance
GLD	Ginzburg-Landau-Devonshire
IP	In-plane
KDP	Potassium dihydrogen phosphate
MBE	Molecular beam epitaxy
MEMS	Micro-electro-mechanical systems
MIT	Metal-insulator-transition
MLCC	Multilayer ceramic capacitors
MOCVD	Metal-organic chemical vapor deposition
MPB	Morphotropic phase boundary
OOP	Out-of-plane
PFM	Piezoresponse force microscopy
PLD	Pulsed laser deposition
PMN-PT	$(1-x)Pb(Mg_{1/3}Nb_{2/3})O_3$-$xPbTiO_3$
PTC	Positive temperature coefficient
PZT	$PbZr_xTi_{1-x}O_3$
RBS	Rutherford backscattering spectrometry
RHEED	Reflection high-energy electron diffraction
RMS	Root mean square
RSM	Reciprocal space map
SEM	Scanning electron microscopy
SPM	Scanning probe microscopy
TDTR	Time-domain thermoreflectance
XPS	X-ray photoelectron spectroscopy
XRD	X-ray diffraction

LIST OF SYMBOLS

P	Spontaneous polarization
T_c	Curie temperature
P_r	Remnant polarization
E	Electric field
F	Free energy
a_{ijk}	Dielectric stiffness
ε_o	Permittivity of vacuum
ε_r	Relative dielectric permittivity
C	Curie-Weiss constant
θ	Curie-Weiss temperature
a_{sub}	Pseudocubic in-plane lattice parameter of the substrate
a_{pc}	Pseudocubic lattice parameter of the film
Q_{ij}	Electrostrictive constants
T	Temperature
σ	Stress
ε_{ij}	Coefficient of dielectric permittivity tensor
π_i	Pyroelectric coefficient
d_{ijk}	Piezoelectric coefficient
t	Film thickness
λ	Wavelength
I	Current
V	Voltage
f	Lattice misfit
u_m	Misfit strain
t_c	Critical thickness
S_{ij}	Elastic compliance

G_γ	Free energy contribution from composition-gradients
G_f	Flexoelectric energy
γ	Phenomenological coefficient for composition-gradients
f_{ij}	Flexoelectric coefficient
G_D	Depolarization energy
E_D	Depolarization field
ε_b	Background permittivity

CHAPTER 1

FERROELECTRIC PEROVSKITES: PHYSICS, MATERIALS AND PROPERTIES

In this chapter, we begin with a review of the basic concepts of ferroelectricity and provide an overview of the technological significance of these materials. This is followed by a discussion of prototypical perovskite ferroelectric systems along with conventional materials design strategies to tune and maximize their responses. While lead-based perovskites dominate the current market of ferroelectric devices, we highlight the need to develop lead-free alternatives, especially in the thin film form, that would enable a seamless integration of these technologies in next-generation devices. This naturally, leads to a discussion of the current state-of-art in ferroelectric thin-film growth and concepts of epitaxy and strain-engineering which have been widely utilized as an additional knob to control structure and responses of these materials. Lastly, having discussed the merits and limitations of current strain-engineering based approaches, I will motivate the need to develop new modalities in material growth and design that can extend the limits of strain-engineering in these materials and develop the central focus of the rest of the thesis. The chapter concludes with a summary of the organization of the remainder of the thesis.

1.1 Introduction

Ferroelectric materials are crucial for a wide array of technologies and form an active element in applications ranging from relatively simple devices such as piezoelectric gas igniters and airbag sensors in cars, to advanced technologies including sonar and radar, ultrasonic medical imaging, ferroelectric memory, infrared imaging, waste heat harvesting and more [1,2,3,4,5,6]. A ferroelectric is defined as an insulating system with two or more discrete stable or metastable states of different non-zero electric polarization (*P*, referred to as the spontaneous polarization) under zero applied electric field [7,8,9,10]. These materials are characterized by a phase transition temperature, referred to as the ferroelectric Curie temperature (T_C), at which they undergo a structural transition from a high symmetry paraelectric phase to a lower symmetry ferroelectric phase. This phase transition is caused by a relative displacement of cations and anions in each of the crystal unit cells, that in turn, results in the formation of an intrinsic spontaneous polarization and the simultaneous emergence of the property of pyroelectricity (temperature dependence of spontaneous polarization) [11]. In the low-temperature phase, ferroelectric crystals belong to one of the polar symmetry groups, which are non-centrosymmetric and therefore display piezoelectricity (deformation under the action of electric fields and vice versa) [9,12]. Ferroelectric materials are thus, simultaneously piezoelectric and pyroelectric, and it is such multi-functionality that has led to the technological significance of this class of materials. In the following sections, we will briefly review various concepts related to ferroelectricity in materials, and then examine the range of physical properties that make ferroelectrics attractive for such a wide array of applications. At the same time, we will also discuss various materials engineering strategies that have been widely used to modify and control ferroelectric properties that are important for application-specific optimization of functionalities in these materials [13].

1.2 Ferroelectrics and Related Concepts

The defining feature of a ferroelectric is the presence of a switchable spontaneous electric polarization that is intrinsic to the crystal lattice. This imposes constraints involving the simultaneous presence of non-centrosymmetry and a polar axis on the point-group symmetry of these materials. Of the 32-possible crystal classes, 20 are piezoelectric (non-centrosymmetric materials that can be polarized under stress). Of these 20 piezoelectric crystal classes, 10 are pyroelectric (possess a polar axis with a spontaneous polarization that is temperature dependent)

[9,12]. Ferroelectrics are a subset of the 10 pyroelectric crystal classes in that they require the additional characteristic that the electric polarization can be switched between two or more energetically degenerate states by the application of an external electric field [5,7,8,10]. In the absence of such an electric field, the ferroelectric can exist in any of these states, including the possibility that the crystal can split into multiple regions known as domains, where neighboring domains possess different directions for the direction of the vector or spontaneous polarization [11,14]. The experimental proof of ferroelectricity is very often provided in the form of the polarization-electric field (*P-E*) hysteresis loop, a plot of the integrated switching current as a function of applied electric field, which demonstrates the hysteretic and saturation behavior associated with switching between the different domain states (Fig. 1.1). Point A in the figure describes a state characterized by equal fractions of oppositely polarized domains resulting in a system with a net zero macroscopic polarization. The application of an external electric field, energetically favors domains that have a parallel alignment of the spontaneous polarization. Consequently, as the external field is linearly increased the domain walls (regions between

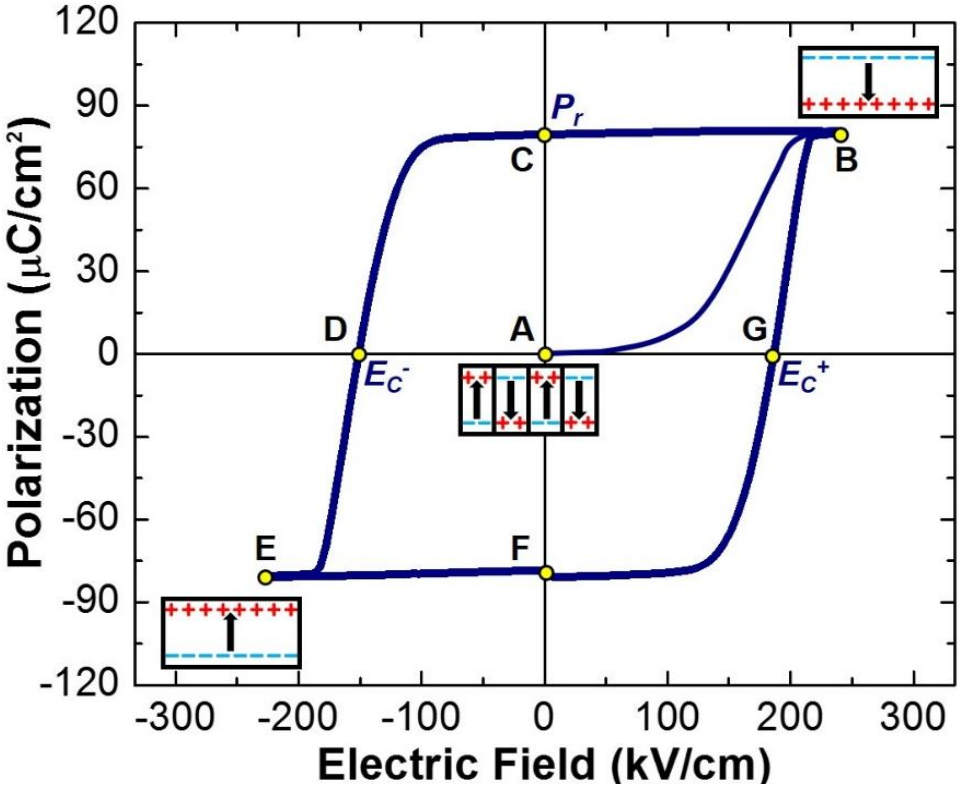

Fig. 1.1: A typical ferroelectric hysteresis loop of polarization *vs* applied electric field showing the poling process from a poly-domain state with net-zero macroscopic polarization (point A) to a poled monodomain state with downward pointing polarization (point B). Subsequent cycling of electric field to values in excess of the coercive fields (E_C, points D and G) results in a hysteretic switching between states with downward- and upward- pointing polarization (points B and E respectively) with a remnant polarization (P_r, points C and F).

adjacent domains) move to redistribute the volume fractions of domains in favor of the energetically favorable domain configuration to eventually yield a monodomain state (point B) [11,14]. Such a process of obtaining a monodomain state is termed as "poling" and the ferroelectric remains in this monodomain state even on the removal of the external field (point C). Now, in order to switch to a completely upward pointing monodomain state, an electric field in the reverse direction exceeding the coercive field (point D) needs to be applied. By traversing the hysteretic path B-C-D-E-F-G, the ferroelectric can be cyclically switched between downward and upward pointing polarization states, and forms the basis of switching-based devices including ferroelectric memory (or FeRAM) where bits of information can be stored as the polarization direction in a ferroelectric capacitor [15,16].

In addition to polarization-switching and the associated highly non-linear hysteretic response of ferroelectrics at high electric fields, there also exists strong thermo-electro-mechanical coupling in these materials resulting in a range of interesting functionalities that are summarized here (Fig. 1.2). Of these susceptibilities, we will primarily focus on the dependence of the spontaneous polarization of ferroelectric materials to electric field (E), temperature (T) and mechanical stresses (σ) that result in large values of linear (small signal) susceptibilities which are characterized by the dielectric, pyroelectric, and piezoelectric coefficients, respectively as [7,9,17],

$$\varepsilon_{ij} = \frac{\delta P_i}{\delta E_j}, \pi_i = \frac{\delta P_i}{\delta T},$$

$$d_{ijk} = \frac{\delta P_i}{\delta \sigma_{jk}} \quad (1.1)$$

where, ε_{ij} are coefficients of the dielectric permittivity tensor, π_i are the pyroelectric coefficients, and d_{ijk} are the piezoelectric coefficients. In addition to the intrinsic lattice contribution to susceptibilities, extrinsic

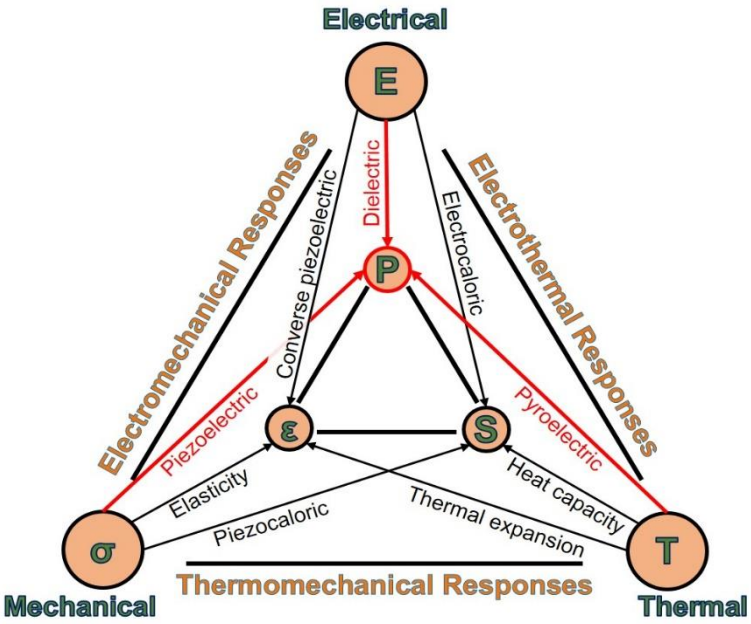

Fig. 1.2: Schematic indicating the range of thermo-electro-mechanical coupling effects in ferroelectric materials. The response of the ferroelectric polarization (P) to thermal, electrical and mechanical stimuli are highlighted in red. (Adapted from J. F. Nye *Physical Properties of Crystals*, 1964)

contributions such as those from domain-wall motion and others are also possible in these materials [18]. These susceptibilities are generally maximized near structural or polar instabilities (such as near T_C) and form the basis of a variety of devices including high-k dielectric capacitors, piezoelectric transducers, and temperature sensing elements [8,13]. In the sections that follow we will look closely at the perovskite family of ferroelectric materials to have a better understanding of these instabilities and ways to engineer optimized responses at the operating conditions of temperature, stress, and electric fields in real devices.

1.3 Bulk Perovskite Ferroelectrics

While ferroelectricity was first discovered in the 1920's in hydrogen bonded materials such as Rochelle salt and subsequently potassium dihydrogen phosphate (KDP) [19,20,21], it was only in the early 1940's with the discovery of above room-temperature ferroelectricity in $BaTiO_3$, a perovskite ceramic with excellent chemical and structural robustness, that the field of ferroelectrics transformed from a subject of mere scientific curiosity to one of immense technological significance [22]. Since then many hundreds of ceramic ferroelectric materials have been discovered and have been categorized based on their unit cell structure as (1) the tungsten-bronze group, (2) the oxygen octahedral or the perovskite group, (3) the pyrochlore group, and (4) the bismuth layer structure group [4]. Nevertheless, the perovskite-based ferroelectric materials are still the most widely used and form the bulk of ferroelectric ceramics manufactured in the world today [4,5,13].

1.3.1 Structure and Phase Transitions

Ferroelectrics perovskites are a subtype of a broader range of compounds possessing the perovskite structure with the chemical formula ABO_3, where *A* and *B* each represent a cation element or a mixture of two or more elements or vacancies. Depending on the composition and cationic ordering, perovskites can be metallic or insulating, can exhibit many different types of magnetic and structural order including (anti-)ferromagnetism [23], colossal magnetoresistance [24], high-temperature superconductivity [25], and more. Prototypical examples of ferroelectric perovskites include simple compounds such as $BaTiO_3$, $PbTiO_3$, $BiFeO_3$, $KNbO_3$ as well as solid solutions including $PbZr_xTi_{1-x}O_3$ (PZT), $Ba_xSr_{1-x}TiO_3$ (BST), $(1-x)Pb(Mg_{1/3}Nb_{2/3})O_3$-$xPbTiO_3$ (PMN-PT), etc. The simplest arrangement of a perovskite structure is based on corner linked oxygen octahedra arranged in a regular cubic array to form the high symmetry *m*3*m* structure (very

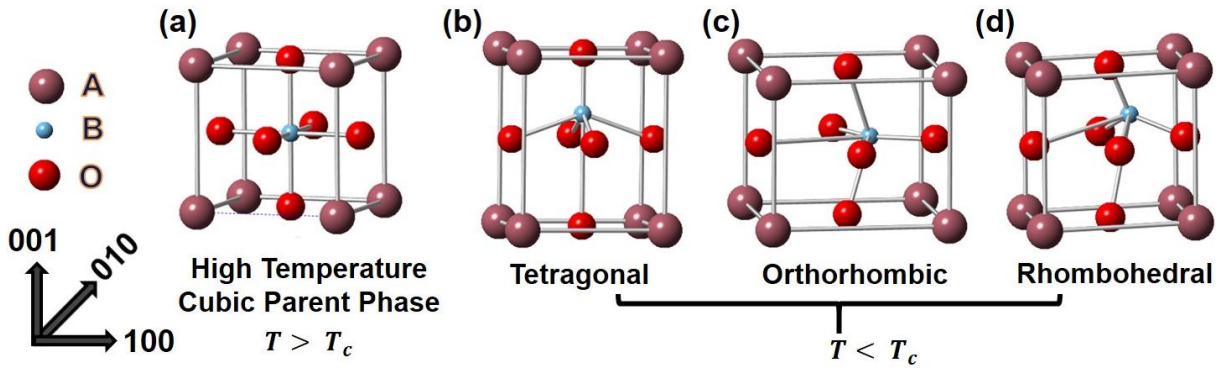

Fig. 1.3: Cartoon depiction of the crystal structure of typical polymorphic states of a ferroelectric perovskite including a) Ideal perovskite structure (cubic paraelectric parent phase), b) tetragonal phase with polarization along [001] direction, c) orthorhombic phase with polarization along [110] direction, and d) rhombohedral phase with polarization along [001] direction.

often the reference high temperature paraelectric phase of many perovskite ferroelectrics (Fig. 1.3a)). The small 6-fold coordinated *B* site cation in the center of the octahedron is filled by a small highly charged (tri-, tetra-, penta-, or hexa- valent) transition metal cation and the larger 12-fold coordinated "interstitial" site between the octahedra carries a larger mono-, di- or trivalent cation or is simply empty as in WO_3 [4,11,13]. In the case of ferroelectric perovskites, a structural phase transition from the parent high symmetry paraelectric phase to the ferroelectric phase with a lower symmetry distorted perovskite structure occurs upon cooling below the T_C and the material can exist is several polymorphic states. In bulk $BaTiO_3$, the paraelectric-to-ferroelectric transition occurs at 120°C, below which the cubic lattice (symmetry $Pm\bar{3}m$) is distorted and the crystal becomes tetragonal (symmetry $P4mm$). This transition is accompanied by the displacement of the central Ti cation relative to the oxygen octahedra along the four-fold axis and the development of spontaneous macroscopic polarization along the tetragonal *c* axis (Fig. 1.3b). Upon further cooling, the $BaTiO_3$ crystal demonstrates additional phase transitions to an orthorhombic phase (symmetry $mm2$) at 0°C with spontaneous polarization along the two-fold [110] (Fig. 1.3c). The final ferroelectric transition to a rhombohedral phase (symmetry $R3m$) occurs at -70°C with spontaneous polarization along the three-fold [111] (Fig. 1.3d). The ferroelectric phase transitions in bulk $BaTiO_3$ are of the first order and are accompanied by the release of latent heat and discontinuous changes in lattice parameters and unit cell volume (Fig. 1.4a, top panel). The ferroelectric susceptibilities at such first order transitions display large anomalies and are hysteretic (Fig. 1.4a, bottom panel) [9,11]. Furthermore, second order phase transitions (continuous transitions without any latent heat) are also possible in ferroelectric materials; and even larger anomalies in ferroelectric susceptibilities (theoretically infinity) are expected. In addition to temperature,

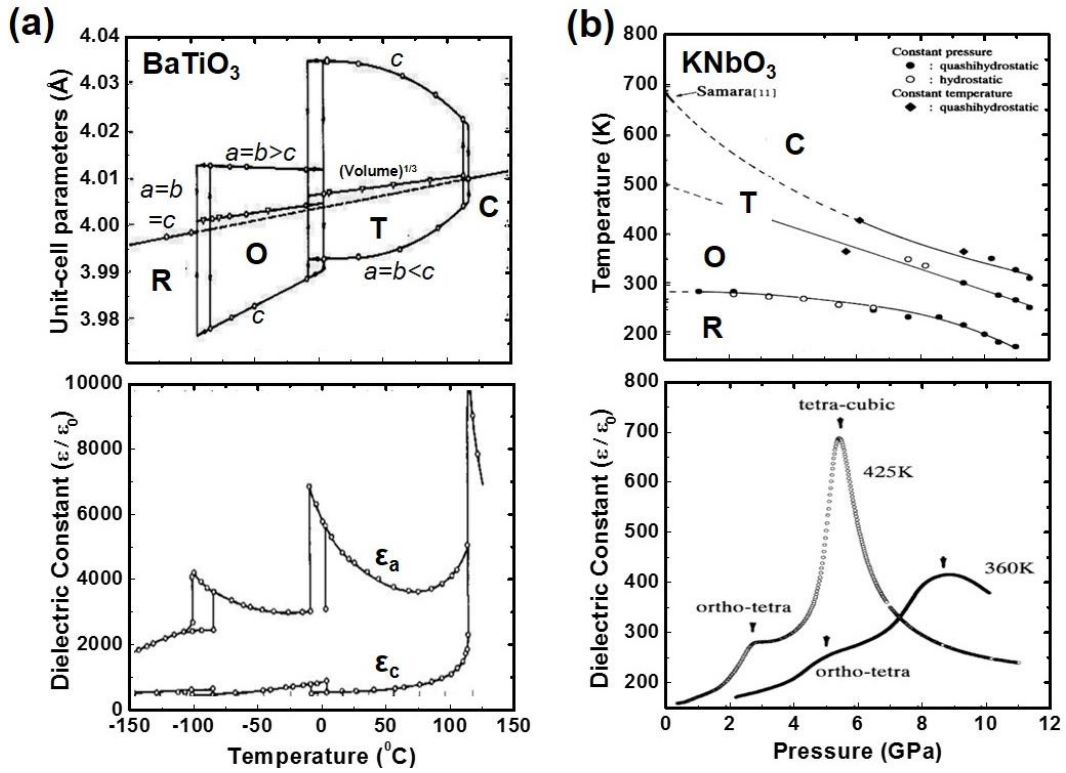

Fig. 1.4: a) Temperature dependent evolution of unit-cell lattice parameters and ferroelectric phase transitions (top panel) and associated dielectric response (bottom panel) in $BaTiO_3$ [9], and b) Temperature-pressure phase diagram (top panel) and pressure-dependent evolution of dielectric constant at representative temperatures of 360 and 425 K (bottom panel) for ferroelectric $KNbO_3$ [26]. C, T, O and R represent the cubic, tetragonal, orthorhombic and rhombohedral polymorphs respectively.

pressure can also be used to induce such structural instabilities. For instance, Fig. 1.4b (top panel) shows the temperature-pressure phase diagram of $KNbO_3$ (an orthorhombic ferroelectric at ambient conditions). In addition to a temperature-dependent ferroelectric transitions from cubic to tetragonal to orthorhombic to rhombohedral upon cooling, an identical sequence of ferroelectric transitions are observed with increasing hydrostatic pressure. The anomalies in the dielectric permittivity associated with these pressure-induced phase transitions are provided for two representative temperatures of 360K and 435K (Fig. 1.4b, bottom panel) [26]. In order to achieve such enhanced susceptibilities, routes to induce structural instabilities in the vicinity of operating conditions for real world applications have been developed. To understand these pathways, we begin by understanding the general mechanism for ferroelectricity in perovskite materials.

1.3.2 General Mechanism for Ferroelectricity in Perovskites

The sensitivity of ferroelectrics to temperature and pressure, as well as a range of other factors, arises from its origin as a delicate competition between long range Coulomb forces that

favor the ferroelectric state and short range repulsions that favor the non-polar cubic structure [27]. Detailed electronic-structure calculations have revealed that the mechanism for ferroelectricity in $BaTiO_3$ involves the ligand field stabilization of empty *d*-orbitals of B-site Ti cation by the completely filled O 2*p* orbitals, which is accompanied by the off-centering of the Ti cation [28]. These studies concluded that the mechanism of ferroelectricity in classic perovskite ferroelectrics such as $BaTiO_3$ and $PbTiO_3$ involves a weakening of the short range repulsive forces by hybridization between the unoccupied *d* states of the *B*-site transition metal cation with oxygen allowing for ferroelectric instability at lower pressures. Additionally, in the case of $PbTiO_3$, the Pb 6*s* and the O 2*p* states are also strongly hybridized leading to a large strain that stabilized the tetragonal ferroelectric state. Thus, in a manner similar to applied hydrostatic pressure, chemical substitutions (typically with isovalent cations of varying sizes) on the *A*- and *B*-sites of perovskite ferroelectrics give rise to so called "chemical pressure" and can be utilized to engineer structural instabilities and ferroelectric phase transitions. There are also alternative mechanisms to ferroelectricity in perovskite materials such as $BiFeO_3$ that possess non-d^0 *B*-site cations, and typically involves the steriochemical activity of lone pair electrons on *A*-site cations (such as Pb^{2+}, Sn^{2+}, Bi^{3+}) with ns^2 electron configurations [29]. It has also been shown that for such non-d^0 B-site ferroelectric perovskites the ferroelectric state is relatively insensitive to strain [30].

1.3.3 Chemical Tuning of Ferroelectric Susceptibilities

We have, so far, seen that temperature, pressure, and composition are three important knobs that can be used to tune the polymorphic state of a ferroelectric material and that ferroelectric susceptibilities are often maximized in the vicinity of structural instabilities. While the temperature and pressure conditions are determined by the operating conditions for a given application, researchers have primarily resorted to tuning the composition or the so called "chemical pressure" to maximize ferroelectric responses in materials. Over the decades, researchers have exploited the flexibility of chemical modifications in perovskites and a whole array of compounds based on ferroelectric solid solutions, including BST, PZT, PMN-PT, and others, have been developed. These ferroelectric solid solutions are extensively used in a wide range of applications from high dielectric-constant capacitors, piezoelectric sonar and ultrasonic transducer, radio and communication filters, infrared image sensors and more [1,4,13,18]. For instance, alloying the *A*-site of $BaTiO_3$ with increasing amounts of Sr^{2+} controllably decreases the unit cell volume and has the effect of increasing "chemical pressure" thereby allowing a continuous control of ferroelectric

T_C from that of bulk $BaTiO_3$ (T_C ~120 °C) all the way down to zero kelvin for $SrTiO_3$, an incipient ferroelectric [9,31]. Consequently, BST–based solid solutions are widely used for near-room temperature dielectric applications that require high dielectric permittivity and tunability [32].

The concept of "chemical pressure" has also been applied to develop optimized compositions of solid solutions of lead-based perovskites that display large piezoelectric and electromechanical coupling coefficients, and have entirely supplanted the use of its predecessors (based on bulk $BaTiO_3$ ceramics) for piezoelectric applications. State-of-the-art piezoelectrics are based on perovskite materials with complex chemistries including $Pb(Zr_{0.52}Ti_{0.48})O_3$ and $0.77Pb(Mg_{1/3}Nb_{2/3})O_3$-$0.33PbTiO_3$ [4,13,33]. The importance of these compositions can be understood by looking at the role of alloying at the *B*-site Ti^{4+} cation of $PbTiO_3$ with isovalent Zr^{4+} cations towards controlling the polymorphism displayed by the PZT family of ferroelectrics. The high temperature prototype phase in PZT is the cubic perovskite phase and at lower temperatures, they adopt many distorted versions of the parent phase depending on the composition and the temperature (Fig. 1.5, top panel) [33,34]. It is easily seen that Ti-rich compositions form a tetragonal ferroelectric (with the polarization along the pseudo-cubic [001] direction) and Zr-rich region condense into a rhombohedral ferroelectric (with the polarization along the pseudo-cubic [111]) [1]. While the largest ferroelectric polarization is displayed by pure $PbTiO_3$, it has been observed that the ferroelectric susceptibilities, including the dielectric constant, electromechanical coupling constants, and piezoelectric coefficients, vary as a function of composition across the phase diagram and are maximized at the boundary between the tetragonal and the rhombohedral phases (Fig. 1.5, bottom panel). This compositional boundary marks a region of

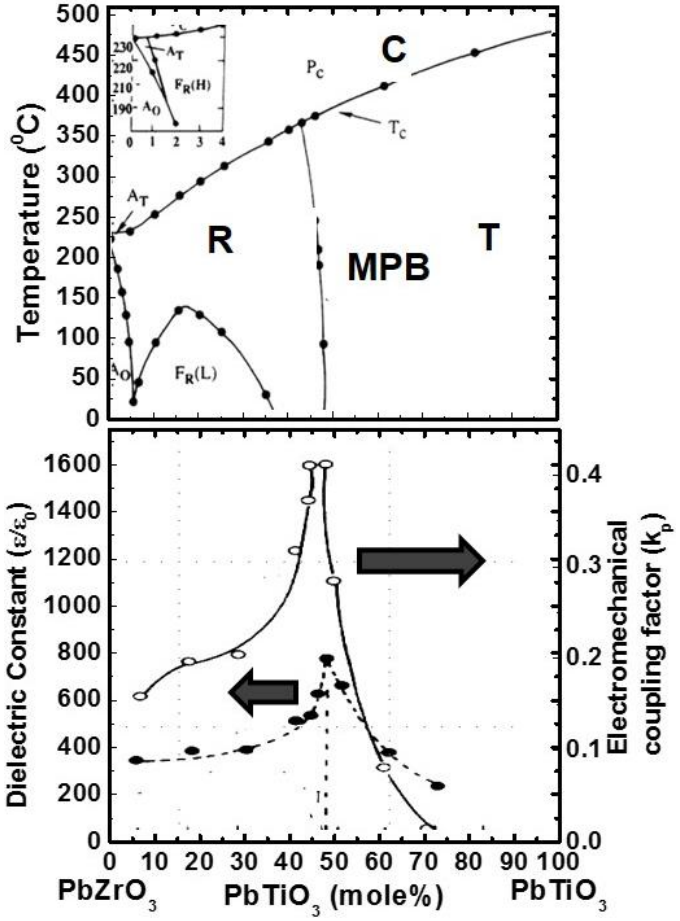

Fig. 1.5: Temperature-composition phase diagram (top panel) and the evolution of room-temperature dielectric response and electromechanical coupling factor (bottom panel) as a function of bulk PZT composition [1].

structural instability and thereby high susceptibilities that are temperature insensitive, and commonly referred to as the morphotropic phase boundary (MPB) [1,33,35,36]. It is now understood that the apparent continuous-phase transitions through the MPB region from tetragonal to rhombohedral (disallowed by symmetry), are mediated by intermediate phases of monoclinic symmetry [37,38], and that the high electromechanical response in this region is related polarization rotation mechanisms associated with this phase transition [39,40,41]. Furthermore, recent high-pressure studies on pure $PbTiO_3$ have revealed the presence of a rhombohedral phase at pressures exceeding 20GPa with intermediate MPB-like monoclinic phases that separate the tetragonal and rhombohedral phases in the intermediate-pressure regime of 10-20GPa [42]. These studies have led to the conclusion that the observation of MPB in solid solutions of $PbTiO_3$ is a manifestation of the high pressure-induced MPB of pure $PbTiO_3$ that has been tuned to exist at ambient pressure via chemical alloying (chemical pressure).

Over the last few decades, considerable effort has been focused on developing lead-based ferroelectrics with increasingly complex chemistries including the development of relaxor-single crystal ferroelectrics like PMN-PT ($PbMg_{1/3}Nb_{2/3}O_3$-$PbTiO_3$) that have 10 times the electromechanical coupling coefficients of PZT based compounds [43]. While ultrahigh performance piezoelectrics with increasingly complex chemistries have been developed to revolutionize applications, their synthesis has become increasingly challenging and requires complicated and expensive synthesis routes. At the same time, these compositions contain more than 60% weight lead and are a matter on environmental concern. Subsequently, there has been a concerted effort towards development of lead-free piezoceramics that not only display MPB-like features and associated highly enhanced piezoresponse, but can also be easily manufactured [44,45,46].

1.4 Thin-Film Ferroelectrics

Ferroelectrics in the thin-film form, on account of their nanoscale thickness and low power operation, are poised to replace their bulk counterparts in many modern ferroelectric applications [47]. While bulk ferroelectric perovskites (0.1-10 mm thick) have been extensively used as piezoelectric transducers and sensors for decades, their macroscopic dimensions and the requirement of enormous external switching voltages exceeding kilovolts make it impossible to integrate them as active elements in integrated circuits and micro-electro-mechanical systems (MEMS). The synthesis of ferroelectric materials in thin-film geometries has paved the way for

such an integration and has also provided a convenient platform for novel advanced applications including low power electron emission devices, electrocaloric cooling systems, phase-array radar, 3-D trenched capacitors for DRAM devices [5]. The epitaxial growth of ferroelectric thin films on lattice mismatched single-crystal substrates allow the use of epitaxial strain as an additional knob, apart from composition and akin to pressure, to engineer phase and domain structures of ferroelectric materials and provides an enormous phase space for materials design [48,49,50]. Modern thin-film growth technologies have paved way for the growth of high-quality ferroelectric thin films with unit cell control over film thickness as well as the synthesis of heterostructures and superlattices with atomically sharp interfaces. These developments have resulted in rapid advances in our understanding of the physics of ferroelectricity, including possibilities to artificially engineer ferroelectricity in materials at the nanoscale.

1.4.1 Ferroelectric Thin Film Growth

Researchers have been using a wide array of growth techniques including sputtering, metal-organic chemical vapor deposition (MOCVD), molecular beam epitaxy (MBE), and pulsed laser deposition (PLD) to synthesize epitaxial ferroelectric thin films. RF magnetron sputtering of oxide targets using pure oxygen or a mixture of oxygen and argon has been often used to synthesize thin films of a wide array of ferroelectric perovskites such as PZT, BST, and $BiFeO_3$ [15,16,51,52]. While sputtering processes provide advantages of uniform film growth over large areas and is suitable for large scale production, there exist several challenges associated with widely different sputtering yields of elemental species in the oxide target as well as the high density of bombardment-related defects that form in the films synthesized. MOCVD processes provide great flexibility for conformal growth of high quality, pin-hole free, stoichiometric epitaxial films of ferroelectric thin films over large areas and is preferred for large scale production [53,54]. The challenge, however, is the identification and careful tuning of metal-organic precursors chemistry, the need for complex gas handling systems with high levels of temperature control, and safety issues related to the toxicity of gas precursors that limits its use in a research environment. Researchers have therefore preferred MBE- and PLD- based growth techniques for the synthesis of complex oxide materials in the context of research and development [55,56,57,58]. MBE has been, for decades, the benchmark for high-precision growth and yields high-quality thin films with precise control of stoichiometry and thickness. In MBE growth of complex oxides, low energy (<1 eV) thermalized beams of constituent metal atoms are evaporated in a reactive environment of

ozone or atomic oxygen onto single crystal substrates held at elevated temperatures and UHV background pressures to give extremely pure and defect-free films. However, the high cost of a good MBE system (exceeding a million dollars), and the requirement for ultrapure material and UHV operation limits flexibility with regards to growth of different material systems that in the same chamber. PLD, on the other hand, is a very simple growth process, relatively inexpensive to set up. In PLD of complex oxides, a high power pulsed laser ablates a sintered ceramic or single crystal target in a reactive oxygen ambient with growth pressures as high as a few hundred millitorr. The high energy density of the incident laser vaporizes the target material to generate a plasma plume that condenses to form a film on a heated substrate that is held in the path of the plume. The highly energetic and far from equilibrium nature of the process is advantageous towards ensuring stoichiometric ablation of complex target compositions. Furthermore, one can grow multiple materials in the same PLD system by simply replacing targets, and, thus it is a high-throughput technique enabling the exploration and rapid prototyping of a wide array of material systems. The slow growth rate per pulse in tandem with advanced *in situ* growth metrology techniques such as reflection high-energy electron diffraction (RHEED) [59] has now made it possible to achieve unit-cell level thickness control of films making it possible to synthesize exotic artificial superlattice structures with atomically sharp interfaces. Thus, in spite of limitations with regards to the large area film uniformity and scalability of this technique, it is widely popular with researchers and has played a very important role in the discovery of novel functionalities in complex oxide materials. In the remainder of the thesis, we focus on the development of lead-free thin film ferroelectric materials and have employed the versatility of PLD growth to synthesize thin films of several materials including prototypical ferroelectrics as $BiFeO_3$ and $BaTiO_3$ as well as ferroelectric heterostructure devices with conducting perovskites metals such as $SrRuO_3$ and $La_{0.5}Sr_{0.5}CoO_3$ as top and bottom electrodes for ferroelectric measurements.

1.4.2 Strain Engineering in Ferroelectric Thin Films

High quality, epitaxial ferroelectric thin films on single-crystal substrates have been routinely synthesized using advanced thin film growth and *in situ* metrology capabilities that have developed over the last decade. The simplicity of the thin-film geometry has great advantages as compared to bulk, polycrystalline counterparts and has enabled a systematic study of intrinsic ferroelectric responses in materials at low voltages, as well as the effect of extrinsic factors including the presence of interfaces (*e.g.*, domain walls, surfaces, phase boundaries) and defects

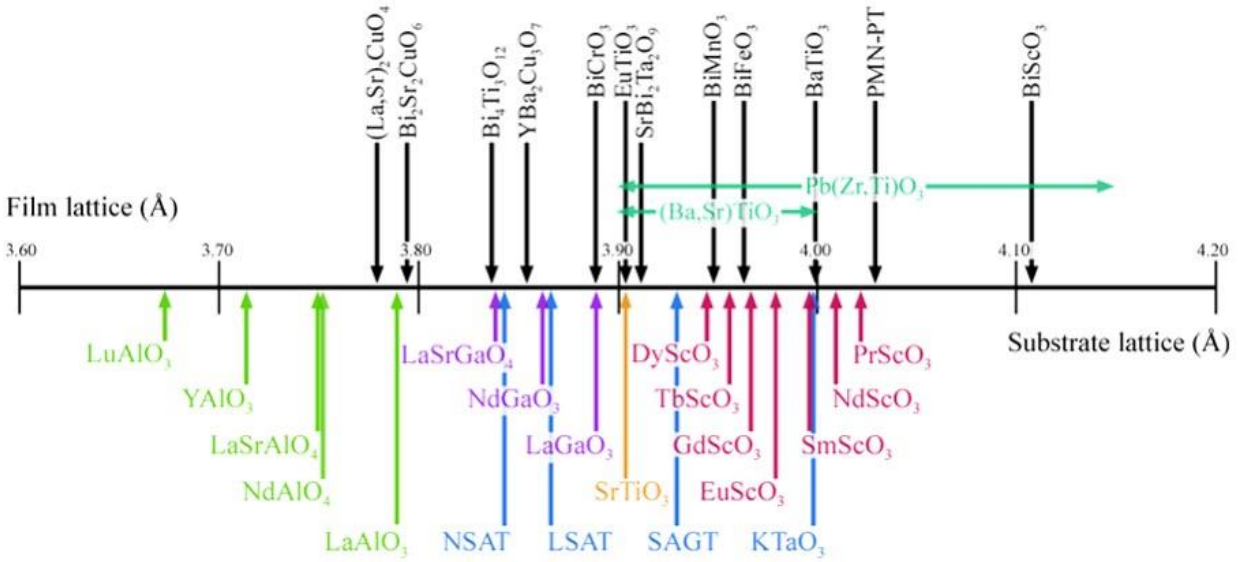

Fig. 1.6: A number line showing the pseudocubic *a*-axis lattice constants of some ferroelectrics and commercially available perovskite substrates for the growth of epitaxial thin films [50].

on ferroelectric properties. The most important advantage over bulk ferroelectrics, however, is the fact that substrate-induced epitaxial strain can be used to greatly modify the stability of ferroelectric polymorphs and thereby dramatically control and engineer the responses in these materials. Subsequently, a range of complex oxide substrates and buffer-layers of perovskite oxide metals have been developed to enable the synthesis of epitaxial ferroelectric capacitor heterostructures with substrate-induced compressive or tensile strains to values as high as a few percent for ferroelectric materials including PZT, BST and $BiFeO_3$ (Fig. 1.6) [50]. This has produced an array of spectacular results in the past decade such as strain induced enhancement of T_C in $BaTiO_3$ [60], strain induced ferroelectricity in $SrTiO_3$ [61], substrate vicinality and electrode control of domain morphologies [62], and even new strain-induced ferroelectric phases [63].

1.5 Statement of Thesis

Over the last few decades, considerable attention has been given to the utilization of high-performance and high-temperature compatible versions of the canonical ferroelectric system PZT, but growing concerns over the toxicity of lead are driving a rejuvenation of efforts towards the development of lead-free ferroelectrics such as $BiFeO_3$, $BaTiO_3$, and others. Towards this end, my work focuses on understanding and inventing new routes to enhance ferroelectric responses through strain control in epitaxial thin films of these lead-free materials. For this work, I have focussed on two prototypical ferroelectric lead-free perovskites: $BiFeO_3$ and $BaTiO_3$.

My interest in the $BiFeO_3$ system stems from recent work on $BiFeO_3$ that showed the formation of exotic structural polymorphs and complex mixed-phase structures with a highly enhanced electromechanical responses in highly compressively strained versions of this material [63]. The mixed-phase coexistence in these films are akin to those in MPB-compositions of lead-based ferroelectrics, with potentially similar mechanisms for the origin of these effects and the observed enhancement in responses. In order to optimize such strain-induced mixed phase formation in $BiFeO_3$ for advanced applications as well as identify other potential ferroelectric systems that can demonstrate such effects, it is necessary to understand the origin of these observations at the nanoscale. For this, I combined epitaxial thin-film growth and detailed investigations of the nanoscale structure and topography of these materials using temperature- and field-dependent high-resolution X-ray Diffraction (XRD) and scanning probe-based techniques. Based on these experiments, I was able to develop a complete picture of the distribution of various phases present in these complex mixed-phase structures as well as the reversible electric field-induced structural transformations that were responsible for the large electromechanical effects observed. I identified, for the first time, the presence of monoclinic distortions and intermediate phases necessary to allow such transformations that had not been previously observed. From there, I worked to understand the origins of mixed-phase formation by mapping out the nature of nanoscale phase separation in these films as a function of thickness and temperature that illuminated the presence of a strain-induced spinodal instability between the various structural polymorphs of $BiFeO_3$, and then explored doping-based routes to further enhance such effects in these materials. In all, my work has greatly advanced the understanding of these complex and technologically exciting structures present in highly strained $BiFeO_3$ thin films and has provided new strain-based pathways to engineer mixed phase structures and enhanced piezoresponses in thin film ferroelectrics.

The second half of my thesis focuses on new strain-based approaches to engineer ferroelectric responses in $BaTiO_3$ and BST-based thin films. Over the last decade, researchers have demonstrated that a few percent of epitaxial compressive strain can increase the T_C of $BaTiO_3$ by a few hundred degrees.[60] Such conventional epitaxial strain-based approaches, however, are limited by the magnitude of strain that can be applied and the thicknesses that can be achieved before film relaxation. To overcome these limitations, I have developed a new direction in epitaxial strain control involving the coupling between epitaxial strain and engineered defect-structures that

produce anisotropic lattice deformations and enhanced strain states in materials. My work suggests that epitaxial strain can be used to control the ordering of defect structures inducing deterministic additional out-of-plane strains that greatly enhance the T_C of $BaTiO_3$ thin films to temperatures as high as 800°C without any need to change substrates. This is especially exciting since this is achieved without any degradation of the polarization or leakage properties. This is made possible by new insights from my research that relates the energetics of the growth process to film chemistry, defect structures, and properties in materials. Such a combined control of epitaxial strain and engineered defect-structures to control ferroelectricity in materials opens up a new paradigm in strain control of materials and properties.

The final part of my thesis focusses on a novel combination of compressive epitaxial strain and a controlled composition-gradient across the thickness in BST thin films to engineer a state where the in-plane dimensions of the oxygen octahedra (responsible for ferroelectricity in these materials) are held constant by the substrate while the out-of-plane dimension is linearly tuned as a function of composition, thereby, creating an effective out-of-plane strain gradient and associated polarization gradient in the film. Here, we explore the possibility of using spatial gradients in composition and strain to engineer enhanced dielectric responses with excellent temperature stability over a wide temperature range for use in next-generation microwave devices. Preliminary measurements for the temperature-dependence of dielectric susceptibility for epitaxial monodomain graded-BST films grown on $GdScO_3$ (110) substrates with highly controlled composition- and strain- gradients have revealed high values of dielectric permittivity (ε_r ~750) that is stable over a wide temperature range (25-350°C). Furthermore, by comparing our measurements with those from advanced GLD-based models for graded ferroelectric films, we comment on the role of composition gradient, flexoelectric (strain-gradient) and depolarization effects that are important for the observed responses.

Overall, in my thesis I have explored three new modalities of strain engineering in ferroelectric thin films: 1) The use of strain to stabilize metastable phases and mixed phase structures for enhanced piezoresponse in ferroelectric materials, 2) The use of epitaxial strain to align engineered defects that result in additional anisotropic lattice deformation in the bulk of ferroelectric thin films resulting in highly enhanced strain states and property enhancements, and 3) A combination of epitaxial strain and composition-gradients to engineer enhanced dielectric

responses with excellent temperature stability that is required for next generation microwave applications.

1.6 Organization of Thesis

The remainder of this dissertation consists of six chapters, four appendices, and a section for references.

In Chapter 2, we explore the growth of two lead-free ferroelectrics, namely $BiFeO_3$ and $BaTiO_3$ on low lattice mismatched substrates using PLD. We present a detailed study of the growth optimization for the two ferroelectric thin film systems with regards to structure and film stoichiometry, and also introduce the basics of electrical, thermal and scanning probe-based measurements that have been employed in the rest of the thesis.

In Chapter 3, we experimentally investigate the intricate nanoscale spatial arrangement of metastable mixed-phase structures that form in highly compressively strained $BiFeO_3$ thin films *via* detailed characterization of the phase- and surface- structure of these films using a combination of high resolution XRD and scanning probe-based techniques. We also present bias-induced nanoscale swithching among the various phases present using piezoresponse force microscopy (PFM) that shed light on the mechanism for highly enhanced piezoresponses that have been reported in these films.

In Chapter 4, we provide detailed temperature- and thickness-dependent studies of the evolution of metastable phases in highly strained $BiFeO_3$ films to trace the origins of such complex mixed phase formation. We also present "chemical pressure" based alloying strategies that enable the stabilization of these technologically significant mixed phase structures with highly enhanced electromechanical responses to greater thicknesses.

In Chapter 5, we demonstrate a new route to engineering strain in materials involving the use of chemical strain from growth-induced defect dipoles in combination with substrate-induced compressive epitaxial strain to engineer tunable, high temperature ferroelectricity in $BaTiO_3$ thin films to temperatures exceeding 800°C. We also present detailed measurements of the effect of defect-related strain of the temperature-dependent evolution of ferroelectricity in these films and compare the results to predictions from phenomenological Ginzburg-Landau-Devonshire (GLD) models.

In Chapter 6, we utilize epitaxial strain in conjunction with a controlled gradient in chemical pressure (achieved by linearly varying the Ba:Sr ratio) across the thickness of BST films

to generate composition- and strain- gradients in these materials. We then investigate the role of gradient effects towards engineering enhanced dielectric responses that are stable over a wide temperature range, and also compare them with predictions from GLD-based models.

In Chapter 7, I summarize the findings of the work and outline future work that could be pursued after this thesis based on my overall findings.

The main text is supplemented by two Appendices that include additional and supporting details of the main text. Appendix A introduces the PFM technique, showing the experimental setup and procedure for imaging ferroelectric order in materials. Appendix B provides details of the GLD model utilized to study the role of defect-related strain in coherently strained epitaxial $BaTiO_3$ thin films.

CHAPTER 2

GROWTH AND CHARACTERIZATION OF LEAD-FREE FERROELECTRIC THIN FILMS USING PULSED LASER DEPOSITION

In this chapter, we begin with a discussion of the pulsed laser deposition process, followed by a brief description of the experimental setup and the growth parameters that were used to synthesize the various epitaxial thin-film heterostructures that have been studied in this dissertation. We explore two lead-free ferroelectric thin-film systems: $BiFeO_3$ (also a room temperature multiferroic) and $BaTiO_3$, as we study their structural, chemical, topographical, and ferroelectric properties for films grown on low misfit-strain substrates. We present a detailed study of the growth and characterization for the two ferroelectric thin-film systems with regards to structure and film stoichiometry, and also introduce the basics of electrical, thermal, and scanning probe-based measurements that have been employed in the rest of the thesis.

2.1 Introduction

In Chapter 1, we briefly reviewed various thin-film growth techniques that have been used in the synthesis of epitaxial complex oxide thin films. Of these, PLD has emerged as the technique of choice with several advantages related to the low set-up cost as well as the versatility it offers to synthesize a wide range of oxide material systems. It was the synthesis of high T_C superconductors *via* PLD in the late 1980's [64], followed by several pioneering works on oxide ferroelectrics [65,66] in the early 1990's that initially brought PLD growth to the mainstream. Since then, major advancements over the last few decades including the integration of *in situ* growth monitoring capabilities such as RHEED and others, has transformed PLD to a sophisticated thin-film growth technique that routinely enables the growth of high-quality epitaxial thin films with unit-cell level control of thickness, and even the growth artificial superlattices and nanostructures [55,57]. However, despite the relatively easy set-up for a PLD system, the actual growth involves highly energetic and complex processes including laser-ablation, plume formation and propagation, plasma chemistry, as well as the out-of-equilibrium thin-film growth process that occurs at the substrate surface [67,68,69]. Consequently, careful control of PLD growth parameters are required to carefully tune the structure, crystallinity, stoichiometry and morphology of materials [69,70,71,72]. This is particularly important for ferroelectric materials as it is well known that any of these factors can have a significant impact on the ferroelectric properties [18,71]. Therefore, in this chapter, we begin with a description of the PLD set-up in our laboratory, followed by a brief description of the protocol involved in setting up a growth experiment. We then move on to describe the growth parameters that we used for the growth of ferroelectric thin films of $BiFeO_3$ and $BaTiO_3$, including detailed characterization of the structure, chemistry, morphology, domain architecture, and ferroelectric properties of these films to demonstrate our ability to synthesize high-quality versions of these materials. In particular, we focus on the PLD growth of epitaxial (001)-oriented thin films of lead-free ferroelectrics on single crystal perovskite substrates that provide a low lattice mismatch to the film overlayers, and compare them in the framework of existing experimental and theoretical studies done on these systems. The optimized growth parameters and the characterization techniques described in this chapter lay the foundation for the remainder of the thesis that aims at innovating new strain based strategies to engineer enhanced ferroelectric performance in these lead-free materials.

2.2 PLD Setup for Thin Film Growth

All thin film ferroelectric heterostructures studied in this dissertation were grown *via* PLD using a KrF excimer laser (Lambda Physik LPX205i, λ = 248 nm). The growth experiments were conducted in a vacuum chamber that is equipped with a target holder and substrate heater (Fig. 2.1). Prior to growth, the substrates are ultrasonicated for five minutes each in acetone and isopropanol, mounted on to the heater using silver paint (Leitsilber 200 silver paint from Ted Pella, Inc.), and allowed to cure at 60°C for fifteen minutes. Targets of the desired composition are sanded, cleaned, and mounted on the target rotator assembly. An on-axis growth geometry with a target-substrate distance of 6 cm is used for all depositions. The chamber is pumped down to a base pressure of at least 5E-6 Torr following which it is backfilled with oxygen (99.995% pure) to the desired deposition pressure using a variable leak valve. The substrate is then heated to the growth temperature at a ramp rate of 20°C per minute. Depositions are typically conducted at laser repetition rates between 1 - 20 Hz with energy densities ranging from 0.6 - 3 J/cm^2 depending upon target material, its density, and the desired growth rate. Prior to deposition, the target is pre-ablated to ensure that the target surface had reached steady state prior to growth. Following growth, the chamber is filled with 760 Torr of oxygen to promote complete oxidation of films and is cooled at 5°C/min. to room temperature. The growth variables involve several parameters including

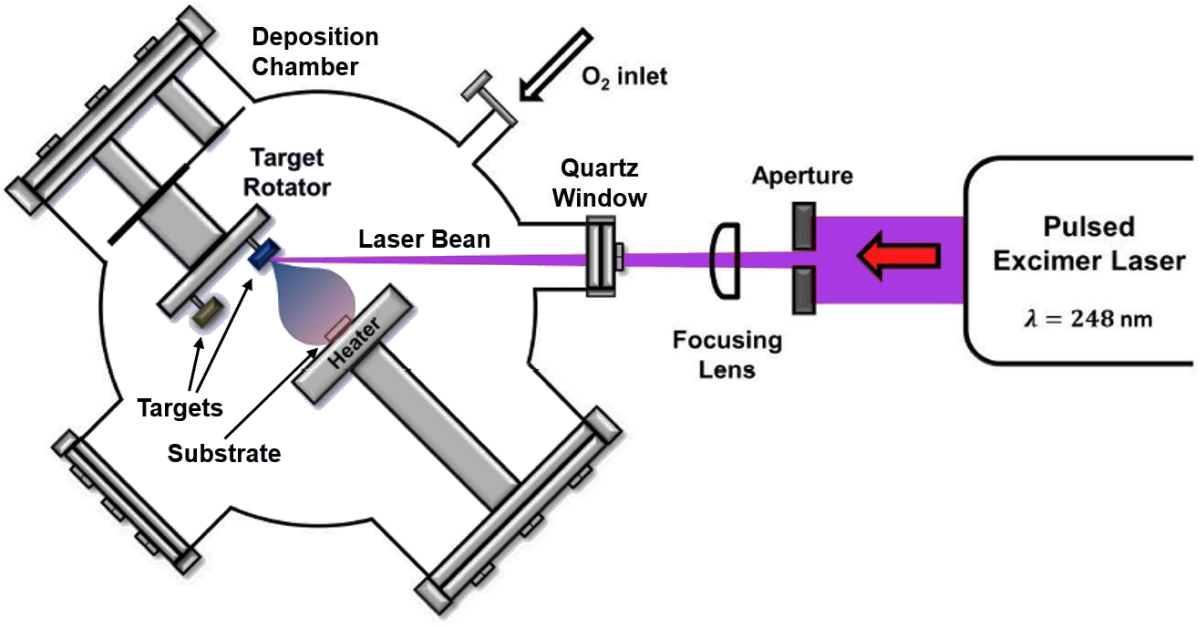

Fig. 2.1: Schematic of the pulsed-laser deposition system used for the deposition of complex oxide thin films used in this study.

substrate temperature, chamber pressure, laser fluence, and laser repetition rates that have been optimized for the thin-film systems under study and are described in the sections that follow.

2.3 $BiFeO_3$

2.3.1 Introduction and Background

$BiFeO_3$, in the bulk at room temperature, is a rhombohedrally distorted perovskite exhibiting antiferromagnetism that is coupled with ferroelectric order [73,74]. It is one of the few single-phase multiferroics (presence of coupled magnetic and electric order parameter), and has been the center of intense scientific studies due to its lead-free nature, large ferroelectric polarization, and room temperature multiferroism [75]. Significant advances have been made over the last decade towards understanding ferroelectricity and magnetism in $BiFeO_3$, as well as the nature of the coupling between these order parameters in both bulk and thin film form. The room temperature structure of $BiFeO_3$ is characterized by two distorted perovskite blocks connected along their body diagonal or the pseudocubic <111>, to build a rhombohedral unit cell (Fig. 2.2a). Through this text we will refer to the structure of $BiFeO_3$ using the pseudocubic Miller indices. In this structure the two oxygen octahedra of the cells connected along the <111> are rotated clockwise and counterclockwise about the <111> by +/-13.8(3)° and the Fe-ion is shifted by 0.135Å along the same axis away from the oxygen octahedron center position. The ferroelectric

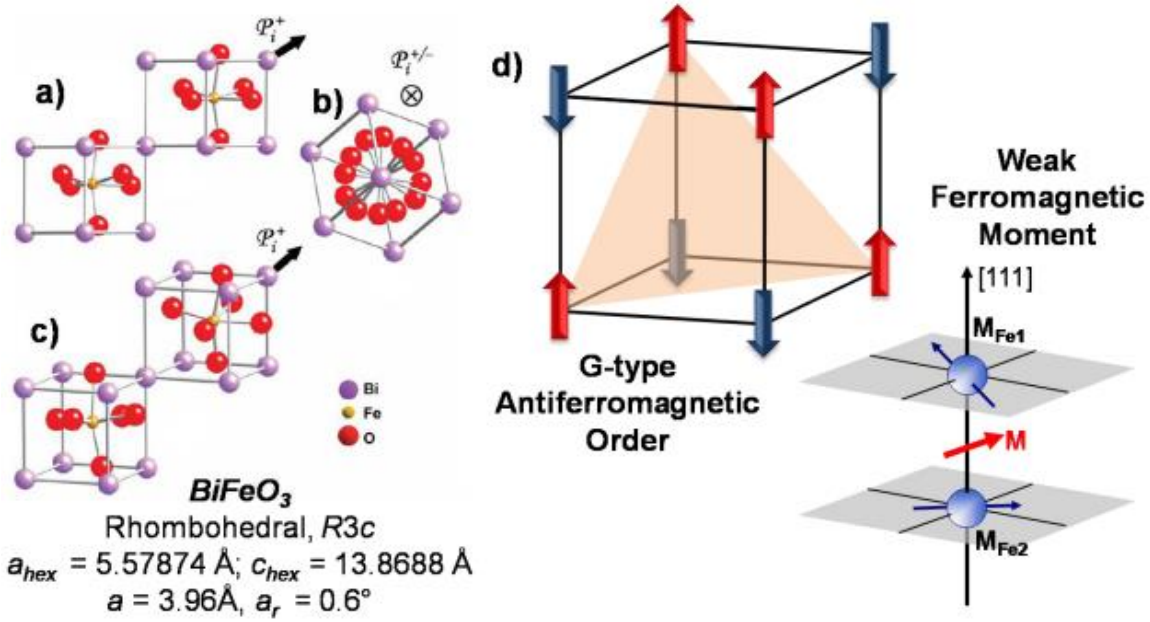

Fig. 2.2: (a)-(c) Crystal structure of rhombohedral $BiFeO_3$ viewed from (a) the [110], (b) the [111]-polarization direction, and (c) a general three-dimensional view of the structure. d) The magnetic structure of $BiFeO_3$ is shown including G-type antiferromagnetic ordering and the formation of the weak ferromagnetic moment. Figures adapted from ref. [74].

state is realized by a large displacement of the Bi-ions relative to the FeO_6 octahedral (Fig 2.2a, b, and c) [76,77]. It possesses robust ferroelectric properties with a spontaneous polarization of ~100 $\mu C/cm^2$ [78,79,80] along the <111> direction and a high Curie temperature of 1103 K [81]. It is also a G-type antiferromagnet (Fig. 2.2d) with a Néel temperature of 643 K as demonstrated by early neutron diffraction studies [82]. However, the spins between adjacent {111} are not perfectly antiparallel, as there is a weak canting moment caused by the local spin-orbit interaction, which is of a similar form to the Dzyaloshinski-Moriya interaction that results in the spin canting producing a weak ferromagnetic moment [83,84]. The high ferroelectric and magnetic ordering temperatures, robust ferroelectric properties, and its appeal as a "lead-free" ferro/piezoelectric material has attracted great attention towards $BiFeO_3$ thin film based devices. Additionally, over the last decade, researchers have demonstrated the ability to control and create periodic domain structures in $BiFeO_3$ thin films that could give rise to interesting photonic devices [85], offer new pathways for nanolithography [86], as well as new devices that take advantage of novel functionalities such as conductivity at ferroelectric domain walls [87]. Very recently, researchers discovered exiting strain-induced phase transitions and MPB-like features in $BiFeO_3$ thin films that has further fuelled the excitement towards the study of thin films of $BiFeO_3$ [63]. While this newly discovered phase of $BiFeO_3$ forms the focus of a portion of this dissertation, to begin with, in this chapter we demonstrate our ability to synthesize the conventional rhombohedral versions of $BiFeO_3$ with excellent, structural, chemical, and ferroelectric properties. In order to measure the ferroelectric properties of these films, we use $SrRuO_3$, a perovskite oxide metal with orthorhombic unit cell and a pseudocubic lattice constant of 3.93 Å that is lattice matched to rhombohedral $BiFeO_3$ [88]. The use of $SrRuO_3$ is advantageous given its excellent chemical compatibility with perovskite oxide ferroelectrics and the presence of space charge free interfaces that result in excellent ferroelectric performance including large switchable polarization and superior fatigue endurance [88,89,90,91].

2.3.2 PLD Growth of $BiFeO_3$ on Low Misfit Strain Substrates

Epitaxial thin-film heterostructures of $BiFeO_3/SrRuO_3$ were grown via PLD on a number of commercially available perovskite single crystal substrates (Crystec GmbH, Berlin) including $SrTiO_3$ (001), $DyScO_3$ (110), and $GdScO_3$ (110) that provide lattice mismatches of -1.5%, -0.4%, and 0.05%, respectively, relative to the pseudocubic lattice parameter of $BiFeO_3$. To begin with, the substrates were heated up to a temperature of 635°C in 100 mTorr oxygen followed by the growth of the epitaxial bottom electrode layer using a commercial $SrRuO_3$ target (Praxair) and a

laser fluence of 1.5 J/cm^2 at a laser repitition rate of 14 Hz and yielded films that are, typically, 30-40 nm in thickness. The $SrRuO_3$-buffered substrates were then ramped up to a temperature of 700°C for $BiFeO_3$ growth. Home-made $Bi_{1.1}FeO_3$ targets with 10% excess bismuth were used to account for its volatility at the growth temperature. The laser fluence and repetition rate were maintained at 1.3 J/cm^2 and 10 Hz, respectively, for the $BiFeO_3$ layer resulting in an effective growth rate of ~0.25 Å/s. Furthermore, in order to assure uniform deposition and appropriate chemistry, no single target was used to deposit more than 75 nm of material.

Following growth, detailed structural characterization was completed for all films using X-ray diffraction. Wide range θ-2θ diffraction patterns for $BiFeO_3$ / $SrRuO_3$ heterostructures grown on $GdScO_3$ (110), $DyScO_3$ (110), and $SrTiO_3$ (001) substrates (top-to-bottom, Fig. 2.3a) reveal that all films are epitaxial and single-phase. The $BiFeO_3$ peak for films grown on GdScO3 (110) substrates is seen only on zooming in onto the 002-diffraction condition (Fig 2.3a, inset) due to the close lattice match between $BiFeO_3$ (3.965 Å) and $GdScO_3$ (3.967 Å). Chemical composition studies were also carried out for films grown on $SrTiO_3$ substrates using Rutherford backscattering spectrometry (RBS) and was performed with an incident ion energy of 2000 keV, incident angle

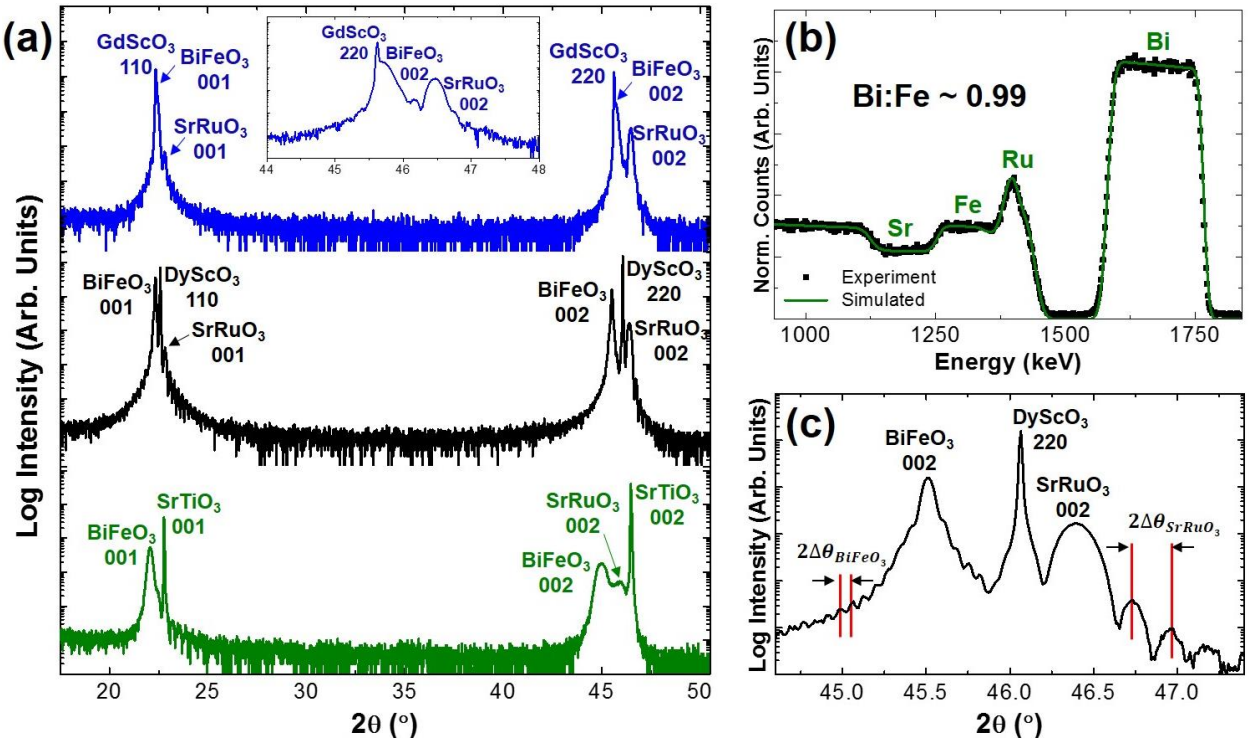

Fig. 2.3: (a) θ-2θ X-Ray scans of 140 nm thick $BaTiO_3/SrRuO_3$ heterostructures grown on $NdScO_3$ (110), $GdScO_3$ (110) and $DyScO_3$ (110) oriented substrates revealing single phase films, (b) RBS measurements for $BiFeO_3/SrRuO_3/SrTiO_3$ (001) heterostructure, and (c) Zoom-in of θ-2θ X-Ray scans for $BiFeO_3/SrRuO_3/SrTiO_3$ showing Laue oscillations for $BiFeO_3$ and $SrRuO_3$ layers.

α = 22.5°, exit angle β = 52.5°, and a scattering angle θ = 150° (Fig. 2.3b). The fits reported here were completed using the built-in fitting program in the RBS analysis software SIMNRA (simnra.com). The studies reveal that the films possess a [Bi]/([Bi]+[Fe]) ratio of 49.8% and are nominally stoichiometric within error of the measurement technique (1-2%). Furthermore, the RBS fits yield a thickness of 140 nm for the $BiFeO_3$ layer and a thickness of 40 nm for the $SrRuO_3$ layer, that matches with thickness estimates based of Laue oscillations seen from the XRD scans (Fig. 2.3a). Laue oscillations around the diffraction peaks are characteristic of films of the high crystalline quality that possess a smooth topography for the surface as well as other interfaces. These fringe oscillations also allow us to determine the film thickness (t) and is calculated as:

$$t = \frac{(i-j)\lambda}{2(\sin\theta_i - \sin\theta_j)} \sim \frac{\lambda}{2\Delta\theta\cos\theta} \qquad (2.1)$$

where, λ is the wavelength of X-ray; i, j is fringe index and $2\Delta\theta$is the fringe interval. Presence of Laue oscillations is easily seen in the zoomed in theta-2thetal line scans for the $BiFeO_3/SrRuO_3/DyScO_3$ (110) heterostructures (Fig. 2.4c). Using (1) the film thicknesses are determined as 138 nm for the $BiFeO_3$ and 44 nm for $SrRuO_3$. For brevity sake, we focus only on the $BiFeO_3$ films grown on $DyScO_3$ substrates for further characterization studies. In the sections that follow, we seek to demonstrate our ability to controllably produce high quality ferroelectric thin films of $BiFeO_3$, and also to familiarize the reader with characterization techniques that will used to investigate structure-property-functionality relationships throughout this dissertation.

2.3.3 Structural Studies using X-ray Reciprocal Space Maps

Additional insights into the epitaxial nature and crystal structure of the synthesized films including in-plane epitaxial relationship and lattice parameters, the presence of domain variants and crystallographic tilts, strain relaxation in thin films and more can be studied using high-resolution X-ray reciprocal space maps (RSM). RSMs comprise of a series of line ω-2θ X-ray scans to form a 2D map around various film/substrate diffraction conditions. The angular space can then be converted to reciprocal space using the relationships:

$$Q_{//} = \sim\frac{4\pi}{\lambda}\sin\theta\cos(\omega-\theta)\,;\; Q_{\perp} = \sim\frac{4\pi}{\lambda}\cos\theta\sin(\omega-\theta) \qquad (2.2)$$

In the case of (001)-oriented $BiFeO_3$ films, the rhombohedral ferroelectric distortion results in four possible structural variants (Fig. 2.4a) that are equally likely to form for growth on cubic (001)-oriented substrates. While all these variants have the same out-of-plane lattice parameter and consequently the same diffraction peak position for on-axis symmetric scans such as that for a 00*l*-

diffraction condition (Fig. 2.4b, schematic RSM with units in reciprocal lattice units of $BiFeO_3$ and showing single film peak at the 003-diffraction condition). Under asymmetric scan conditions, the peak positions differ for the different variants and can provide insights into the nature of the distortions present in the domain variants. For instance, in the case of $BiFeO_3$, a *h*0*l*-diffraction conditions would split into two peaks, one corresponding to variants r_2 and r_3, and the other corresponding to variants r_3 and r_4 (Fig. 2.4b, schematic RSM showing expected peak splitting in $BiFeO_3$ for the 103- and 013-diffraction conditions). Upon analyzing the RSMs for $BiFeO_3$ films grown on the orthorhombic $DyScO_3$ (110) substrates (Fig. 2.3c and d) we observe no peak corresponding to the r_1 and r_2 variants around the 013-psedocubic diffraction condition indicating an absence of these variants. Only the r_3 and r_4 variants are present and are consistent with previous reports of a 2-variant stripe domain structure of $BiFeO_3$ films grown on orthorhombic scandate substrates [92,93]. It is also seen from the RSMs (Fig. 2.4 c and d) that the 103- and the 013-film peaks have the same Q_x value as the 332- and 420- substrate peaks indicating that the films possess the same in-plane lattice parameters as the substrate and therefore coherently strained.

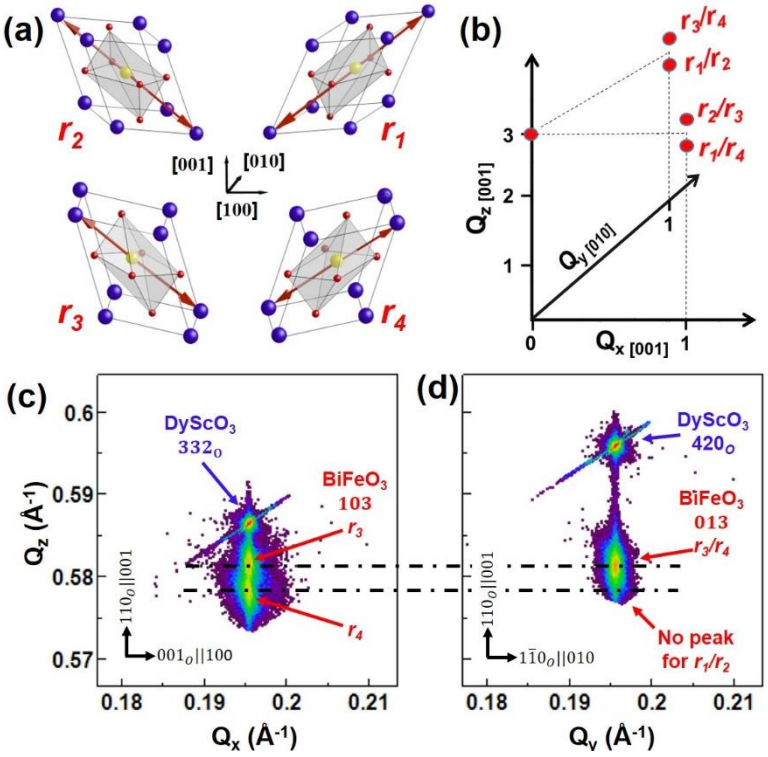

Fig. 2.4: (a) Schematic of four different structural variants (r_1, r_2, r_3 and r_4) of rhombohedral $BiFeO_3$ films possible in 001-oriented films, (b) peak location for the 003-, 103-, and 013- diffraction condition for the different variants, and RSM around the (c) 103- and (d) 013-diffraction condition for the $BaTiO_3/SrRuO_3/DyScO_3$ (110) heterostructure film.

2.3.4 Domain Architecture Studies *via* Piezoresponse Force Microscopy

The presence of only two domain variants two (r_3 and r_4) was observed in RSM studies for the $BiFeO_3/SrRuO_3/DyScO_3$ (110) heterostructure films. In order to understand the nanoscale spatial arrangement of these domains we conducted piezoresponse force microscopy (PFM), another key characterization technique that is used extensively throughout this dissertation to characterize ferroelectric order in materials (details provided in appendix A). PFM measurements

were conducted using a commercial atomic force microscope (AFM) (Cypher, Asylum Research). The measurement involves the application of a small signal AC bias using a conductive AFM tip to locally measure the piezoresponse of samples during contact mode AFM scans during which images of the surface topography, lateral and vertical piezoresponse are simultaneously obtained. PFM studies of the $BiFeO_3/SrRuO_3/DyScO_3$ (110) heterostructures reveal a surface topography with atomically flat terraces (Fig. 2.5a) that are separated by a one unit cell step heights making the film extremely smooth (RMS roughness ≈ 3 Å over a 5 x 5 μm area). The vertical (out-of-plane) PFM image (Fig 2.5b) of the same area shows a uniform contrast and corresponds to a common downward pointing polarization for all variants present, and is in tune with what is expected for $BiFeO_3$ thin films grown on a bottom $SrRuO_3$ electrode [94]. The lateral (in-plane) PFM image (Fig. 2.5c) reveals two distinct contrast, and in combination with the OOP PFM images are indicative of the presence of only two domain variants (as suggested by RSM studies). It is also seen that each domain at an average is about 125 nm wide and they form a stripe-like pattern of domains separated by 71° domain walls that run along the in-plane orthorhombic [110] of the $DyScO_3$ (110) substrate. Such ordered domain architectures in $BiFeO_3$ thin films have been demonstrated previously with contributions from several parameters including electrostatic boundary conditions, substrate vicinality, choice of anisotropic substrates, and substrate orientation [62,92,95,96,97]. Our results are consistent with these studies and further demonstrate our ability to synthesize high quality epitaxial thin films of $BiFeO_3$. Furthermore, these studies also demonstrate the use of PFM as a versatile tool to characterize and understand the domain structure of such ferroelectric materials. In addition to simple imaging, PFM also enables local ferroelectric switching studies [98], and has been employed in Chapter 5 to understand the

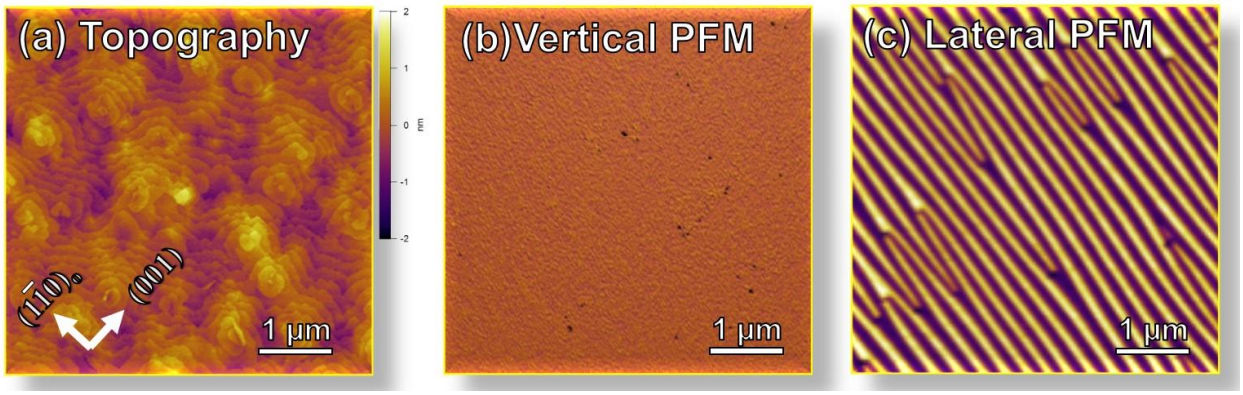

Fig. 2.5: (a) Topography, (b) Lateral PFM and (c) Vertical PFM images revealing an atomically flat topography and a two-variant stripe 71° domain wall structure for the $BaTiO_3/SrRuO_3/DyScO_3$ (110) heterostructure film.

switching behavior and the origin of highly enhanced electromechanical responses that have been observed in mixed-phase structures that form in highly compressively strained $BiFeO_3$ films.

2.3.5 Ferroelectric and Dielectric Characterization

The structural, chemical, and piezoresponse studies conducted so far demonstrate the high quality of these $BiFeO_3$ films that is also reflected in their ferroelectric and leakage characteristics. *P-E* hysteresis loops are sharp and square without any evidence of leakage, and yield a 2*Pr* value of 130 $\mu C/cm^2$ (Fig. 2.6a). Such values are consistent with previously measured values for BFO and theoretically predicted values for (001)-oriented films. Furthermore, current-voltage (*I-V*) measurements (Fig. 2.6b) reveal highly symmetric *I-V* curves and the low leakage performance.

In our studies so far, we began with a description of the growth parameters for the synthesis of (001)-oriented $BiFeO_3$ thin films. We have then focused specifically on films grown on $DyScO_3$

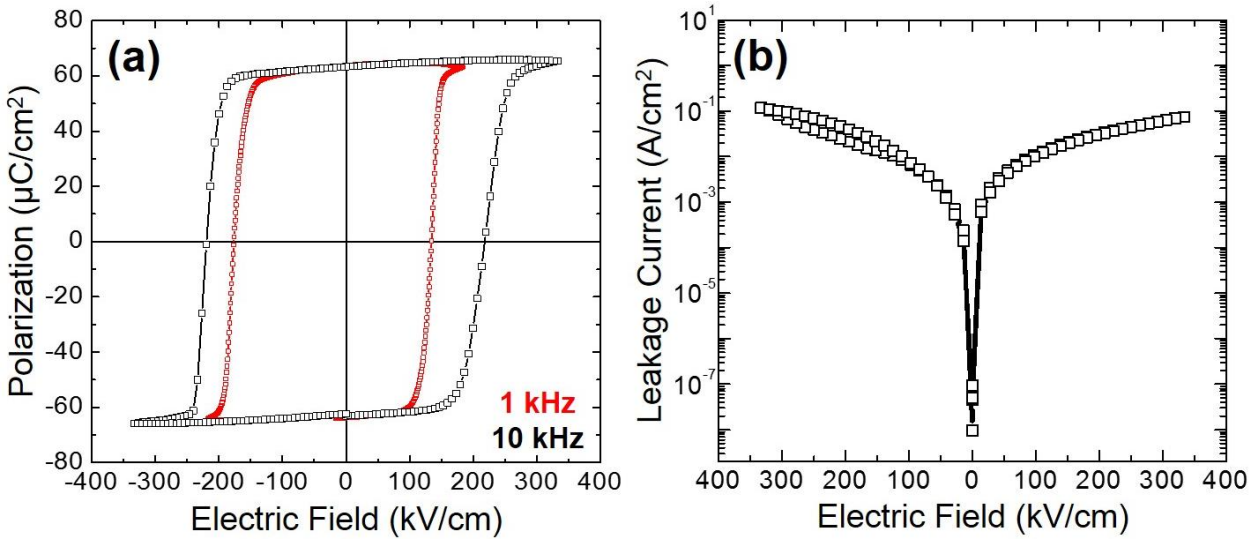

Fig. 2.6: (a) Ferroelectric hysteresis loops, and (b) current-voltage (I-V) data for a 140 nm thick $BaTiO_3$ film on an $SrRuO_3$ buffered $DyScO_3$ (110) substrate.

(110) substrates and have explored the use of a combination of X-ray diffraction, scanning probe-based studies, and ferroelectric measurements to study the structure, domain architecture, and ferroelectric properties of the film, while simultaneously demonstrating our capability to synthesize high quality films of $BiFeO_3$. Next, we move on to study the growth, structure and ferroelectric properties of $BaTiO_3$, the second lead-free ferroelectric system studied in this dissertation.

2.4 $BaTiO_3$

2.4.1 Introduction and Background

$BaTiO_3$ is the first ceramic ferroelectric known to man and was discovered in the early 1940's. Even today, it is widely used in the manufacture of a variety of electroceramic components manufacture including multilayer ceramic capacitors (MLCCs), positive temperature coefficient (PTC) thermistors, and a variety of electro-optic devices. Over the years, $BaTiO_3$ has been used in a wide variety of applications in various forms of crystals, bulk ceramics, multilayers, and thin films [99]. Bulk $BaTiO_3$, at room temperature, has a tetragonally distorted perovskite structure, with space group *P*4*mm* and lattice constants a = 3.992 Å and c = 4.036 Å ferroelectric polarization of P_r = 26 μC/cm^2 along the [001]. The tetragonal phase is stable in the temperature range 5°C < T < 120°C (T_C). Below 0°C, $BaTiO_3$ remains ferroelectric but the structure changes from tetragonal to orthorhombic (*mm*2) with a polarization along the pseudocubic [011]. A third phase transition occurs at -70°C, below which the structure is rhombohedral (*R*3*m*) with a ferroelectric distortion along the pseudocubic [111]. Above T_C, bulk $BaTiO_3$ has a nonpolar, centrosymmetric cubic structure ($Pm\bar{3}m$). While $BaTiO_3$ was the first piezoelectric transducer ceramic ever developed, its relatively low *Tc* has resulted in it being almost entirely replaced by lead-based ferroelectrics in tranducer-based and many other applications, especially those requiring high-temperature operation [4]. However, researchers have demonstrated just about a decade ago, that just a percent of epitaxial compressive strain in thin films of $BaTiO_3$ can increase the T_C by several hundred degrees with simultaneous enhancements in ferroelectric polarization [60]. This makes strained $BaTiO_3$, in the thin-film form, a strong candidate for replacement of lead-based ferroelectrics in several high-temperature applications. Therefore, in Chapter 5 and 6 of this dissertation, we have explore new strain-based strategies involving a combination of epitaxial strain and defect-engineering to further control the temperature dependent ferroelectric properties of thin films of $BaTiO_3$. Nevertheless, in this chapter, we focus on aspects of PLD growth to achieve stoichiometric versions of $BaTiO_3$ thin films with minimal defect related lattice expansion, followed by a characterization of chemical, structural, and ferroelectric properties.

2.4.2 PLD Growth and Characterization of $BaTiO_3$ Thin films

Recent work by Kan *et al.* [71] on the PLD growth of $BaTiO_3$ thin films have revealed a strong dependence of laser fluence on film stoichiometry and ferroelectric properties. It is therefore

important to be able to produce ideal defect-free films and also accurately characterize and quantify any deviations from the ideal state that could alter its ferroelectric responses. For this, we have conducted a systematic study to optimize the PLD growth parameters to synthesize near ideal $BaTiO_3$ thin films. Growths were carried out on $NdScO_3$ (110) single crystal substrates (corresponding to a low tensile lattice mismatch of 0.08% with the pseudocubic lattice parameter of $BaTiO_3$) at a growth temperature of 600°C, a background oxygen pressure of 20 mTorr, and the laser fluence was varied from 0.6 to 2.5 J/cm^2. XRD studies (Fig. 2.7a) focusing on the impact of the laser fluence reveal well defined high-intensity film peaks for fluences in excess of 1.5 J/cm^2. However, higher fluences result in films with expanded out-of-plane lattice parameters indicative of the presence of defects in films. Thermal conductivity measurements are known to be a sensitive probe for defects as it is known that increased disorder from defects can greatly enhance phonon scattering rates and thereby dramatically reduce thermal conductivity in these materials [69,100]. Thermal conductivity was probed for these films using time-domain thermoreflectance (TDTR) [101,102]. It is seen that the film grown at 1.5 J/cm^2 shows negligible out-of-plane lattice expansion as well as one of the highest thermal conductivity value of ~2.4 Wm^{-1}K^{-1} (Fig. 2.7b). Furthermore, RBS studies (Fig.2.7c) of films grown at 1.5 J/cm^2 reveal stoichiometric films with a [Ba]/([Ba]+[Ti]) ratio of 0.5. All these studies, indicate that the laser fluence of 1.5 J/cm^2 is optimal for the synthesis of near ideal $BaTiO_3$ thin films. Additional studies of structure, chemistry, and the impact of fluence on ferroelectic properties for films grown at laser fluences of 1.5 J/cm^2 and

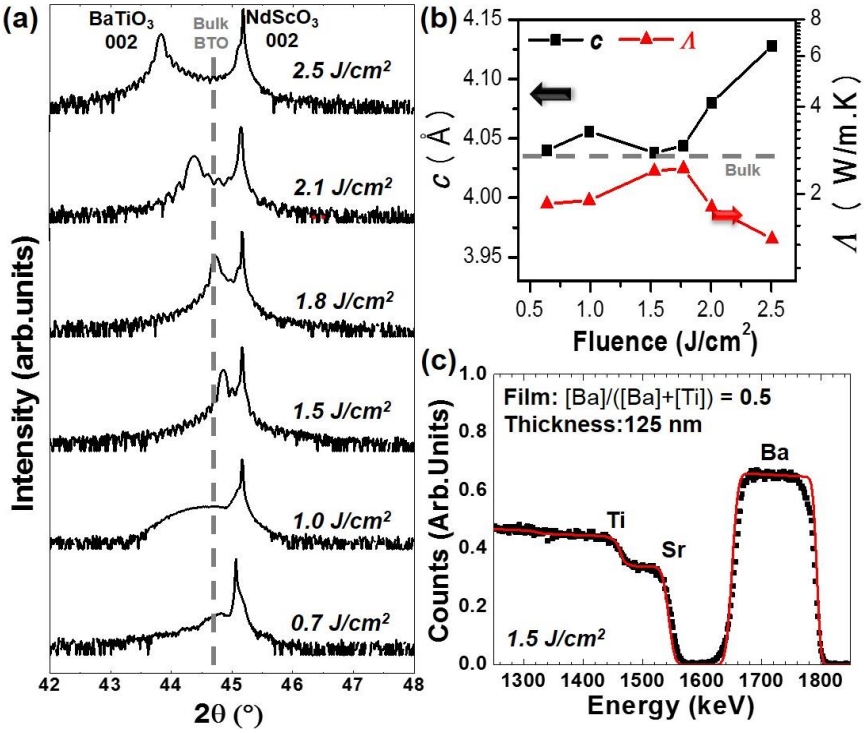

Fig. 2.7: (a) θ-2θ X-Ray scans of $BaTiO_3/NdScO_3$ (110) heterostructures grown on over the fluence range of 0.6 -2.5 J/cm^2, (b) out-of-plane (*c*) lattice parameter and thermal conductivity (Λ) of films as a function of fluence, and (c) RBS of a 125nm $BaTiO_3/SrTiO_3$ film grown at a fluence of 1.5 J/cm^2

higher discussed at length in Chapter 5. Nevertheless, these studies reveal that fluence used in PLD growth condition can have dramatic impacts on the structure and properties of epitaxial $BaTiO_3$ thin films.

2.5 Conclusions

We have shown that pulsed laser deposition can be used to grow high-quality epitaxial thin films of $BiFeO_3$ on a variety of single crystal oxide substrates with lattice matched $SrRuO_3$ as a bottom electrode. We have also conducted structural, chemical and ferroelectric studies to demonstrate the excellent quality of the films synthesized. At the same time we have introduced several characterization techniques including XRD, RBS, RSM, and PFM that will be extensively utilized for investigating structure-property relationships throughout this dissertation. In the case of PLD growth of epitaxial $BaTiO_3$ thin films, we have shown that laser fluence can markedly impact the quality of these films. It is seen that lower fluence films possess poor crystallinity while higher fluence films demonstrate large lattice parameter expansions, both resulting in poor thermal properties of these films. Using a combination of XRD, RBS, and TDTR-based thermal conductivity measurements, we have narrowed down to an optimum fluence condition of 1.5 J/cm^2 for the growth of epitaxial $BaTiO_3$ thin films. In summary, this chapter lays the ground work for the PLD growth as well as various characterization techniques that are important for the research presented in the remainder of this dissertation.

CHAPTER 3

HIGHLY COMPRESSIVELY STRAINED $BiFeO_3$: NANOSCALE STRUCTURE AND MECHANISM FOR ENHANCED ELECTROMECHANICAL RESPONSES

In this chapter we explore the role of large, compressive epitaxial strain in stabilizing novel metastable phases in $BiFeO_3$ that are not present in the bulk at any temperatures. Previous work on epitaxial thin films of these materials, had shown that large compressive strains, exceeding 4.5%, can drive the formation of exotic mixed-phase structures that are accompanied by highly-enhanced piezoresponses. We present experiments involving a combination of highly controlled epitaxial thin-film growth followed by detailed investigations of the phase- and surface- structure using high resolution XRD and scanning probe-based techniques that unravel the complex structure of the various phases present in the mixed-phase films including their intricate nanoscale spatial arrangement. We finally conclude this chapter with detailed PFM-based nanoscale switching studies which reveal the ability of the various phases present to reversibly transform from one to the other under applied electric fields is responsible for the large reversible electric field induced strains observed in these films.

3.1 Introduction

In Chapter 1, we discussed various chemistry-based strategies employed for tuning ferroelectric and piezoelectric susceptibilities in materials. In particular, we saw that state-of-the-art piezoelectric materials have generally been based on perovskite materials with complex lead-based chemistries including PZT, PMN-PT and others, with special attention being given to these complex materials due to the presence of a compositionally driven MPB between tetragonal- and rhombohedral-polymorphs that give rise to significantly enhanced piezoelectricity in these materials [1,33,43]. Traditionally, it has been observed that MPBs result from chemically-induced structural instabilities and thus are often observed in mixed perovskites such as PZT at x = 0.52 and PMN-PT at x = 0.33. However, it has been recently shown that MPB-like features can also exist in chemically simple materials that are appropriately strained [42,63,103]. This includes the demonstration of a strain-induced structural phase transition in $BiFeO_3$ under conditions of compressive epitaxial strain exceeding 4.5% that gives rise to the formation of MPB-like mixed phase structures and highly enhanced electromechanical responses (reversible electric-field induced strain as large as 4-5%), making it a promising alternative for future high performance lead-free piezoelectrics [63,104]. While in Chapter 2, we discussed the PLD growth and characterization of $BiFeO_3$ thin films on low lattice mismatched substrates including $DyScO_3$ (110) and $GdScO_3$ (110) that yielded films with classic stripe-like 109° and 71° domain walls typical of rhombohedral ferroelectrics, in this chapter we will focus on films grown on highly compressive $LaAlO_3$ (001) substrate where the aforementioned complex strain-induced phase boundaries and enhanced electromechanical responses have been reported. Using highly-controlled epitaxial thin film growth, X-ray reciprocal space mapping (RSM), high-resolution atomic force microscopy (AFM), and piezoresponse force microscopy (PFM) we present a detailed study of the nanoscale structural evolution at these strain-induced phase boundaries including the observation of previously unreported phase complexity at these boundaries and propose a mechanism for the observed enhanced electromechanical responses.

3.2 Prior Studies on Phase Stability of Strained $BiFeO_3$

As early as 2005, the structural stability of the parent rhombohedral phase of $BiFeO_3$ had been the focus of theoretical studies [105,106]. Although the parent ground state is a rhombohedrally distorted perovskite (*R*3*c*), a tetragonally distorted perovskite phase (*P*4*mm*

symmetry, a ~ 3.665 Å, and c ~ 4.655 Å) with a large spontaneous polarization has also been explored [105,107,108]. More recently Zeches *et al.* [63] reported the observation of so-called mixed-phase thin-films possessing tetragonal-like and rhombohedral-like phases in complex stripe-like structures and enhanced electromechanical responses. Since this report, additional information has come forth about these materials including the fact that the so-called tetragonal-like phase (hypothesized to possess *P*4*mm* symmetry) is, in fact, monoclinically distorted (possessing *Cc* symmetry) [109,110]. Nonetheless, a thorough understanding of the complex structure of these phase boundaries in $BiFeO_3$ remains incomplete. Building off of our understanding of structure and response in chemically driven MPB systems [111], we seek to uniquely identify the boundary nanostructure and the pathway for enhanced electromechanical response in highly compressively strained $BiFeO_3$ films.

3.3 Growth and Structure of Highly Compressively Strained $BiFeO_3$ Films

We grew samples of epitaxial $BiFeO_3$ thin films *via* PLD (using optimized growth parameters as described in Chapter 2) on single-crystal $LaAlO_3$ (001) substrates that offer a compressive lattice mismatch of 4.5%. Films with thicknesses between 20 and 200 nm were produced and thicknesses were confirmed (when possible) through analysis of X-ray Kiessig fringes. Following growth, detailed phase and structural information including lattice parameter, distortions, tilts, etc. were obtained using high-resolution RSM. At the same time, high resolution AFM studies of the topography or the surface structure of the films were also conducted.

Consistent with prior reports [63], films less than ~40 nm thick grown directly on $LaAlO_3$ (001) substrates exhibited only the distorted tetragonal-like phase. The complexity of this system calls for a rigorous definition of the phases present, and we will henceforth refer to this monoclinically distorted tetragonal phase possessing a large c/a-lattice parameter ratio as the M_{II}-phase. AFM studies of these samples reveal atomic-level terraces with step-heights corresponding to a single unit cell (~4.65Å) (Fig. 3.1a). Detailed RSM of the 001-diffraction condition for these films (Fig. 3.1b) reveal the presence of only two diffraction conditions – the 001-diffraction peak for the $LaAlO_3$ substrate and that for the M_{II}-phase of $BiFeO_3$ (note the presence of Kiessig fringes in this RSM, Fig. 3.1b). As film thickness is increased, complex mixed-phase samples are observed. The typical topography for a 130 nm thick $BiFeO_3/LaAlO_3$ (001) film reveals regions of pure M_{II}-phase (bright areas, Fig. 3.1c) and mixed-phase regions (striped regions, Fig. 3.1c). We note that early reports suggested these mixed-phase regions were made of an intimate mixture

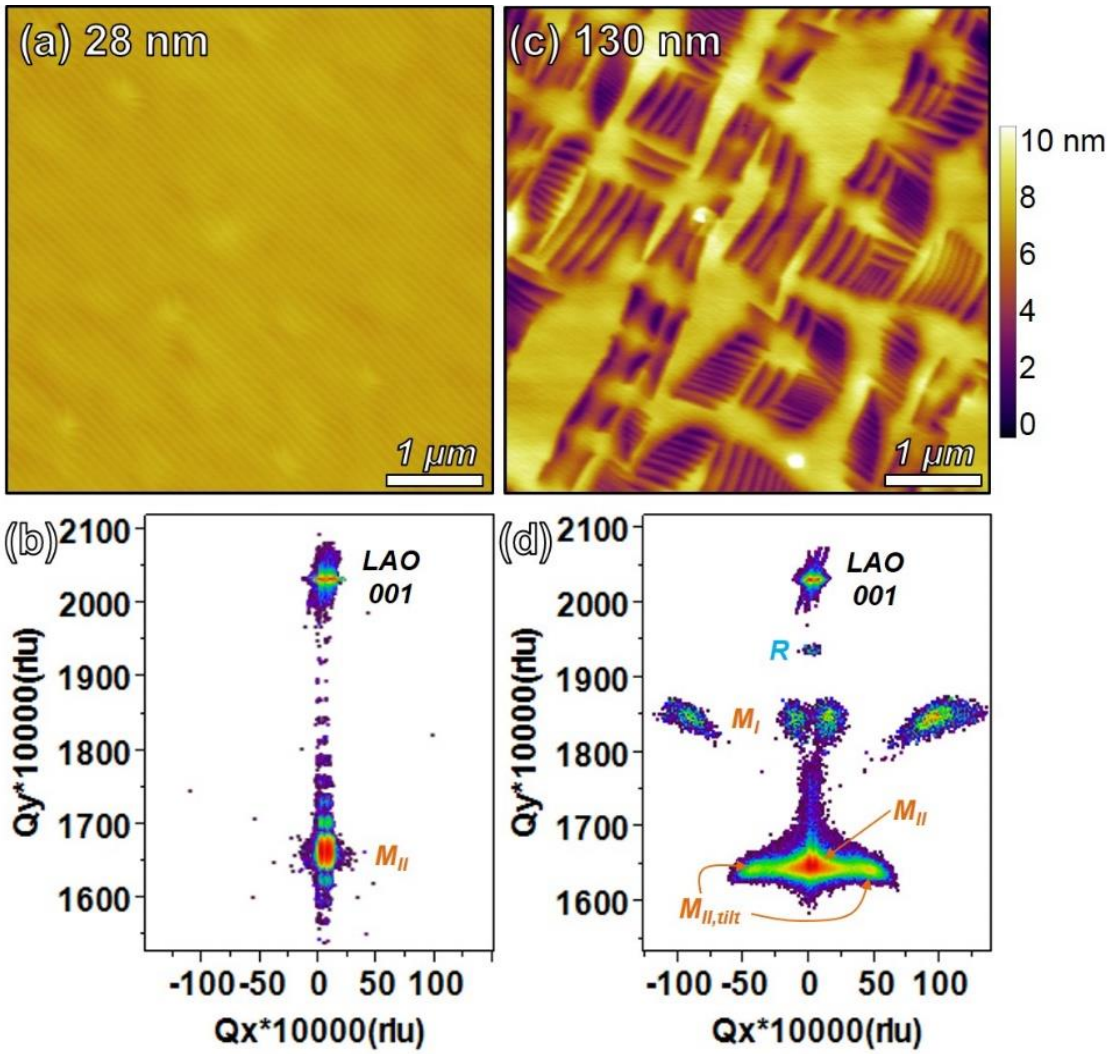

Fig. 3.1: AFM image and RSM of the 001-diffraction peak for 28 nm (a and b, respectively) and a 130 nm thick (c and d, respectively) $BiFeO_3/LaAlO_3$ (001) thin films. Note the presence of Laue Oscillations in part b.

of the tetragonal-like and a monoclinically-distorted, bulk-like rhombohedral phase. In turn, our studies provide evidence of a more complex nanostructural arrangement. Again, in order to maintain a rigorous approach to this complex system, we refer to the bulk-like rhombohedral phase as the R-phase. This designation is made based on parallel studies done on $BiFeO_3$ films of similar thickness grown on $SrTiO_3$ (001) substrates [112,113,114]. Detailed RSM of the 001-diffraction condition for the 130 nm thick $BiFeO_3/LaAlO_3$ (001) film (Fig. 3.1d) shows significant complexity. Peaks corresponding to the 001-diffraction peak of the $LaAlO_3$ substrate, the R-phase of $BiFeO_3$ (out-of-plane lattice parameter of 3.979 +/- 0.003 Å), and the M_{II}-phase of $BiFeO_3$ (out-of-plane lattice parameter of 4.667 +/- 0.005 Å) are easily identifiable and labeled accordingly and are consistent with previous data. We see that the peak corresponding to the R-phase has very low intensity and note that they have been found to be completely absent in diffraction studies of

similar films. Additionally, there are two new sets of diffraction peaks present in Fig. 3.1d that are not observed in the thinner films. The first set is located on either side of the peak from the M_{II}-phase in Q_x-space at a Q_y-value of ~1640 (labeled as $M_{II,\,tilt}$ in Fig. 3.1d). These peaks correspond to a phase that possesses the same out-of-plane lattice parameter (4.667 +/- 0.005 Å) as the M_{II}-phase, but is tilted by ~1.53° along the [100] relative to the [001] sample normal. The second set, comprises of four diffraction peaks at a Q_y-value of ~1850 which represents a previously unobserved phase, heretofore referred to as an intermediate monoclinic phase (M_I-phase). The M_I-phase has an out-of-plane lattice parameter of 4.168Å – intermediate between the R- and M_{II}-phases. Additionally two pairs of peaks are observed – the outer pair suggests this phase has a tilt of ~2.88° along the [100] relative to the [001] sample normal and the inner pair suggests this phase has a rotation about the sample normal of ~0.4°. This conclusion comes from the observation of two, orthogonal sets of stripe-like features on the surface of the films. The outer- and inner-peak pairs correspond to diffraction from the same phase in these two stripe-sets (rotated by 90° in the plane of film). This suggests that the M_I-phase is tilted along a direction rotated by ~0.4° from the [100].

In order to further understand this complex structure, we conducted a series of high-resolution RSM studies of a number of diffraction peaks to help develop a complete picture of the structure of the phases present. We have investigated RSMs of the 103, 013, 113, $1\bar{1}3$, 203, and 023 diffraction conditions for a number of films ranging in thickness from 20 nm to 200 nm. Studies of 28 nm thick films that were found to possess only the M_{II}-phase (Fig. 3.1a) provide important information about the distortions of this phase. RSM of the 103- (Fig. 3.2a) and the 113- (Fig. 3.2b) diffraction peaks for the M_{II}-phase reveals a splitting of the peak into three and two distinct peaks, respectively. This splitting uniquely identifies that the distorted tetragonal M_{II}-phase is in reality monoclinically distorted, with a small tilt along the <100> in-plane directions. Further analysis of the RSMs shown here, as well as RSM from other peaks on this sample (not shown), and from data on films of other thicknesses has allowed us to uniquely identify the structure of this so-called M_{II}-phase. The M_{II}-phase exhibits slightly anisotropic in-plane lattice parameters (a ~ 3.74 Å, b ~ 3.82 Å), a c/a lattice parameter ratio of 1.23, and a monoclinic angle (β) of 88.1°. This data for the M_{II}-phase is consistent with recently reported values [115], and unequivocally suggests that the distorted tetragonal phase is indeed monoclinic with either *Pm* or *Pc* symmetry. Turning our attention now to thicker films (*i.e.*, 130 nm) that exhibit the complex

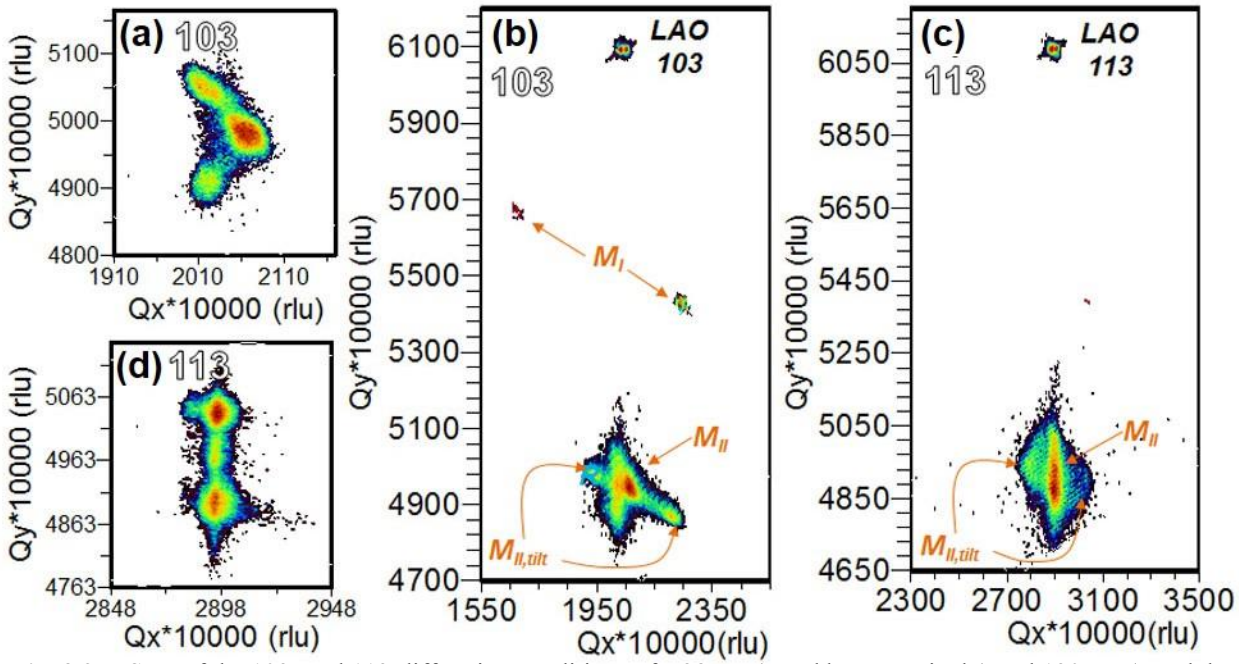

Fig. 3.2: RSMs of the 103- and 113-diffraction conditions of a 28 nm (a and b, respectively) and 130 nm (c and d, respectively) thick $BiFeO_3/LaAlO_3$ (001) film.

mixed-phase topography (Fig. 3.1c), RSM studies have provided similar details about the various phases present in these samples. RSM studies of the 103- (Fig. 3.2c) and 113- (Fig. 3.2d) diffraction peaks are provided. We note that the peaks corresponding to the M_{II}-phase are again observed to split into three and two diffraction peaks in the 103- and 113-diffraction conditions respectively; which is consistent with the thinner films and a monoclinic distortion. Furthermore, we observe additional diffraction peaks that, to our knowledge, have thus far been overlooked by researchers. The peaks, which correspond to the so-called $M_{II,tilt}$-phase are found to possess in-plane lattice parameters closely matching the M_{II}-phase. Again, this phase is found to be tilted from the substrate normal by ~1.53° along the <100> direction. We have additionally been able to capture the first experimental evidence for the intermediate M_I-phase (Fig. 3.2c). Analysis of this and other diffraction scans has enabled us to produce an estimated unit cell structure for this intermediate phase – in-plane lattice parameters are found to be ~3.82Å while the out-of-plane lattice parameter is found to be ~4.168Å. More importantly this phase is found to be tilted from the substrate normal by ~2.88° and rotated in-the-plane of the film about the substrate normal by ~0.4°. This analysis implies that the structural distortions in this phase are unique compared to the other phases present. The splitting of diffraction peaks in the off-axis RSM of Fig. 3.2 also suggest the co-existence of structural domain variants for the M_{II}-phase and is easily verified by examining a 43 nm thick $BiFeO_3$ film with both AFM (Fig. 3.3a) and PFM (Fig. 3.3b). Topography

images (Fig. 3.3a) reveal the presence of both pure M_{II}-phase regions as well as mixed-phase regions corresponding to the stripe-like features. Upon further investigation of PFM contrast in this same region additional stripe-like contrast is observed to occur within the purely M_{II}-phase regions in the lateral (in-plane) response (Fig. 3.3b). Analysis of vertical (out-of-plane) contrast (inset, Fig. 3.3b) reveals no contrast across the same area. This in-plane PFM contrast occurring in the purely M_{II}-phase regions can again be attributed to the monoclinic distortion. These distortions effectively tilt the polarization direction along the in-plane [100] and [010] of the film and give rise to weak in-plane contrast in the PFM images. These results are consistent with prior studies [110,116], and provide further details of the complexity of this structure.

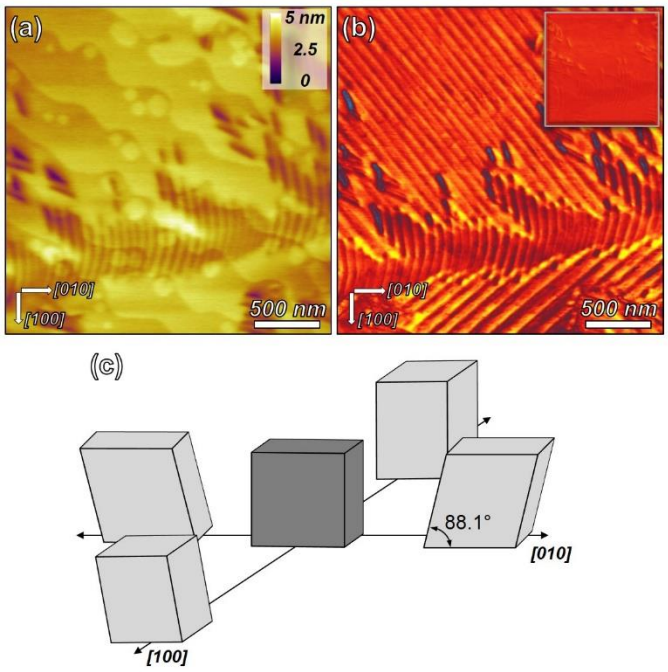

Fig. 3.3: a) AFM image of the surface topography of a 43 nm thick $BiFeO_3/LaAlO_3$ (001) thin film. b) Lateral PFM image of the same area in A) reveals the presence of in-plane contrast; inset shows the lack of vertical PFM contrast. c) Schematic illustration of the monoclinic distortion present in the M_{II}-phase that gives rise to the observed in-plane PFM contrast.

3.4 Spatial Distribution of Phases in Mixed-Phase Films

In this section, we determine the spatial arrangement of complex mixed phases observed in XRD studies of thicker films of highly compressively strained $BiFeO_3$ that could potentially shed light on mechanism for the enhanced electromechanical response of this material. For this, we first focus on understanding the nanoscale surface structure of the mixed-phase films obtained from high-resolution AFM studies which provide direct images of the structural features observed in the X-ray diffraction studies. Evidence for regions of pure M_{II}-phase and mixed-phase structures (saw-tooth-like features on the surface) are easily observed in 140 nm thick films (Fig. 3.4a). We see that the mixed phase regions *do not* possess a flat-bottom or well-like structure, but are saw-tooth in nature as demonstrated by the indicative line-trace (dashed-line in Fig. 3.4a, data Fig. 3.4b). Furthermore, we have found that these features are asymmetric and, in this example, the left side of the saw-tooth is inclined to the substrate surface with an angle of ~1.8°, while the right side

of the saw-tooth is inclined to the surface at an angle of ~2.8° This suggests that the phases observed in the X-ray diffraction studies to be tilted by ~ 1.6° ($M_{II,tilt}$-phase) and ~2.8° (M_I-phase) are located in intimate proximity to one another in the mixed-phase, stripe-regions. Prior work suggested an intimate mixture of the R- and M_{II}-phases in these regions, but our data indicates otherwise. Further evidence against this intimate mixture of the R- and M_{II}-phases is provided in the line-trace parallel to the stripe-like features (red line Fig 3.4a, data Fig. 3.4c). This analysis shows that there is an overall depression of the surface height from the M_{II}-phase (left- and right-sides of Fig. 3.4c) and the mixed-phase region. We note that the data in Fig. 3.4c is an average height trace data set compiled from analysis of five line-traces along peaks and five line-traces along valleys in the mixed phase region of a number of films. In other words, this data represents the average height profile for all regions present in these films. The average height depression is ~5 nm (Fig. 3.4c) while the overall film thickness is 140 nm. This film thickness is equivalent to 300 unit cells of the M_{II}-phase (c = 4.667Å). Surface area analysis reveals that the mixed-phase regions are made-up of 63% M_{II}-phase and 37% M_I-phase. Thus, assuming the mixed-phase regions are made up only of the M_I- and $M_{II,tilt}$-phases, simple fractional analysis using these values and the lattice parameter and tilt values of the various phase as determined by X-ray diffraction, we estimate an anticipated depression of the surface for the mixed-phase region of 5.6 nm compared to the surrounding pure M_{II}-phase regions. On the other hand if the mixed-phase regions possessed R- and M_{II}-phases (as has previously been suggested) we would anticipate a depression of over 7.6 nm as well as different surface morphology (well-like, flat bottom features). Additionally, no tilt of the R-phase diffraction peaks has been observed that would suggest it would be present in these regions. Furthermore, we have analyzed carefully the diffraction patterns of many samples for evidence of the R-phase. Studies of films from 28 to 200 nm reveals no appreciable change in the peak

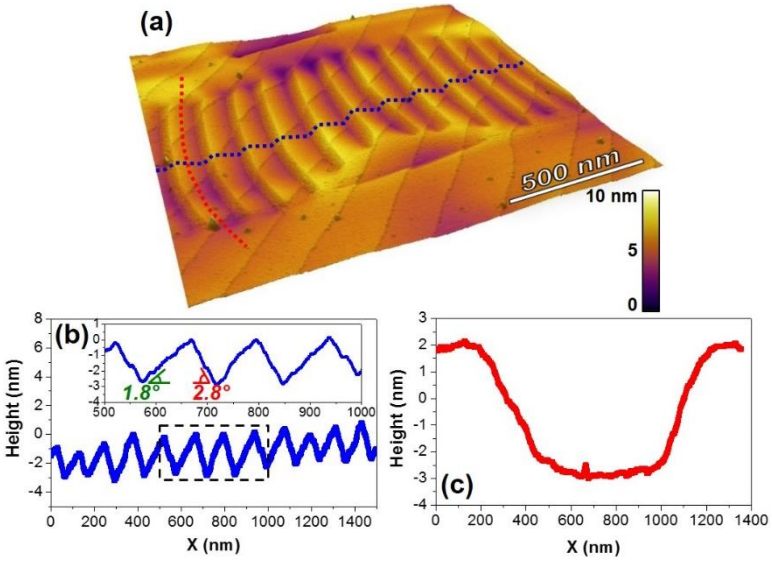

Fig. 3.4: a) AFM topography, b) line-trace along the dashed line in part a), and c) line-trace along the red line in part a) of a 140 nm thick $BiFeO_3/LaAlO_3$ (001) thin film.

intensity of the R-phase throughout this thickness range, suggesting that very small fractions of the film are made up of the R-phase. These results thus lead us to conclude that the mixed-phase regions of highly-strained $BiFeO_3/LaAlO_3$ (001) thin films are made up not of an intimate mixture of bulk-like rhombohedral- and tetragonal-like phases, but an intimate mixture of highly distorted, monoclinic phases – one a monoclinic version of the tetragonal phase ($M_{II,tilt}$-phase, c/a ~ 1.23) tilted 1.6° from the surface normal and the other an intermediate, monoclinic phase (M_I-phase) tilted 2.8° from the surface normal in the opposite direction. With such an understanding of the nanoscale phase distribution, we proceed to investigate the mechanism for enhanced electromechanical responses in these materials.

3.5 Mechanism for Enhanced Electromechanical Responses

Application of electric fields to these mixed-phase samples results in strong electromechanical responses. Local switching studies using PFM reveals surface electromechanical strains as large as 4-5% (Fig. 3.5) and have been reported in several previous studies.[63,104] Recent measurements of the effective converse piezoresponse (d_{33}) on clamped capacitor-based structures of these films revealed a d_{33} value of 115 pm/V, that is higher than the responses of any of the parent phases (~50 pm/V for the rhombohedral phase, and ~30 pm/V for the tetragonal-like phase) [77,103,104].

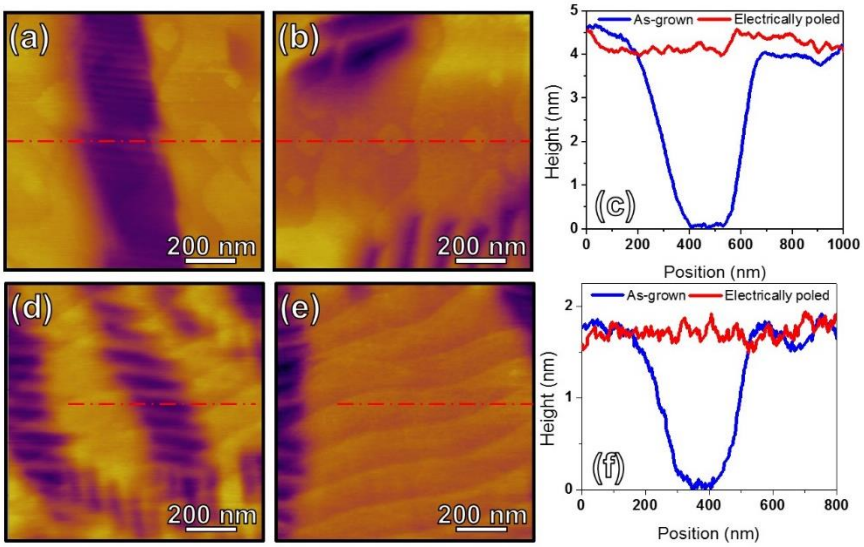

Fig. 3.5: AFM images of 100 nm and 50 nm $BiFeO_3/La_{0.5}Sr_{0.5}CoO_3/LaAlO_3$ (001) heterostructures in the a) and d) as-grown state, b) and e) following electrical poling, and c) and f) corresponding line traces at the red-lines.

In order to understand the mechanism for such large electromechanical responses, we studied the evolution of the surface structure and polarization of a 1 x 1 μm region of a mixed-phase 100 nm$BiFeO_3$/5 nm $La_{0.5}Sr_{0.5}CoO_3/LaAlO_3$ (001) thin film by applying different voltages to the region within the box in Fig. 3.6a using the PFM. After each applied voltage, we captured both the topography (left images Fig. 3.6) and the out-of-plane orientation of the polarization (right images Fig. 3.6). In the as-grown configuration, the film possesses a mixed-phase structure and is

entirely down polarized (Fig. 3.6a). Upon applying a 5.25V potential, we have observed no change in the surface structure or out-of-plane polarization (Fig. 3.6b). Upon further increasing the applied potential to 10.25V, however, we observe the ability to electrically drive the mixed-phase region to be entirely made-up of the M_{II}-phase (Fig. 3.6c). If we then begin to drive the same region with small negative potentials (*e.g.*, -3V) we observe the ability to completely and reversibly switch the material back into a mixed-phase structure similar to the as-grown configuration (Fig. 3.6d). Further increasing the negative potential to -5.25 V results in ferroelectric switching of the material (Fig. 3.6e), but maintains the mixed-phase structure. Application of large negative biases (-9V) results in the eventual transformation of the mixed-phase structure into an upward-poled version of the M_{II}-phase (Fig. 3.6f). The polarization of this M_{II}-phase is pointing opposite to that in the structure shown in Fig. 3.6c. If we now apply positive potentials to this region we can return to the mixed-phase structure similar to the as-grown state, but with a reversed out-of-plane polarization

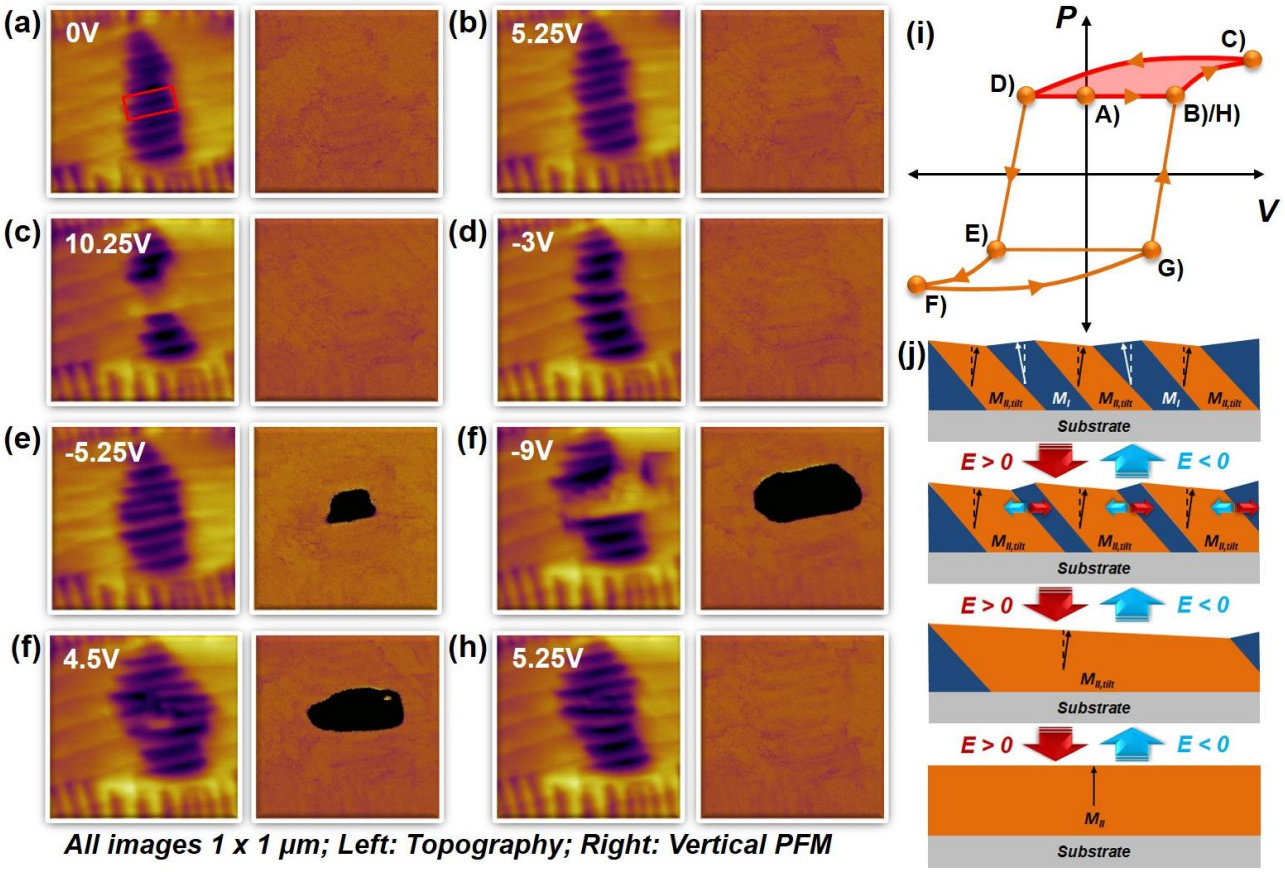

Fig. 3.6: AFM image (left) and vertical PFM image (right) of 100 nm $BiFeO_3/La_{0.5}Sr_{0.5}CoO_3/LaAlO_3$ (001) in the a) as-grown state and after being poled in the box at b) 5.25 V, c) 10.25 V, d) -3 V, e) -5.25 V, f) -9 V, g) 4.5 V, and h) 5.25 V. (All images are 1 x 1 μm). i) A schematic hysteresis loop with letters corresponding to the images in a)-h) shows the multiple pathways to enhanced electromechanical response. j) Illustration of the proposed mechanism for the large electromechanical response without the need for ferroelectric switching.

(Fig. 3.6g). Finally, by further increasing to a positive potential of 5.25V we return the structure and polarization to the as-grown configuration (Fig. 3.6h).

By navigating the hysteretic nature of electric field response in this material, we have learned a number of important features of this system. First, large surface strains of generally 4-5% occur any time the material transforms form a mixed-phase structure to the M_{II}-phase. Second, the transformations between these two states are entirely reversible. Third, there are numerous pathways to achieve large electromechanical responses in these materials. The first, as described in Figs. 3.6a-h and in the corresponding schematic hysteresis loop in Fig. 3.6i occurs upon traversing the entire hysteresis loop. Following the path from (a) to (h) in Fig. 3.6i, we undergo four transformations that give rise to large surface strains. Traversing this major hysteresis loop requires the input of considerable energy and two ferroelectric polarization switching events. On the other hand, we can achieve the same large electromechanical responses *without the need to ferroelectrically switch the sample*. By following the minor hysteresis loops B-C-D-B or E-F-G-E (one is highlighted in Fig. 3.6i) we can repeatedly transform between the mixed-phase structure and the M_{II}-phase, thereby obtaining large electromechanical responses without switching the polarization direction. This is an exciting discovery and could have important implications for utilization of these materials in devices – including possible low-power applications. The key for the enhanced electromechanical responses appears to be the ability to transform from the M_I-phase to the $M_{II,tilt}$-phase to the M_{II}-phase through a diffusion-less phase transition. Focusing on the minor hysteresis loop B-C-D-B and our step-by-step probing of the material, it appears that the application of a positive potential drives the preferential growth of the $M_{II,tilt}$-phase at the expense of the M_I-phase in the mixed-phase regions (Fig. 3.6j) until a purely $M_{II,tilt}$ region is obtained. At this point the material undergoes a final rotation of the polarization towards the surface normal and the development of the M_{II}-phase which has preferential alignment of polarization relative to the applied field direction. We note that we cannot uniquely identify if this polarization rotation occurs only after the material has transformed to the M_{II}-phase or if it gradually happens during the transformation. From a geometrical argument, however, one might expect gradual rotation of the polarization during the growth of the $M_{II,tilt}$-phase as the tilt is no longer needed to accommodate the M_I-phase and the elastic strain. Regardless, at this point the M_{II}-phase is stable and only upon application of negative potentials does the sample undergo a reversal of the

transformation and return to the as-grown structure. Such a hysteresis loop provides the actuation and deactuation of the large surface displacement required for applications.

3.6 Conclusions

Based on detailed characterization of the phase- and surface- structure of highly compressively strained $BiFeO_3$ thin films *via* high resolution XRD and scanning probe-based techniques, we have uniquely identified and examined the numerous phases present at these strain-induced phase boundaries. We have discovered an intermediate monoclinic phase (much akin to what has been observed in MPB systems) in addition to the previously observed rhombohedral- and tetragonal-like phases. Our studies reveal that the mixed-phase films are not mixtures of rhombohedral- and tetragonal-like phases as originally stated, but intimate mixtures of highly-distorted monoclinic phases (designated as M_I- and M_{II}- phases) with no evidence for the presence of the rhombohedral parent phase. Nanoscale swithching studies using PFM have provided intersting insights into the mechanism for highly enhanced piezoresponses that have been reported in these films. These studies reveal that the films are able to repeatedly transform between the mixed-phase structure and the pure M_{II}-phase under applied electric field. This can be achieved without any polarization reversal and result in large electromechanical responses with net surface displacements that are nearly 5% of the film thickness. This allows for the actuation and deactuation of large surface displacements that are important for real-world applications, and scales with the film thickness. Therefore, moving forward, it is also important to understand the thickness evolution of these mixed-phase structures and investigate the thickness limits for such strain-induced stabilization of metastable phases in the $BiFeO_3$ system. Nevertheless, these results represent an unprecedented picture of the phase complexity associated with this exciting strain-induced structural phase transition as well as direct evidence of the pathway for enhanced electromechanical response in these materials. Such unique behavior has significant implications for numerous applications and could help shed light on similar boundaries in other high-performance piezoelectrics.

CHAPTER 4

TEMPERATURE- AND THICKNESS-DEPENDENT EVOLUTION OF PHASES IN HIGHLY COMPRESSIVELY STRAINED $BiFeO_3$

In this chapter, we present the temperature- and thickness-dependent structural and morphological evolution of strain-induced phase boundaries in epitaxial $BiFeO_3$ films deposited on $LaAlO_3$ (001) substrates using a combination of high-resolution X-ray diffraction and temperature-dependent scanning-probe-based studies. These studies, in turn, provide clues to the origin of complex phase evolution that had been observed in this system, including the possibility of a strain-induced spinodal instability as the cause for the thickness-dependent transformation from a single monoclinically distorted tetragonal-like phase to a complex mixed-phase structure in thicker films. Additionally, we also observe an irreversible breakdown of this strain-stabilized metastable mixed-phase structure to non-epitaxial microcrystals of the parent rhombohedral structure of $BiFeO_3$ at thicknesses exceeding 250 nm which provides further insight into the competing nature of the various phases present in this system. Based on such an understanting, we utilize concepts of chemical pressure and demonstrate that appropriate alloying of the $BiFeO_3$ thin films can stabilize the tetragonal-like polymorph and, in turn, the mixed-phase structures that form and delay the onset of strain relaxation and epitaxial breakdown in these highly compressively strained films.

4.1 Introduction

In Chapter 3, we developed a complete picture of the structure and the nanoscale spatial distribution of various phases present at the strain-induced phase boundary in $BiFeO_3$ films grown on highly compressive $LaAlO_3$ (001) substrates. We also conducted stroboscopic-PFM based poling studies that demonstrated that reversible electric field switching between the various highly distorted monoclinic phases are crucial to produce strong electromechanical responses in these materials [117,118]. Since our studies detailed in Chapter 3, additional information has come forth about the structure of these highly-strained films [109,110,119,120], with several recent reports showing additional near-room-temperture structural, magnetic, and ferroelectric transformations in these materials that hold promise for giant piezoelectric, magnetoelectric, and piezomagnetic responses [121,122,123]. To ultimately utilize the potential of highly-strained $BiFeO_3$ thin films in real devices, a thorough understanding of the origins of such strain-induced formation of metastable phases as well as their stability against conventional strain relaxation mechanisms to bulk-like rhomohedral versions of these materials is desirable. Therefore, in this chapter, we begin by examining the thickness- and temperature- dependent evolution of these various phases present in the mixed-phase structures, and the competition between the thermodynamically stable equilibrium rhombohedral phase and these strain-induced polymorphs. We then provide routes to achieve larger electromechanical responses in films *via* chemical alloying strategies that stabilize the mixed-phase structure of highly compressively strained $BiFeO_3$ films to thicknesses that are greater than 500 nm.

4.2 Review on Strain Stabilization of Metastable Phases in Materials

Before we move on to describe the thickness- and temperature dependent evolution of mixed-phase structures in highly strained $BiFeO_3$ films, useful insights can be gained by investigating related work on different mechanisms for strain accommodation and relaxation that are typically observed in material systems [124]. It has long been known that epitaxial thin-film strain has a strong role to play in the evolution of thin-film structure. Typically in a mismatched film-substrate scenario, the film is coherently strained (referred to as a commensurate state) to some point where it becomes too costly energetically to continue to accommodate all the strain in the film. At this point so-called discommensuration (or the formation of strain relieving defects) occurs driving the system into an incommensurate state. The mean separation distance between

these strain-relieving defects generally decreases as the mismatch increases. Often these defects are misfit dislocations that form ordered arrays at the substrate/film interface.[125,126] The density of these misfit dislocations will increase as the film thickness is increased until the total strain in the film is reduced to zero and the lattice parameters return to those of the bulk. Following the nomenclature used by Bruinsma and Zangwill [124], we will refer to coherent-incoherent transitions resulting from a variation in thickness (t) and commensurate-incommensurate transitions resulting from variations in lattice misfit (f).

It has been observed that in metal systems, where dislocation motion is relatively easy, predicted values of critical thicknesses (t_c) and thickness-dependence of coherency loss follow each other closely [127]. Oxide-based systems, however, are widely observed to deviate from these predictions due to large kinetic barriers to dislocation nucleation and migration [128]. Thus in these systems, alternative pathways for strain relaxation are possible – including having the film adopt a crystal structure that is well lattice matched to the substrate, but that is different from the bulk structure of the film material. This process has been referred to as *pseudomorphism* and the pseudomorphic phase is often coherently strained to the substrate. We note that pseudomoph may be a misnomer and that polymorph may be the more accurate term here. Pseudomorphism, which literally means false form, comes from mineralogy and refers to a compound or mineral that has taken on the shape or structure of another mineral. In general this can be mechanical, structural, or chemical in nature. Polymorphism, on the other hand, refers to the ability of a solid material (with a single chemical composition) to exist in more than one form or crystal structure. The study of such polymorphs dates back to the 1950s when alkali halide films were observed to undergo a so-called pseudomorphic phase transformation [129]. Additionally, early molecular beam epitaxy studies found that in certain metal systems, polymorphic phase transitions are possible. For instace, work on Sb [which normally possesses a tetragonal BCC structure (white tin) with a = 5.831Å and c = 3.181Å at room temperature] found that this material adopted a low-temperature diamond structure (grey tin, a = 6.489Å) when deposited on (001) InSb and CdTe (a = 6.48Å) [130]. By undergoing the polymorphic transformation, the Sb avoids an unfavorable lattice mistmatch and strain condition. Likewise, similar results have been obtained for Co films on GaAs [131]. More surprisingly in this case, films of Co <100 nm in thickness were found to grow as a previously unknown, metastable BCC version (a = 2.819Å) on GaAs (110) while films >100 nm were found to transform to the bulk HCP structure.

In light of these experimental observations of strain stabilization of metastable phases, Bruinsma and Zangwill proposed a thickness dependent structural phase diagram as a function of the geometric misfit between the substrate and film and overall film thickness to help explain such effects [124]. These predictions also include an intermediate strain regime where the film evolves from a single-phase, highly-strained metastable structure to a spinodal-modulated, mixed-phase structure before eventual breakdown to microcrystallites of the bulk stable phase. In the sections that follow, we will compare and contrast the features that we observe in the thickness dependent evolution of metastable phases of highly-strained $BiFeO_3$ films on $LaAlO_3$ (001) substrates as well the observation of an eventual breakdown of epitaxy to microcrystallites of the bulk rhombohedral phase with the model proposed by Bruinsma *et al*. [124], and frame these results as a competition between the thermodynamically stable equilibrium rhombohedral phase and the strain-induced polymorphs.

4.3 Thickness Dependent Phase Evolution of $BiFeO_3/LaAlO_3$ (001)

Epitaxial $BiFeO_3$ films of thickness 20-400 nm were synthesized via PLD on single-crystal $LaAlO_3$ (001) substrates using the procedure described in Chapter 2. Detailed structural information of the various films was obtained using high-resolution XRD including θ-2θ scans and reciprocal space maps (RSMs). Typical θ-2θ XRD studies about the 001-diffraction condition of $BiFeO_3$ films of thicknesses 30, 140, 250, and 350 nm (Fig. 4.1) reveal an interesting evolution in structure with thickness. Following the nomenclature established in Chapter 3, the various phases observed are labeled as the rhombohedral parent phase (R-phase, c = 3.96 Å), the intermediate monoclinic phase (M_I-phase, c = 4.17 Å), and the monoclinically-distorted, tetragonal-like phase (M_{II}-phase, c = 4.67Å). The 30 nm thick film exhibits a single peak corresponding to an out-of-plane lattice parameter (c) of ~4.67 Å, consistent with the M_{II}-phase. Upon increasing the film thickness, additional

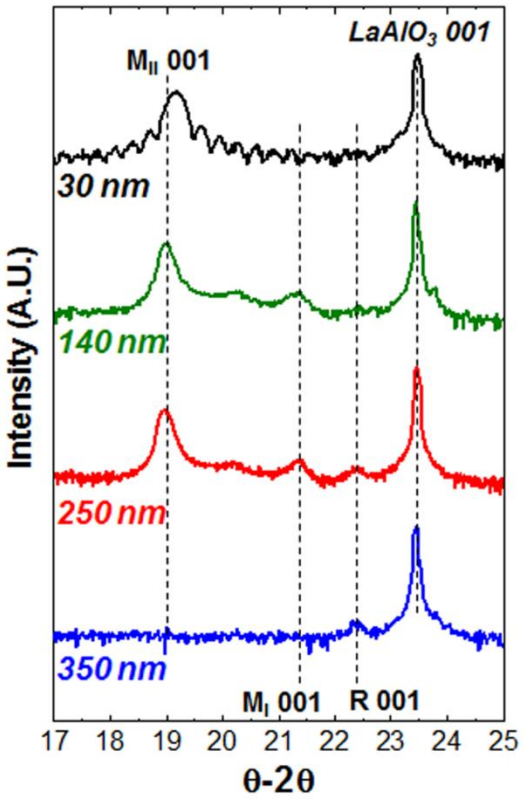

Fig. 4.1: XRD about the 001 diffraction condition of $BiFeO_3/LaAlO_3$ (001) heterostructures for (top-to-bottom) 30 nm, 140 nm, 250 nm, and 350 nm thick films.

peaks corresponding first to the M_I-phase (c = 4.17Å) and subsequently to the bulk-like R-phase (c = 3.967Å) begin to appear. From our studies, we have observed that in films less than ~150 nm, the peak corresponding to the R-phase has very low intensity or is totally absent in some cases. By the time the thickness reaches ~250 nm, the presence of an R-phase peak is more noticeable for most films and by a thickness of ~350 nm only the peak corresponding to the R-phase is observed and all other peaks are completely absent. It should also be noted that the R-phase peak is considerably less intense than the peaks for the M_{II}-phase in the thinner films and, in general, shows lower diffraction intensities throughout the films studied. We also note that the out-of-plane lattice parameter of the M_{II}-phase increases from 4.63Å to 4.68Å as we transition from the 30 nm to 250 nm thick films (Fig. 4.1). This suggests a rather complex thickness dependent evolution and strain relaxation process in these films.

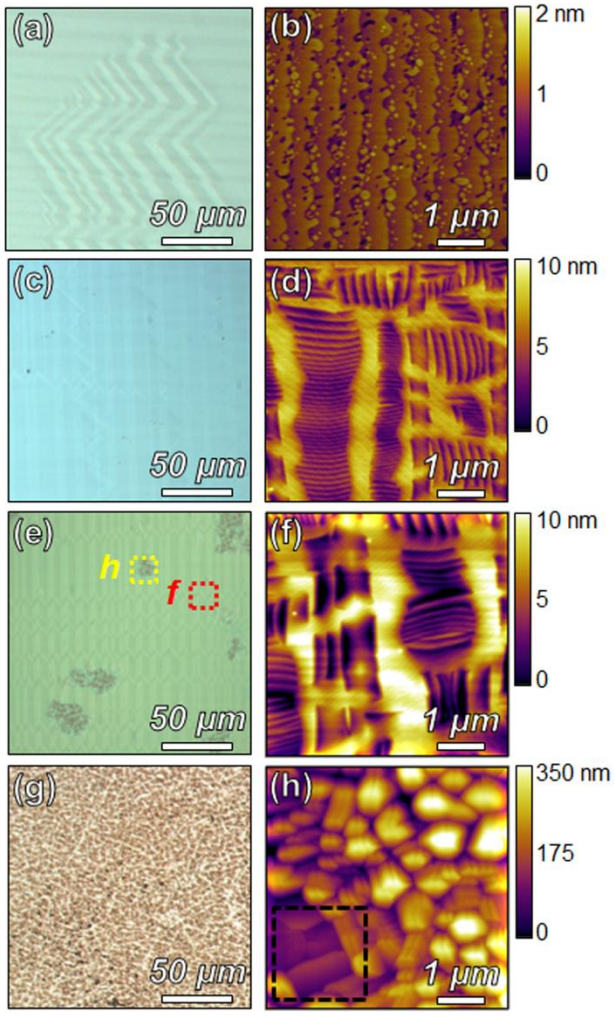

Fig. 4.2: Optical (left) and AFM (right) images of $BiFeO_3/LaAlO_3$ (001) heterostructures of various thicknesses. a) and b) are images for a 30 nm thick film, and c) and d) for a 140 nm thick film. e) reveals formation of different types of structures in 250 nm thick films. Close inspection of the smooth areas (f) reveals results consistent with thinner films and investigation of patchy regions reveals rough microstructure (h). An optical micrograph of a 350 nm thick film (g) is found to possess only the rough microstructure.

Such observations present two important questions: what happens to the M_{II}-phase in thicker films and why does the R-phase peak intensity remain so low even in thick films? Here we develop a detailed picture of the complex behavior observed in these diffraction experiments and provide insight into the thickness-dependent evolution of this complex system. An understanding of the structural evolution is obtained by investigation of the surface topography of these films. We have investigated the surface topography of the films at various magnifications using both optical microscopy and AFM (Fig. 4.2). Under the optical

microscope, the 30 nm thick films are found to have an optically smooth surface (Fig. 4.2a, note also the presence of the structural twins in the $LaAlO_3$ substrate visible in the image), which is consistent with the AFM images (Fig. 4.2b) which exhibits only the M_{II}-phase with atomically smooth terraces, separated by single unit cell step-heights (~4.65Å). Likewise, the optical micrographs of the 140 nm thick films reveal these films to be optically smooth as well (Fig. 4.2c) and upon close inspection using AFM, we observe mixed-phase topography consisting of regions of atomically flat terraces of the M_{II}-phase (bright areas, Fig. 4.2d) and mixed-phase regions consisting of an intimate mixture of the M_I and $M_{II,tilt}$-phases (striped regions, Fig. 4.2d), consistent with the nomenclature adopted in Chapter 3 [117].

Inspection of optical micrographs of the 250 nm thick films, on the other hand, reveal a surface that is mostly smooth with a number of rough regions (Fig. 4.2e). We note that the fraction of these rough regions scales with thickness and does not appear to grow with additional time spent at high-temperatures without additional material being added to the surface. *Ex-situ* anneals at 500-600°C in oxygen for over 20 hours did not result in a change in the fraction of the rough regions. AFM studies of the optically flat regions (red box in Fig. 4.2e, Fig. 4.2f) once again reveal topography consistent with flat terraces of the M_{II}-phase and striped mixed-phase regions. We note that upon increasing the thickness from 140 nm to 250 nm the surface depressions associated with the mixed-phase regions increase greatly from ~7 nm to ~11 nm, respectively. Interestingly, however, AFM studies of the same sample in the rough regions (yellow box in Fig 4.2e, Fig. 4.2h) show a significantly roughened surface with a peak-to-valley height scale of over 200 nm (nearly the entire thickness of the film) without any resemblance to the mixed-phase structures observed elsewhere on this sample. Further inspection of the 350 nm thick films under the optical microscope reveals that the rough regions have grown dramatically to cover the entire film surface (Fig. 4.2g). Analysis of these films with AFM revealed surface morphologies similar to that observed in Fig. 4.2h. The region within the black box in Fig. 4.2h is consistent with regions observed across this and other samples in this thickness range and evokes images of recent advances in the study of $BiFeO_3$ materials – especially the synthesis of $BiFeO_3$ single crystals via the flux growth method [132,133,134]. Fig. 4.3a is a high-resolution AFM image of the area highlighted in Fig. 4.2h and reveals that the rough regions possess micron-sized crystallites with well-defined facets. These features bear a striking resemblance to $BiFeO_3$ single crystals grown by the flux method (Fig. 4.3b) [132] which exhibit large flat (012) surfaces (using the crystallographic

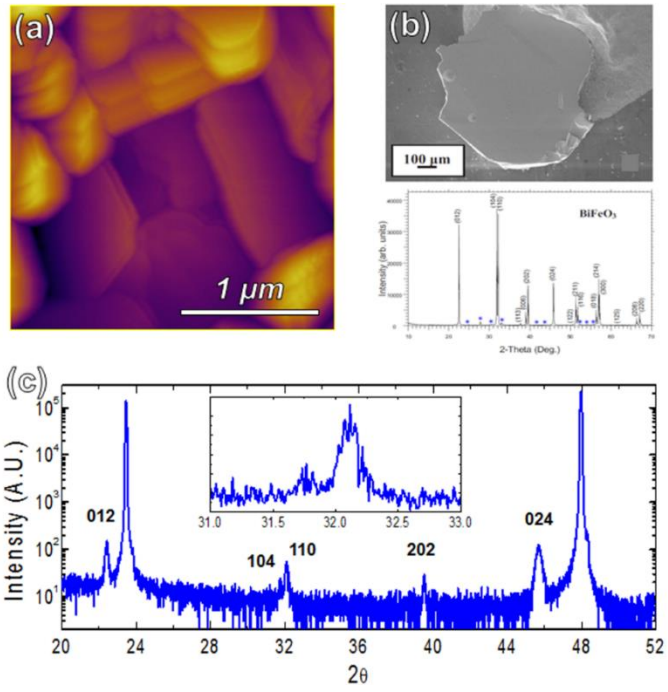

Fig. 4.3: (a) High-resolution AFM image of micron-sized crystallites found in films > 250 nm thick. (b) Image and XRD pattern of a flux grown rhombohedral $BiFeO_3$ sample. Figure courtesy of Ref. 132. (c) XRD pattern of a 350 nm thick $BiFeO_3/LaAlO_3$ (001) heterostructure reveals signatures of the parent rhombohedral phase.

reference frame of the parent rhombohedral structure). Detailed high-resolution XRD scans of our 350 nm samples have allowed us to obtain evidence for a number of peaks corresponding to the bulk-like R-phase of $BiFeO_3$ (Fig. 4.3c). These diffraction patterns can be indexed by peaks corresponding to the most intense reflections from the diffraction patterns of $BiFeO_3$ single-crystals grown by the flux method (bottom, Fig. 4.3b). We have even observed unique features of the bulk R-phase diffraction pattern such as the splitting of the 104- and 110- diffraction peaks in such films. This combination of XRD and AFM strongly suggests that the rough, patchy regions are in fact regions of the bulk-like R-phase of $BiFeO_3$ that grow at the expense of the M_I- and M_{II}-phases in a non-epitaxial manner. We note that for each thickness reported here, we have included in the same growth a $DyScO_3$ (110) substrate for further analysis and comparison of the rhombohedral-like thin film phase. Similar inspection of the co-deposited $BiFeO_3/DyScO_3$ (110) films reveals smooth surfaces (both from optical microscopy and AFM, Fig. 4.4) for all films up to and including the 350 nm thick films and show no evidence of second phases from XRD.

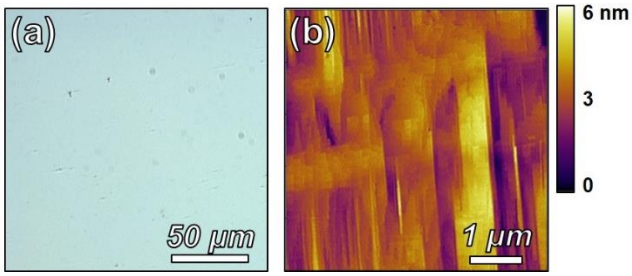

Fig. 4.4: Optical (a) and AFM (b) images of $BiFeO_3/DyScO_3$ (001) of a 350 nm thick film.

4.4 Temperature-Dependent Phase Evolution

We can further our understanding of the mechanism of strain accommodation and epitaxial breakdown in this system by analyzing the change in surface structure of a number of $BiFeO_3$ films

with thickness ranging from 40 nm to 250 nm upon heating from room temperature to 300°C. AFM topography images of films of three representative thicknesses 40 nm (Figs. 4.5a-c), 110 nm (Figs. 4.5d-f), and 250 nm (Figs. 4.5g-i) at three representative temperatures (moving left- to-right, 50°C, 200°C and 300°C) are provided. At any given temperature, the films reveal an increasing fraction of the mixed-phase regions with increasing film thickness (consistent with prior reports) [63]. The reported fraction of the mixed-phase is calculated as the areal fraction of the mixed-phase regions relative to the entire area of the sample (Fig. 4.5j). We also report the depth of the mixed-phase stripe-regions relative to the atomically flat plateau regions of the M_{II}-phase (trench depth, Fig. 4.5k) and the root-mean-square (RMS) roughness of these films which is an indicator of the volume fraction of the mixed-phase regions in these films (Fig. 4.5l). Beginning with the thinnest film reported here (40 nm), we observe that ~20% of the areal fraction of the surface is

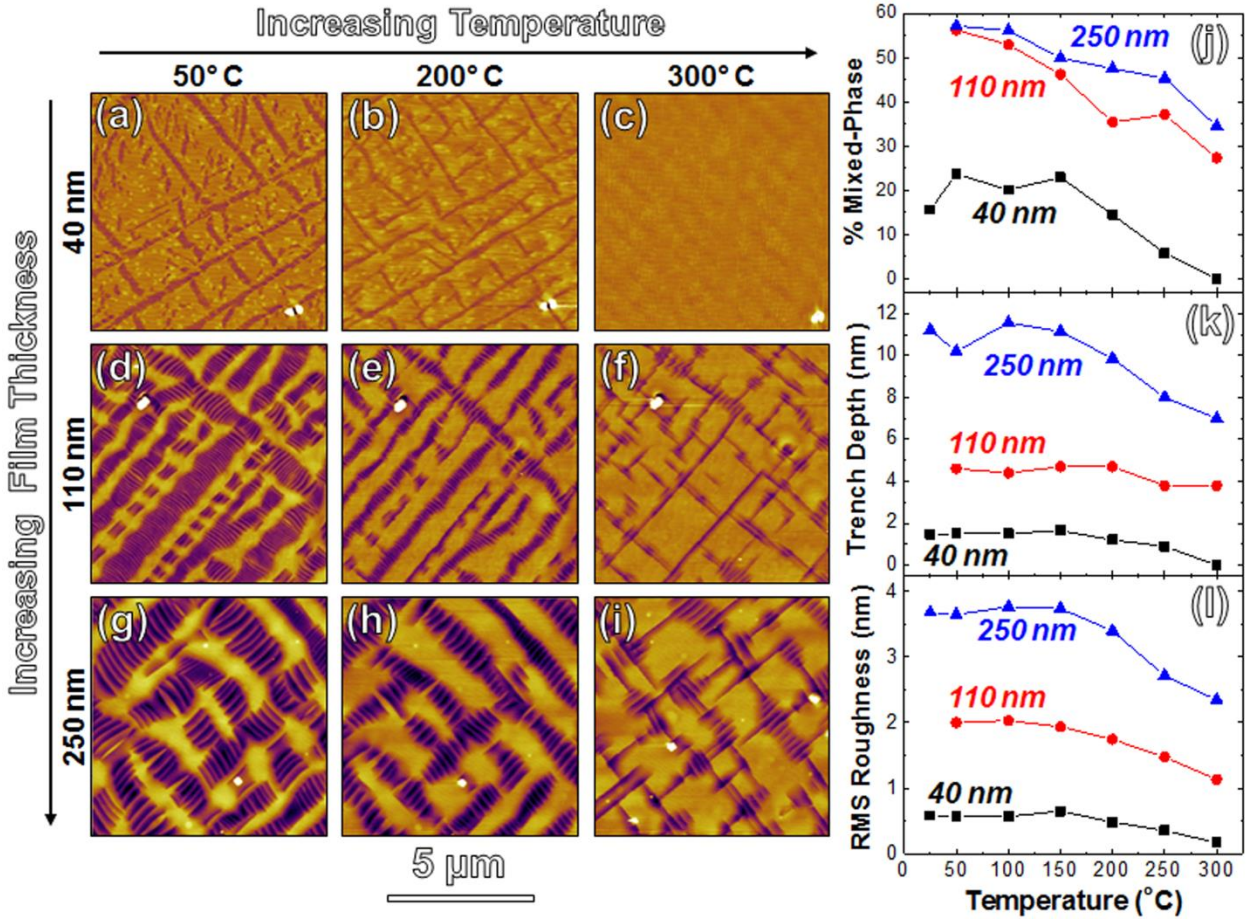

Fig. 4.5: AFM study of the evolution of surface morphology with increasing temperature from 50°C to 300°C for (a) – (c) 40 nm, (d) – (f) 110 nm, and (g) – (i) 250 nm thick films. Corresponding analysis of temperature-dependent evolution of properties including (j) the relative fraction of the mixed-phase structure at the surface, (k) the average depth of the mixed-phase trenches relative to the surrounding M_{II}-phase, and (l) the RMS roughness of the samples. Note the general trend to decrease the fraction of the mixed-phase region with increasing temperature and complete disappearance of the mixed-phase in thinner films.

made up of the mixed-phase regions and that this fraction decreases steadily to zero by 300°C, resulting in a terraced surface with unit cell step-heights corresponding to the M_{II}-phase (Fig. 4.5a-c). We note that similar stripe-like mixed-phase regions are found to reappear upon cooling, but despite similarities in the location of features, they do not appear to have an exact memory for location and fine structure. Similar decreasing trends in the fraction of the mixed-phase are observed for both the 110 nm and 250 nm thick films; however, both of these films still exhibit a significant fraction of mixed-phases even at 300°C (the maximum we can achieve in our scanning probe system). Thus, we conclude that the temperature at which the film transforms to being composed entirely of the M_{II}-phase is a function of the film thickness and is higher for thicker films. This suggests that the films form the mixed-phase upon cooling down from the growth temperature and there exists a critical thickness at which the film will stabilize in the mixed-phase structure even at the growth temperature of 700˚C.

4.5 Mechanism of Mixed-Phase Formation

As illustrated by the AFM experiments, these samples exhibit a temperature induced reduction in the fraction of the mixed-phase. We note that these results are consistent with the work in the supplementary materials of Ref. 63 where phase field simulations suggest a driving force for the stabilization of the highly-distorted M_{II}-phase with increasing temperature. We see that films up to a thickness of 35 nm grow as the M_{II} phase which is stable down to room temperature. However, in thicker films (40-200 nm) we contend that the samples grow as a fully strain-stabilized, M_{II}-phase at 700°C and upon cooling, the mixed-phase structures are formed to accommodate the increase in strain energy. This suggests that the formation of the mixed-phase structure stabilizes the strained film at lower temperatures. It would appear that in this system, that instead of generating misfit dislocations in the sample, the material undergoes partial relaxation via the formation of the M_I- and $M_{II,tilt}$- mixed-phase regions. We also note that these mixed-phase stripe bands generally form 2D arrays on the sample of the surface with the long-axis of bands running along [100] and [010] in-plane directions. Such a configuration has parallels to classic 2D arrays of misfit dislocations.

We can better understand the nature of the formation of such mixed-phase structures during the cool-down process by investigating the energetics of the system. Figs. 4.6a-c show a schematic of the free energy landscape for films with thickness between 40-200 nm as a function of substrate induced strain ε at different temperatures. Here we focus on a film with a thickness of 40 nm as an

example. Theoretical calculations and experimental studies have suggested the presence of a number of different structural varieties of distorted $BiFeO_3$ with a range of *c/a* lattice parameter ratios [119,135,136], the most important of which for this discussion are the parent R-phase and the highly-distorted, strain induced M_{II}-phase. Thus the energy landscape should be characterized by at least two local minima corresponding to these two phases. At the growth temperature (700°C), we can thus draw a schematic energy diagram as a function of thin film strain (Fig. 4.6a). Consistent with previous experimental and density functional theory studies, growth at low strain levels (less than ~4% compressive strain) results in the formation of films possessing the R-phase structure while growth at strain levels in excess of 4% result in stabilization of the M_{II}-phase. Since the R-phase is the thermodynamically stable equilibrium phase at low-temperature and strain, the effect of cooling the film down from the growth temperature is to shift the energy minima for the strained metastable M_{II}-phase to higher energies and strains relative to the R-phase. Thus, as we cool the film from the growth temperature down to 300°C, the energy curves shift as noted. The region within the interval $[\varepsilon^-, \varepsilon^+]$ with a negative curvature for the free energy forms a strain-induced spinodal and in this interval of substrate-induced strain, the film spontaneously splits to a modulated mixed-phase structure of alternating R- and M_{II}-like phases. The region of negative curvature shifts towards the strain condition for the film on the $LaAlO_3$ substrate upon cooling from the growth temperature (Fig. 4.6b). Therefore, at room temperature the $LaAlO_3$ substrate forces the strain condition of the film into the strain-induced spinodal (Fig. 4.6c) [124,137]. In this region, the film is mechanically unstable against local strain wave distortions and this drives a lowering of the energy by spontaneous deformation to the mixed-phase structures along the easy strain axes (<100>).

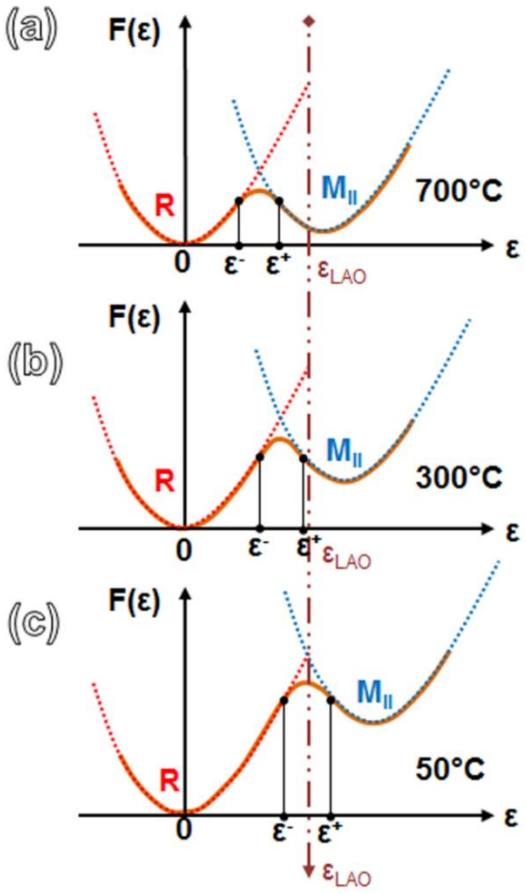

Fig. 4.6: Schematic illustration of the anticipated evolution of free energy of the system as a function of thin film strain. Upon transitioning from (a) 700°C to (b) 300°C to (c) 50°C we anticipate movement of the free energy curves such that spontaneous formation of the mixed-phase structures occurs as noted.

Therefore, films exposed to these strain conditions, as a result of the interplay between thermal expansion mismatch, epitaxial strain, and thermodynamic phase stability, will spontaneously separate into a modulated mixed-phase structure of alternating R-like and M_{II}-like phases in the $BiFeO_3$ system.

4.6 Epitaxial Breakdown in Thicker Films

The majority or our discussion thus far has focused on films with thickness less than 200-250 nm, but beyond this critical thickness we have observed epitaxial breakdown in these films. We now focus on the nature of this epitaxial breakdown. Fig 4.7a is a SEM cross-section of a 250 nm thick $BiFeO_3/LaAlO_3$ (001) films that was observed to have a small fraction of the rough regions reported in the optical micrographs (Fig 4.2e). The presence of these rough regions marks the initial onset of epitaxial breakdown of the film. The SEM cross-section cuts across the optically smooth regions as well as the rough region (Fig. 4.7a). A closer look at the cross-section of the optically smooth regions (blue box, Fig. 4.7a, Fig. 4.7b) reveals a mixed-phase structure composed of alternating regions of M_I- and $M_{II,tilt}$-phases with sharp well-defined interfaces (emphasized by the yellow dotted lines). Focusing, in turn, on the interface between the smooth and rough regions (orange box in Fig. 4.7a, Fig. 4.7c) we observe the formation of micro-crystallites of the bulk R-phase (consistent with AFM and XRD studies) and that the breakdown, once initiated, is not limited to the surface but occurs through the entire thickness of the film. Note that the peak-to-valley roughness in these rough regions are found to be, in general, a good fraction of the entire film thickness. A cross-sectional

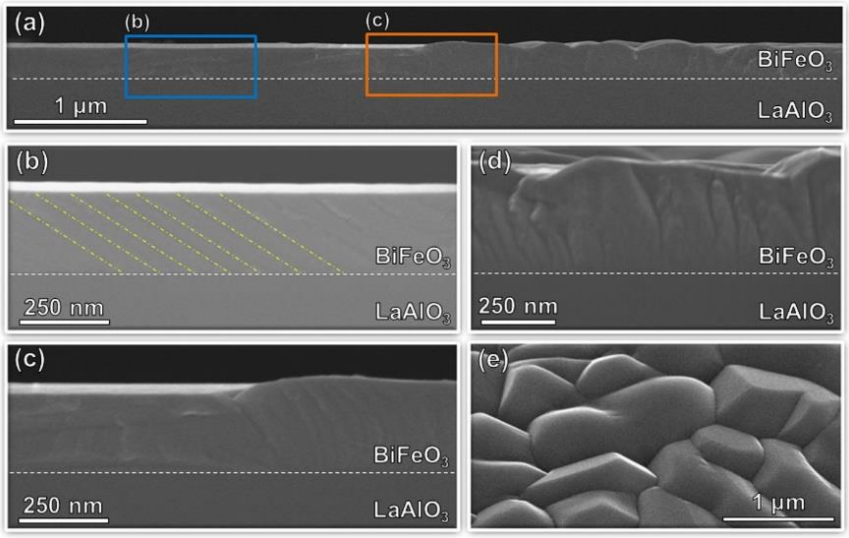

Fig. 4.7: Cross-sectional scanning electron microscope analysis of a 250 nm $BiFeO_3$ / $LaAlO_3$ (001) heterostructure. a) Low-resolution view of sample shows transition from smooth to rough patches. b) Close inspection of smooth areas reveals the presence of contrast consistent with mixed-phase region. c) The rough, patchy regions are found to extend throughout the thickness of the film and have a fairly sharp boundary between regions. Analysis of thicker (350 nm) films reveals the presence of fully epitaxial breakdown with uniform structure throughout the thickness of the film (d) and the presence of faceted crystallites on the surfaces (e).

image of a 350 nm thick film (Fig. 4.7d) is that reveals a complete breakdown of the film. Plan-view images (Fig. 4.7e) of the film reveal the presence of sharp faceted microcrystallites of the R-phase over the entire surface indicating a complete breakdown of epitaxy.

4.7 Thickness-Strain Phase Diagram for $BiFeO_3$

Based on the results so far, we can construct a structural phase diagram (Fig. 4.8a) at the deposition temperature of 700°C to help explain the evolution of the complex structure and morphology of these highly-strained $BiFeO_3$ films as a function of increasing film thickness. Understanding of the evolution of these structures at the growth temperature is important since there are some structural evolutions that are not reversible (*e.g.*, epitaxial breakdown) and thus the final structure of some phases will be set at the growth temperature. In the following discussion we will also elaborate on additional structural evolution that would occur during cooling as necessary. We note that this phase diagram is similar to the diagram proposed by Brunisma and Zangwill [124] for unrelated systems. The diagram shows the expected microstructure of the film as a function of epitaxial lattice mismatch between film and substrate and film thickness. Focusing first on the lattice misfit corresponding to the $LaAlO_3$ substrate, we note that for thickness < 200 nm films grow (at 700°C) in the pure M_{II}-phase and are coherently strained to the substrate (Fig. 4.8b). The growth is expected to occur in a layer-by-layer or step-flow growth mode as the resulting M_{II}-phase regions reveal atomically flat terraces following growth. Note that films in excess of 35 nm will undergo a temperature-induced spinodal phase separation upon cooling. As the films with the strain-stabilized M_{II}-phase grow in thickness, so does the cost in free energy compared to the ground-state R-phase. At a critical thickness, energetics require that the films undergo a first order transformation to the bulk, stable crystal structure. However, large crystallographic deformations and geometric constraints associated with such a transformation present substantial kinetic barriers to the nucleation and transformation to the bulk, stable phase and this prevents the observation of the true equilibrium structure. As the film thickness approaches ~250 nm it enters the regime of high-temperature, thickness-driven, strain-relaxation-induced spinodal instability and forms a strain modulated structure of alternating M_I and $M_{II,tilt}$ phases at the growth temperature of 700°C (Fig. 4.8c). The spontaneous transformation to the mixed-phase structure is accompanied by surface topography with depressions that are easily several nanometers deep (roughly 4-5% of the film thickness) and results in the significant roughening of the growth front (i.e., the saw-tooth structure described in Chapter 3). Several

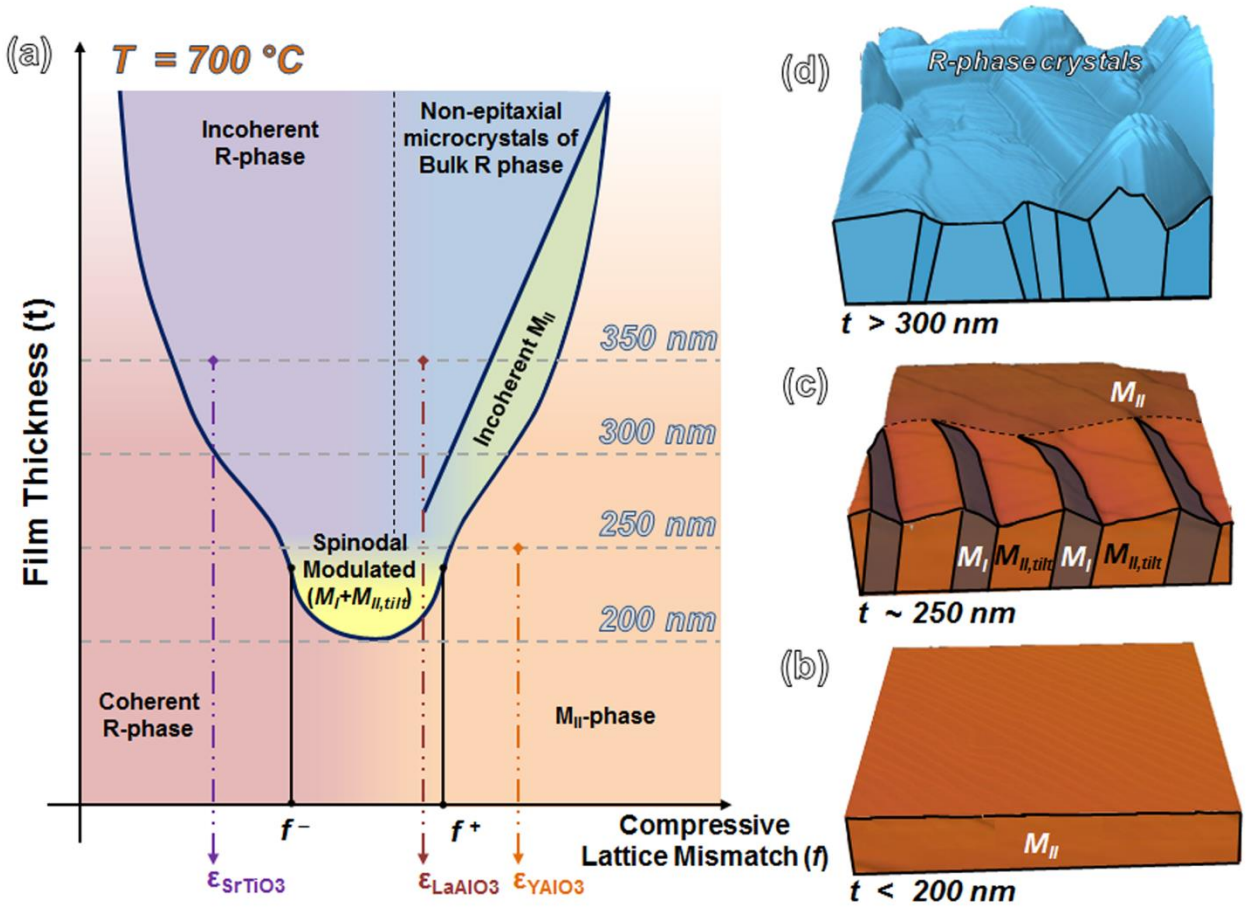

Fig. 4.8: (a) Schematic phase diagram showing the evolution of the microstructure as a function of epitaxial lattice mismatch (*f*) and film thickness (*t*). At the lattice mismatch expected between $BiFeO_3$ and $LaAlO_3$ we expect three different stages of growth: (b) coherent growth of the highly-distorted M_{II}-phase in thin films, (c) relaxation by formation of spinodal modulated structure of the M_I- and $M_{II,tilt}$ -phase at intermediate thicknesses, and (d) eventual relaxation and transformation to non-epitaxial microcrystals of bulk R-phase.

theoretical and experimental studies of systems undergoing spinodal phase separation and concomitant roughening of the growth front have demonstrated changes in growth mode resulting in film-to-island morphological transitions, including possible film break-up [138,139]. Moreover, such a mixed-phase structure with periodic interphase boundaries and surface structures significantly lowers the kinetic barriers to the nucleation of the bulk R-phase and as it approaches a thickness of 300-350 nm, the film breaks down to non-epitaxial microcrystallites of the bulk R-phase at 700°C (Fig. 4.8d). Arresting growth between the 250-300 nm thickness and cooling to room temperature results in films exhibiting a mixture of the rough regions corresponding to epitaxial breakdown and mixed-phase regions with some fraction of the flat plateaus of the M_{II}-phase and the mixed-phase bands possessing the M_I- and $M_{II,tilt}$-phases. We summarize the expected structure at the growth temperature (700°C), an intermediate temperature (300°C), and room temperature (25°C) for films of various thickness in Table 4.1.

Furthermore, this phase diagram is consistent with previously observed work on $BiFeO_3$ thin films grown on other substrates. For instance, growth of $BiFeO_3$ on $YaAlO_3$ (110) substrates (a = 3.71Å, large lattice mismatch, Fig. 4.8a) has been found to result in essentially phase-pure M_{II}-phase films up to thicknesses of 225-250 nm [63]. Likewise much work on $BiFeO_3$ thin films on $SrTiO_3$ (001) substrates [a = 3.905Å, small lattice mismatch, Fig. 7a] has been reported and it has been observed that $BiFeO_3$ films will relax to incoherent (relaxed) films at thicknesses in excess of a few hundred nanometers [119]. Such results are consistent with this proposed diagram. Based on such an understanding of the complex strain-dependent evolution of phases in $BiFeO_3$, we next explore conventional chemical alloying or chemical pressure based strategies that can help to stabilize the mixed-phase structures that form highly compressively strained $BiFeO_3$ to much higher thicknesses than what is possible in the case of pure stoichiometric films.

4.8 Mixed-Phase Stabilization *via* Chemical Alloying

This transformation of the mixed-phase samples to the R-phase could be problematic for some applications that require large electromechanical responses. Such responses are made possible by the sample's ability to transform under applied electric field between the M_I-, M_{II}-, and $M_{II,tilt}$-phases. Thus in order for large electromechanical responses to be made possible, it is imperative that one can stabilize such structures in thicker films to allow for larger field-induced surface displacements. In the remainder of this chapter, we demonstrate one route to stabilize such mixed-phase structures through chemical alloying and lattice parameter/strain engineering in these films. In particular, we focus on the synthesis of lead-alloyed $BiFeO_3$ thin films of thickness between 20-600nm from $Bi_{1-x}Pb_xFeO_3$ targets where x = 0, 0.25, and 0.50.

Following growth, the stoichiometry of these films was probed via XPS and RBS. Due to the similar masses of Pb and Bi, RBS alone was not sufficient to accurately probe the cation chemistry of these samples. Calibrated XPS studies revealed stoichiometry transfer of species to the target, but a combination of high growth temperature, the high vapor pressure (and, in turn, volatility of Pb), and the re-evaporation of Pb from the films as a self-compensation method lead to sizeable Pb-loss. Fig. 4.9 shows a sampling of the results from the XPS studies in which the relative intensities of the Pb 4*f*/9 and Bi 4*f*/8 core electron peaks were used to obtain the chemical composition with the assumption that the number of electrons recorded is proportional to the number of atoms present. Fig. 4.9a shows the XPS spectrum from a polished $(Bi_{0.5}Pb_{0.5})_{1.1}FeO_x$ target demonstrating that our targets do indeed possess the anticipated stoichiometry. Additionally,

this spectrum was used as a calibration for the films to complete quantitative analysis of the composition. Fig. 4.9b shows the XPS spectrum from a thin film grown from this same target at room temperature. This analysis reveals that the laser conditions used in the growth nicely maintain the stoichiometry during the transfer of material from target to substrate. Quantitative analysis using the target as a calibration suggests nearly perfect maintenance of the 50:50 ratio within the error of the study. Fig. 4.9c, however, is the XPS spectrum from growth of a film from the same target at the growth temperature of 700°C. The XPS spectrum reveals significantly diminished peak intensity for the Pb 4*f*/9 peak. Quantitative analysis of the spectrum suggests a Pb-content of ~3% or a chemical formula of $Bi_{0.97}Pb_{0.03}FeO_3$. Fig. 4.9d focuses on the Pb 4*f*/9 peak for films grown at 700°C for the three targets used in this study and reveals that growth from $(Bi_{1-x}Pb_x)_{1.1}FeO_x$ targets with x = 0, 0.25, and 0.50 resulted in final films with [Pb]/[Bi+Pb] fractions of 0%, 1%, and 3%, respectively. The overall chemical composition of the films, in particular the [Bi+Pb]-to-[Fe] ratio was then probed via RBS (Fig. 4.10). We attempted fits assuming only Bi in the film and with a mixture of Bi and Pb in the right ratios and, within the

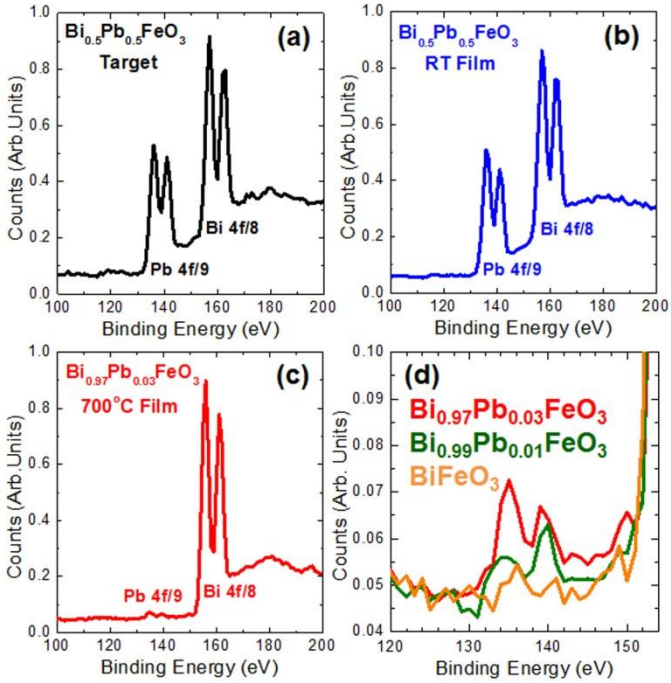

Fig. 4.9: XPS results from a range of samples including: (a) starting $(Bi_{0.5}Pb_{0.5})_{1.1}FeO_x$ target, (b) a film grown from the same target at room-temperature, (c) a film grown from the same target at 700°C, and (d) a comparison of the Pb-peaks from the growth at 700°C from the three targets used in this study.

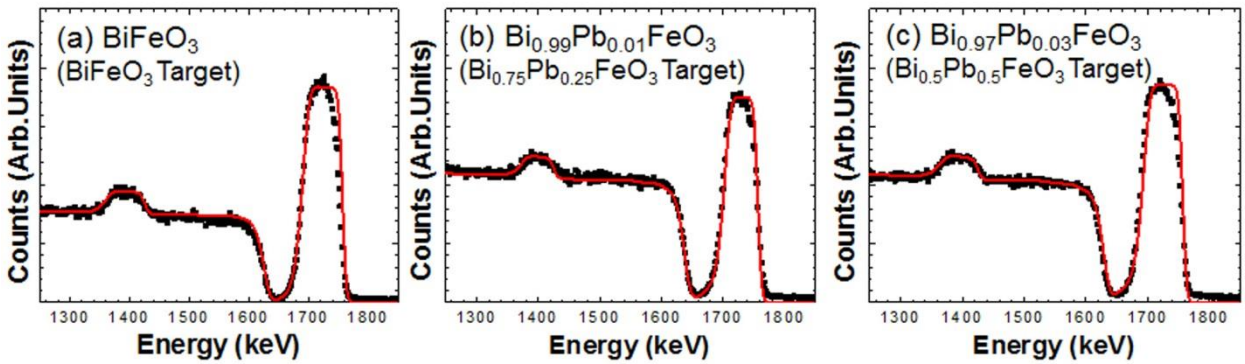

Fig. 4.10: RBS results for films grown at 700°C from $(Bi_{1-x}Pb_x)_{1.1}FeO_x$ targets with (a) x = 0, (b) x = 0.25, and (c) x = 0.50. Dots show experimental data and the line shows the best fit result.

accuracy of the RBS data (typically a 1-2%) all films show a 1-to-1 [Bi+Pb]-to-Fe ratio. This confirms that the films are mildly alloyed with Pb, but otherwise possess the expected chemical structure for these films.

Detailed studies of evolution of structure and topographical features with Pb-alloying were also conducted on these films. Following the nomenclature laid out in Chapter 3, the various phases present in these highly strained films are expected to be the rhombohedral parent phase (R-phase, c = 3.96Å), the highly distorted intermediate monoclinic phase (M_I-phase, c = 4.17Å, tilted ~2.8° from the substrate normal), the highly-distorted tetragonal-like phase (M_{II}-phase, c = 4.67Å), and a tilted version of the M_{II}-phase ($M_{II,tilt}$-phase, c = 4.67Å, tilted ~1.6° from the substrate normal). Previous studies have shown that the mixed-phase regions of these samples are made up of an intimate mixture of the M_I- and $M_{II,tilt}$-phases. As evidenced by AFM images of 100 nm thick films of $Bi_{1-x}Pb_xFeO_3$ (x = 0, 0.01, and 0.03) (Fig. 4.11a-c, respectively) the surface areal fraction of the mixed-phase regions (stripe-like features) is observed to scale inversely with the Pb-content (Fig. 4.11d). Upon introducing only 3% Pb into the system the areal fraction of the mixed-phase regions is observed to decrease by ~12% from that of the $BiFeO_3$ film.

In order to better understand this effect, we have undertaken a series of high-resolution RSM studies of a number of diffraction peaks to develop a complete picture of the structural changes induced by the Pb-alloying. RSMs of the 103- (Fig. 4.11e-g) diffraction peaks for the M_{II}-

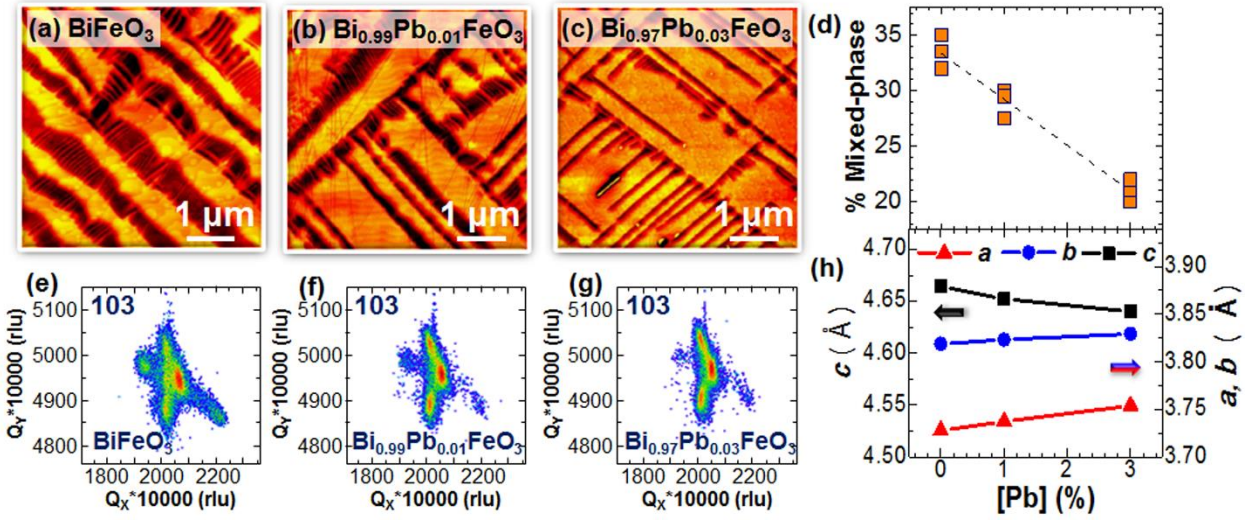

Fig. 4.11: AFM images of 100 nm thick (a) $BiFeO_3$, (b) $Bi_{0.99}Pb_{0.01}FeO_3$, and (c) $Bi_{0.97}Pb_{0.03}FeO_3$ thin films on $LaAlO_3$ (001) substrates. (d) Evolution of the areal percentage of the mixed-phase regions on these samples as a function of Pb-content. (e), (f), and (g) are reciprocal space maps of the 103-diffraction condition for $BiFeO_3$, $Bi_{0.99}Pb_{0.01}FeO_3$, and $Bi_{0.97}Pb_{0.03}FeO_3$, respectively. (h) In-plane (a and b) and out-of-plane (c) lattice parameters of the M_{II}-phase as a function of Pb-content as determined from the reciprocal space maps.

phase of the 100 nm thick $Bi_{1-x}Pb_xFeO_3$ (x = 0, 0.01, and 0.03) films reveal a splitting of the peak into three-peaks. These results are consistent with prior studies of this phase and confirm that the M_{II}-phase is monoclinically distorted, with a small tilt along the <100> in-plane directions [109,110,117,119,140]. Furthermore, we note that the side-lobes on either side of the main diffraction peak in Q_x-space are observed to greatly decrease in intensity with increasing Pb-content. This corresponds to a systematic reduction in the fraction of the $M_{II,tilt}$-phase observed in these films, is consistent with the AFM analysis, and with an overall decrease in the fraction of the mixed-phase regime with increasing Pb-content. From these (and other RSM studies, not shown), we can summarize the effect of Pb-alloying on the unit cell of the M_{II}-phase (Fig. 4.11h). Overall, the addition of Pb to the $BiFeO_3$ structure results in an increase of the *a*- and *b*- and a decrease of the *c*-lattice parameter of the material. Such a change in the structure could be the consequence of both the larger ionic radius of Pb^{2+} (assuming twelve-fold coordination, 149 pm compared to 138 pm for Bi^{3+}) and/or the formation of oxygen vacancies that could accompany the introduction of the Pb^{2+}. Key to the enhanced stabilization of the M_{II}-phase is the fact that the Pb-alloying seems to predominantly manifest itself in the form of an increase in the in-plane lattice parameters. The *a*-lattice parameter, for instance, is 3.74Å, 3.75Å, and 3.76Å for the $Bi_{1-x}Pb_xFeO_3$ films for x = 0, 0.01, and 0.03, respectively. Thus the Pb-alloying reduces the lattice mismatch between the M_{II}-phase and the $LaAlO_3$ substrate (a = 3.79 Å), further stabilizing the M_{II}-phase, allowing thicker films to be produced prior to relaxation and promoting thicker films with the sought after mixed-phase structures. We note that among the common Bi-site dopants studied for $BiFeO_3$ only Pb^{2+} and Ba^{2+} (ionic radius of 161 pm, 12-fold coordination) should provide the impetus to further stabilize the tetragonal-like phase of $BiFeO_3$. This is consistent with the work of Christen *et al.* who observed that Ba-alloying upwards of 8% resulted in a decrease of the monoclinic distortion in the M_{II}-phase and a change in the lattice parameters [119].

We have also investigated the effect of lead-alloying on electromechanical properties of the mixed-phase films using PFM-based local switching studies. We reiterate that large surface strains of 4-5% are obtained upon electric-field switching of mixed-phase $BiFeO_3$ samples. Our studies have revealed that the key parameter at play in allowing for the large electromechanical responses is the relative ratio of the various phases in the mixed-phase structures. Since the Pb-alloying alters the areal fraction of the mixed-phase regions significantly, it is important to normalize data appropriately – here we use the areal fraction of the mixed-phase regions as a means

of normalization. Thus, we report the response both in total magnitude and in nanometers per areal percent of mixed-phase. We have completed local poling on 100 nm $Bi_{1-x}Pb_xFeO_3/LaAlO_3$ (001) films with x = 0, 0.01, 0.03 (Fig. 4.12). Consistent with prior results, we observe reversible electromechanical deformations of 4-5% for $BiFeO_3$ thin films as we transition from the as-grown (Fig. 4.12a) to the electrically poled state (Fig. 4.12b). Line traces across the electrically poled region are provided in Fig. 4.12c. Similar results are obtained for the $Bi_{0.99}Pb_{0.01}FeO_3$ thin films were we can likewise electrically transform the mixed-phase regions (Fig. 4.12d) to a region of pure M_{II}-phase (Fig. 4.12e) resulting in a net surface displacement (Fig. 4.12f). We note that the absolute magnitude of the response is diminished slightly, but the response normalized to the total fraction of the mixed-phase is the same if not slightly enhanced as compared to the $BiFeO_3$ sample. This same trend is further observed in the $Bi_{0.97}Pb_{0.03}FeO_3$ films [Fig. 4.12g-i]. We observe that the surface strain per unit areal fraction of the mixed-phase region increases from 0.13 nm/% for $BiFeO_3$ films to 0.16 nm/% nm for $Pb_{0.97}Bi_{0.03}FeO_3$ films. This is an indication that thicker films of Pb-alloyed $BiFeO_3$ with similar surface fractions of mixed phase regions will yield a higher net surface displacement in electric-field-induced switching experiments and comparable, if not improved, overall displacement.

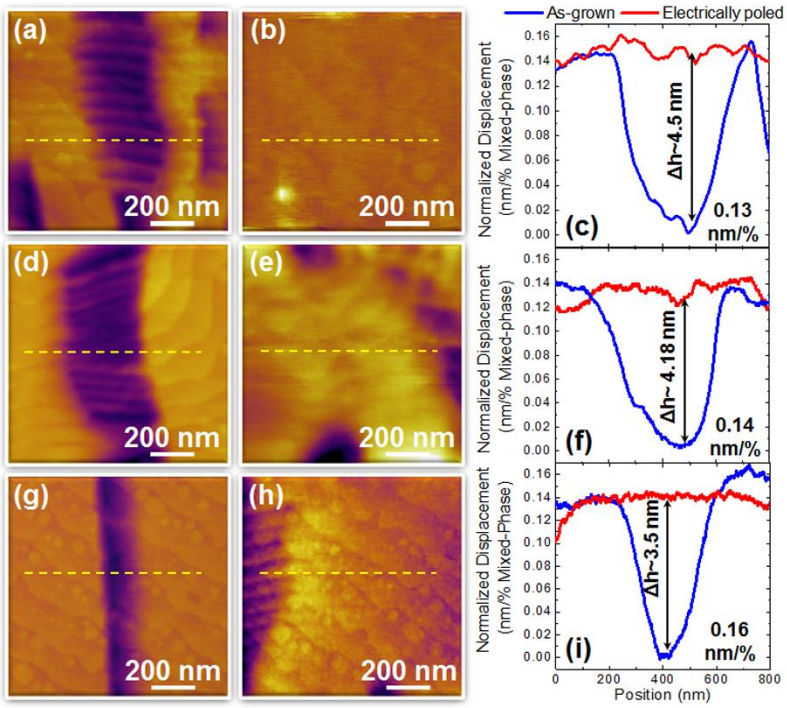

Fig. 4.12: AFM images and corresponding line traces at the dashed line for as-grown (left) and electrically poled (right) 100 nm thick films of (a), (b), and (c) $BiFeO_3$, (d), (e), and (f) $Bi_{0.99}Pb_{0.01}FeO_3$, and (g), (h), and (i) $Bi_{0.97}Pb_{0.03}FeO_3$. Note that the height scales in (c), (f), and (i) are normalized to the fraction of mixed-phase regions on these samples for direct comparison.

To investigate this idea, we studied thick films (300-500 nm) of $Bi_{0.99}Pb_{0.01}FeO_3$ and $Bi_{0.97}Pb_{0.03}FeO_3$ to probe the evolution of phase stability. Fig. 4.13a shows a 10 x 10 micron scan of a 500 nm $Bi_{0.99}Pb_{0.01}FeO_3/LaAlO_3$ (001) sample that reveals the presence of the commonly

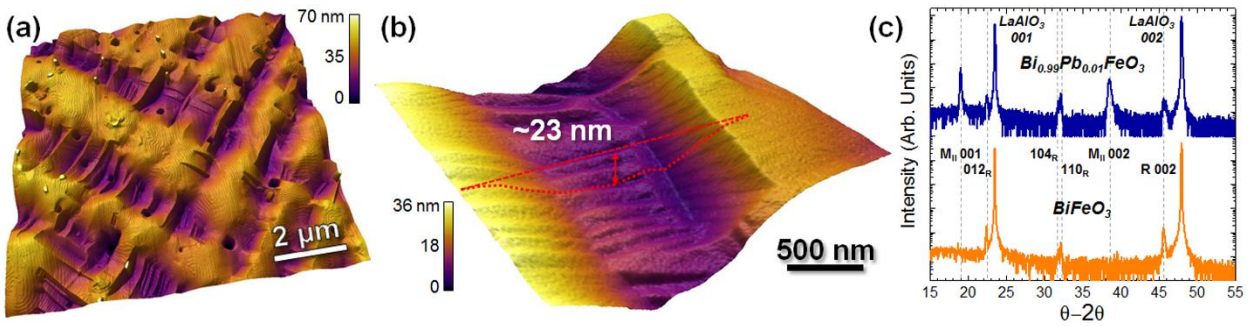

Fig. 4.13: (a) Large scale and (b) zoom-in AFM image of a 500 nm thick $Bi_{0.99}Pb_{0.01}FeO_3/LaAlO_3$ (001) thin film revealing the ability to stabilize the mixed-phase structures necessary for large electromechanical response into thick films. Line-trace across the mixed phase region reveals a surface depression of ~23 nm and the capacity for large electromechanical responses. (c) XRD results from a (orange data) 300 nm $BiFeO_3$ film showing complete breakdown and a 500 nm $Bi_{0.99}Pb_{0.01}FeO_3$ film showing the presence of the M_{II}-phase.

observed mixed-phase regions required for the large electromechanical response. Upon closer inspection (Fig. 4.13c), however, it is evident that these mixed-phase regions possess dramatically increased surface depressions compared to other samples studied. Line traces across the mixed-phase region on this 500 nm thick film reveal surface depressions of ~23 nm. This implies that significantly enhanced surface height changes can be observed in these films. To date we have observed the ability to reversible switch films upwards of 300-350 nm thick (resulting in electromechanical responses as large as 12-14 nm), but have been limited by the lack of a bottom-electrode to enable switching of films in excess of 400-450 nm. Nonetheless, XRD studies reveal that 350 nm thick $BiFeO_3$ thin films possess no evidence of the M_{II}-phase and the mixed phase structures while 500 nm thick $Bi_{0.99}Pb_{0.1}FeO_3$ thin films possess a large fraction of the M_{II}- and mixed-phase structures (Fig. 4.13c). Overall, Pb-alloying, even in very small amounts, can exact a strong impact on the structure of these materials and helps to stabilize the structures and could enhance overall material performance.

4.9 Conclusions

The thickness-, temperature-, and chemistry- dependant evolution of mixed-phases studied in this chapter have added to our understanding of these complex and technologically exciting phase boundaries in highly-strained $BiFeO_3$ thin films. The presence of a variety of polymorphs of the $BiFeO_3$ is essential for the strong electromechanical response in these films. We observe, however, that these structures are limited by a thickness-dependent breakdown and irreversible transformation to a non-epitaxial R-phase. We have examined the thickness- and temperature-dependence of these structures and have constructed schematic energy and phase diagrams to help

explain the structural evolution of these materials. We have drawn parallels to observations of unusual strain-relaxation in more simplistic metallic systems and have applied a model for spinodally-modulated structures to $BiFeO_3$. The ability of the $BiFeO_3$ system to take on a variety of pseudomorphs provides one route to strain relaxation in this system and due to the complex interplay of lattice and electronic order in these materials this results in strong electromechanical responses. Our observations provide new insights into the nature of the phase evolution in highly compressively strained $BiFeO_3$, the stability of the various polymorphs, and are consistent with previously observed structures in a variety of epitaxial $BiFeO_3$ films. Equipped with such an understanding of the thickness-driven breakdown of epitaxy, we can begin to construct pathways to stabilize the desired mixed-phase structures in these exciting and technologically relevant materials. In particular, we have identified that strain engineering via suitable chemical-alloying can delay the onset of epitaxial breakdown in these films and stabilize the necessary nanostructure to assure strong electromechanical responses. By alloying the $BiFeO_3$ with Pb (1-3%) we have stabilized the mixed-phase structures to film thicknesses in excess of 500 nm and have demonstrated surface height depressions greater than 20 nm. These observations provide insight into the nature of the phases of $BiFeO_3$ and their stability and routes to further utilize these materials.

CHAPTER 5

ENHANCED ANISOTROPIC DEFORMATION STATES AND T_C IN $BaTiO_3$ FILMS *VIA* STRAIN-INDUCED DEFECT DIPOLE ALIGNMENT

In this chapter, we explore a new way of inducing anisotropic lattice deformation in materials, involving the use of a combination of defect and strain engineering. More specifically, we will utilize the high energy nature of the PLD growth process to tune the concentration of bombardment-related point defects that occur in $BaTiO_3$ thin films, that in turn form charged point defect complexes known as defect dipoles. We then present a systematic study that correlates the anomalous lattice expansion as well as the observed ferroelectric hysteresis loop offsets to the elastic dipole and the electric dipole of the defect-dipoles that are aligned in the out-of-plane direction of the films. We propose a new mechanism for defect-dipole alignment involving a coupling of the elastic moment of defect-dipole complexes to the stress field from epitaxial constraints. We then demonstrate dramatic enhancements in the ferroelectric T_C for films with high densities of aligned defect dipoles and show that the enhancements are consistent with results based on phenomenological GLD calculations where the defect-related anisotropic lattice deformation is simply modeled as an excess out-of-plane strain on defect free $BaTiO_3$. We also demonstrate ferroelectric Curie temperatures exceeding 800-1000°C on $BaTiO_3$ thin films and our studies suggest that growth induced defect-dipoles aligned under epitaxial constraints can be potentially used to tune the strain state of materials.

5.1 Introduction

In Chapter 3, we demonstrated strain-induced mixed phase formation in highly compressively strained $BiFeO_3$ as a new route to engineer highly enhanced electromechanical responses in ferroelectric thin films. Other examples of epitaxial strain-induced ferroelectric property enhancements include the elevation of ferroelectric T_C of $BaTiO_3$ by several hundreds of degrees, as well as the emergence of room-temperature ferroelectricity in the otherwise quantum paraelectric $SrTiO_3$.[48,60,61,141] Despite considerable excitement over the potential for thin-film strain to control materials, it is fundamentally limited in a number of ways: 1) the magnitude of the strain that can be applied before the onset of relaxation is relatively small (generally <1% lattice mismatch), 2) the thickness of a coherently strained film must be maintained below a critical thickness to avoid strain relaxation which often renders such strain-engineered films unsuitable for applications that require high voltages, and 3) there is a lack of continuous tunability arising from the limited number of substrates and the need to switch between them to change the strain state. In turn, these factors put rather stringent limits on our ability to manipulate the properties and enhance performance on demand in these materials and also motivates the need to invent new pathways to engineer strain in materials. At the same time, we have seen from PLD growth optimization experiments of $BaTiO_3$ films (see Chapter 2), that films grown at laser fluences exceeding 1.5 J/cm^2 resulted in films with expanded out-of-plane lattice parameters beyond what is expected from epitaxial strain alone. In this chapter, we trace back through literature to understand the possible origins of such unexplained lattice expansions, as well as the possibility of using these effects to achieve property enhancements in a manner similar to that what has been demonstrated from purely strain-based effects.

5.2 Anomalous Lattice Expansion from High Energy Growth Processes

Despite the extensive work on the strain-engineering of epitaxial thin films, there are a number of observations over the years that do not fit our fundamental understanding of thin-film strain. In $BaTiO_3$-based films, for instance, as early as the 1980s and 1990s researchers were reporting anomalously large lattice expansions in films [142,143,144,145], especially those grown by highly-energetic growth processes such as sputtering, pulsed-laser deposition, etc., that were not commensurate with the pervasive understanding of epitaxially constrained $BaTiO_3$. For instance, RF sputtered $BaTiO_3$ films were found to exhibit lattice parameters as much as 8.6%

larger than bulk versions (well beyond the expected 2.8% expansion of the *c* axis for a coherently strained $BaTiO_3$ film grown on $SrRuO_3/SrTiO_3$ (001) substrates) [145]. A number of potential explanations were posited for these observations and, as early as 1983, researchers were suggesting that the observed distortions could not be explained by classic epitaxial strain alone. Instead, researchers hypothesized that an anisotropic distribution of point defects (namely interstitial atoms and vacancies) could be responsible for the added distortion [143]. In turn, a potential connection between the growth process and the observed lattice expansion has been proposed [143,146,147], and some have evoked the concept of "negative pressure" induced effects (*i.e.*, large tetragonal strains and anomalous volume expansion under negative hydrostatic pressures) [148] to potentially explain the observations [146]. In turn, these anomalous lattice expansions are associated with interesting changes in the physical properties including enhancement of the ferroelectric transition temperature [143,147,149], and voltage-shifted ferroelectric hysteresis loops where the voltage shift scales linearly with thickness [144,149,150]. Despite this range of interesting work, no clear explanation for the effects has been developed, but it is generally considered that defects could play some role in the manifestation of these effects. While defects in ferroelectrics could potentially degrade the properties (*i.e.*, worsening leakage and promoting aging) [18] and can also impact the structure, phase transitions, polar ordering [151], various defect-engineering strategies have been developed to alleviate such effects and have been widely used to control lifetimes of ferroelectric capacitors in switching-applications as well as for tailoring the mobility of domain walls for piezoelectric applications [18,152,153,154]. Recent investigations have highlighted some unexpected benefits of specific defect-types, for instance, charged point defect complexes (so called defect-dipoles) have been utilized to achieve new functionalities including large reversible strains [155], multistate memory effects [156], and colossal dielectric responses [157]. However, to really control ferroelectric properties using defects, it is imperative to acquire an intimate knowledge of the nature of defects that occur in these materials [158]. With such an outlook, the aim of the work presented in this chapter is to understand the nature of the lattice-distorting defects that occur during high energy growth of $BaTiO_3$ thin films, and attempt to control their formation to achieve desired ferroelectric property enhancements.

5.3 Film Growth and Structural Characterization

130-170 nm $BaTiO_3$ / 40 nm $SrRuO_3$ thin-film heterostructures were grown on $DyScO_3$ (110), $GdScO_3$ (110), and $NdScO_3$ (110) single crystal substrates (corresponding to lattice

mismatches with the pseudocubic lattice parameter of $BaTiO_3$ of -1.7%, -0.99%, and 0.08%, respectively) via PLD as described in Chapter 2, with the laser fluence varied between 1.5 and 2.7 J/cm^2. We know from the PLD growth of $BaTiO_3$ films on bare $NdScO_3$ (110) substrates discussed in Chapter 2, that the growth process is highly sensitive to the laser fluence and care must be taken to control the stoichiometry and defect structures in the resulting films [159,160,161], XRD studies for the $BaTiO_3$ / $SrRuO_3$ / $GsScO_3$ (110) heterostructures (Fig. 5.1a) reveal that all films are epitaxial and single phase. Subsequent off-axis RSM studies about the 103- and 332-diffraction conditions for films and substrate, respectively, show that although the in-plane lattice parameters of the films are matched to that of the substrate, the out-of-plane lattice parameter increases as the laser fluence increases (Fig. 5.1b-f, expected peak locations for bulk (B) and coherently strained (S) $BaTiO_3$ are indicated for comparison). From both Poisson and electrostriction effects an increase in the *c*-axis lattice parameter by 1.7% as compared to bulk is expected, but in all films studied here an additional expansion of the out-of-plane lattice parameter of 0.6-4.1% is observed.

Subsequent study of film stoichiometry using X-ray photoelectron spectroscopy (XPS) (Fig. 5.2a) and RBS (Fig. 5.2b, c and d) reveals that all films possess nominally stoichiometric cation ratios within the limits of experimental error (+/-1%). This observation is consistent with prior studies of $BaTiO_3$ [161], but does not explain the observed increase of out-of-plane lattice parameter. Oxygen post-annealing of the films results in no change in the lattice parameters,

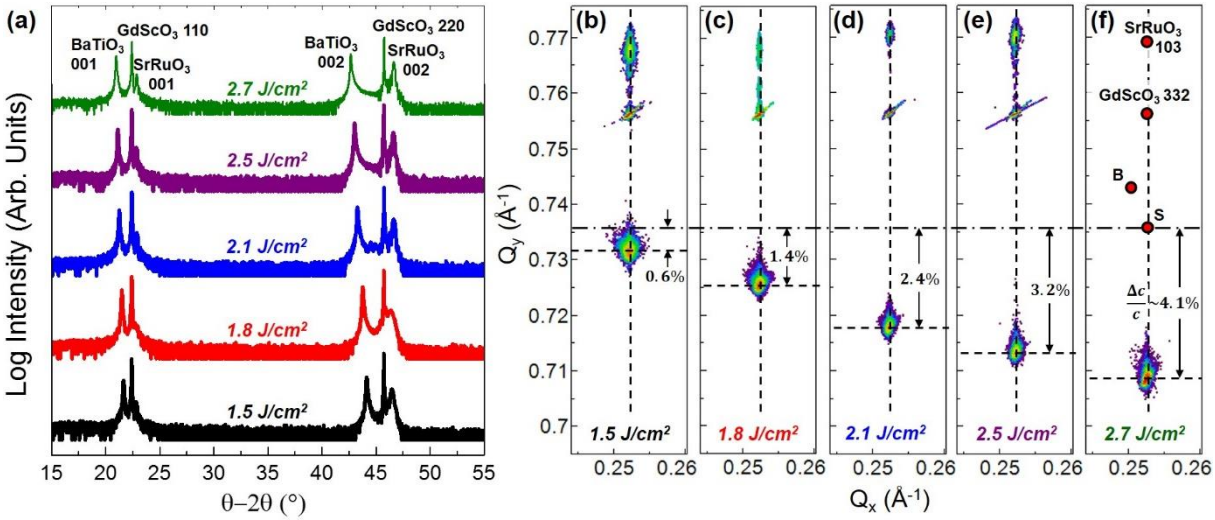

Fig. 5.1: (a) θ-2θ XRD studies of $BaTiO_3$ / $SrRuO_3$ / $GdScO_3$ (110) heterostructures where the $BaTiO_3$ film was grown at a laser fluence of (from bottom-to-top) 1.5, 1.8, 2.1, 2.5, and 2.7 J/cm^2. Corresponding off-axis reciprocal space mapping studies about the 103- and 332-diffraction conditions of the films and substrate for $BaTiO_3$ films grown at a laser fluence of (b) 1.5 J/cm^2, (c) 1.8 J/cm^2, (d) 2.1 J/cm^2, (e) 2.5 J/cm^2, and (f) 2.7 J/cm^2. Despite all films possessing the same in-plane lattice parameters, the out-of-plane lattice parameter is observed to increase with increasing laser fluence.

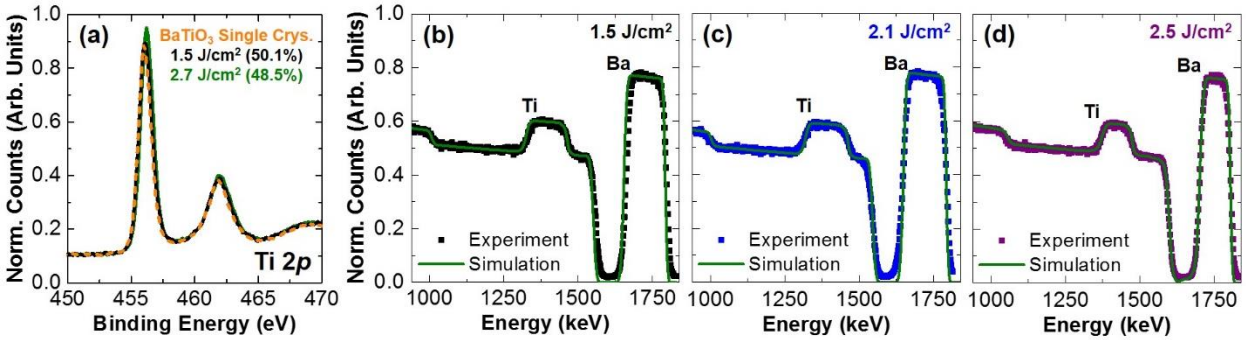

Fig. 5.2: (a) XPS study of the Ti 2*p* peak of $BaTiO_3$ single crystal for calibration and various $BaTiO_3$ films grown at a range of conditions that illustrates and rather small variation observed in the sample chemistry. Corresponding RBS studies of $BaTiO_3$ films grown at laser fluence of (b) 1.5 J/cm, (c) 2.1 J/cm^2, and (d) 2.5 J/cm^2 which correspond to films possessing the same stoichiometry (50.7% Ba) within the error of the measurement of +/- 1%).

eliminating chemical expansion from isolated oxygen vacancies as the mechanism for the lattice expansion. Taken together, these results suggest that the lattice expansion observed with increasing laser fluence arises not from cation or anion compositional deviations, but from defects associated with the varying energetics of the growth process [162,163]. Such effects have been observed previously in in the PLD growth $SrRuO_3$ [164], where expansions as large as 3.8% were observed. Despite reporting a direct connection between the expanded lattice constants and the energetic bombardment during deposition, the exact mechanism responsible for the lattice constant extension was not well understood. It was hypothesized that collision-induced displacement of cations into nonequilibrium lattice locations, implantation of the various ionic species during growth, resputtering of the film, and/or composition differences resulting from relative cation distributions in the laser plume, which are also pressure and fluence dependent, could be responsible. These observations highlight the incredible ability of complex oxides perovskites to accommodate and sustain large densities of point defects as both individuals and clusters, that in turn, are responsible for such dramatic changes in the lattice parameter of these materials from the ideal, bulk structure [165,166,167,168].

5.4 Impact of Defects on Ferroelectric Properties

To gain further insight into the nature of these growth-induced defects and their impact on ferroelectricity, detailed ferroelectric characterization was completed. Ferroelectric hysteresis loops were obtained from 0.001-10 kHz using symmetric $SrRuO_3$ capacitor structures [169], which

suppress extrinsic metal-ferroelectric interface related effects including imprint, asymmetric leakage, and lossy dielectric responses [170]. Accordingly, leakage characteristics (Fig. 5.3a) for films grown at 1.5, 1.8, and 2.7 J/cm^2 on $GdScO_3$ (110) substrates reveal symmetric, low-current response. Of particular interest is the fact that the leakage in films grown at high fluences (1.8 and 2.7 J/cm^2) is an order-of-magnitude lower than for the films grown at lower laser fluence (1.5 J/cm^2) suggesting that the growth-induced defects that give rise to increased cell volume do not also give rise to increased leakage. Characteristic ferroelectric hysteresis loops measured at 1 kHz (Fig. 5.3b) reveal two distinct behaviors: 1) horizontally centered, but pinched loops for films grown at 1.5 J/cm^2 (blue data, Figure 5.3b) and 2) horizontally-shifted, unpinched loops that exhibit shifts that scale with the laser fluence (1.8 and 2.7 J/cm^2, red and green data, respectively, Figure 5.3b). Both of these features are signatures of the presence of defect dipoles that are aligned out-of-the-plane of the films [171,172]. Additional insight is gained by exploring the frequency dependent evolution of the hysteresis loops, here shown for films grown at 1.5 and 1.8 J/cm^2 (Figure 5.3c and d, respectively). Films grown at low laser fluence (1.5 J/cm^2) exhibit loops that are horizontally centered across all frequencies studied, but exhibit pinching when probed at frequencies <5 kHz. Films grown at higher laser fluences show no loop pinching across the range of frequencies studied, but become increasingly off-centered as the measurement frequency is increased. These results are consistent with previous studies of $Pb_{0.98}Ba_{0.02}(Mg_{1/3}Nb_{2/3})O_3$-$PbTiO_3$ where thin films grown under high-

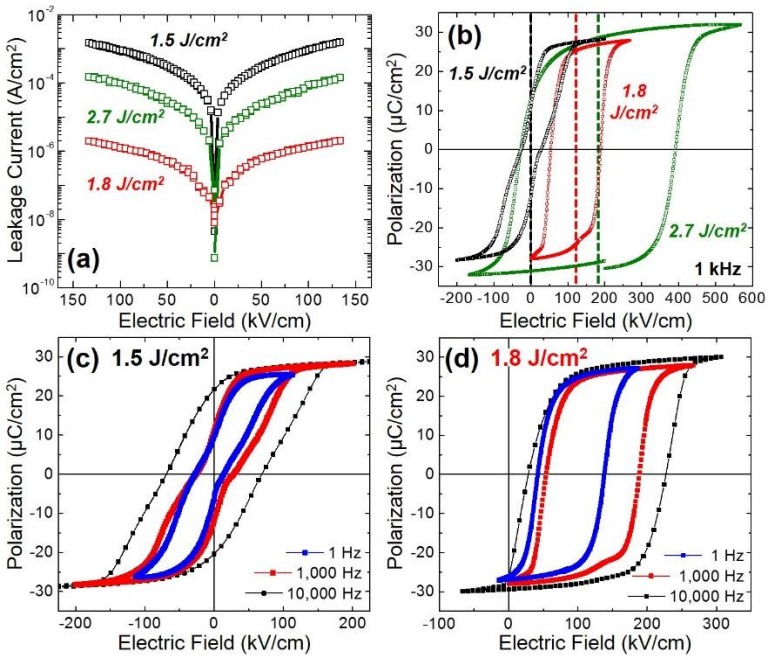

Fig. 5.3: (a) Leakage current as a function of applied electric field for $BaTiO_3/SrRuO_3/GdScO_3$ (110) heterostructures grown at laser fluences of 1.5, 1.8, and 2.7 J/cm^2. (b) Ferroelectric hysteresis loops for the same heterostructures measured at 1 kHz revealing increasing shifts along the voltage axis with increase laser fluence. Frequency-dependent polarization hysteresis loops for heterostructures with $BaTiO_3$ grown at (c) 1.5 J/cm^2 and (d) 1.8 J/cm^2. Films grown at lower fluences show horizontally centered, but pinched loops while those at grown at higher fluence reveal shifted, but unpinched loops.

bombardment conditions possessed large internal electric fields giving rise to only a single stable state of remenant polarization that could not be switched [173].

Such ferroelectric switching behavior (*i.e.*, the presence of pinched/shifted hysteresis loops) and the observed lattice expansion substantiate the presence of growth-induced defect dipoles that increase in concentration with laser fluence. A defect dipole is a generic term referring to any defect-complex that forms when two or more oppositely charged point defects in a lattice couple or interact in such a manner to produce a negative energy of association. In ferroelectrics, this typically refers to a complex of some acceptor defect and an oxygen vacancy or a donor defect and a cation vacancy [18,174]. While the exact nature of the acceptor (or donor) defect can vary, they are likely formed in the films in this study due to the energetic bombardment from the growth process, and are therefore predominantly from intrinsic point defects such as cation and anion vacancies (and potentially interstitials or anti-site defects). It should also be noted that the formation of such defect dipoles is also likely related to the observed reduction in leakage currents as they compensate for oxygen vacancies defects or serve as trap states for free carriers in the film. Before we move on to investigate into the possibility of aligned defect dipoles, we present dielectric permittivity and loss tangent measurements for all films across the frequency range from 1-100 kHz (Fig. 5.4a, b). It is seen that the films grown at higher laser fluences show highly diminished dielectric response as well as low dielectric loss tangents as compared to the film grown at a laser fluence of 1.5 J/cm^2.

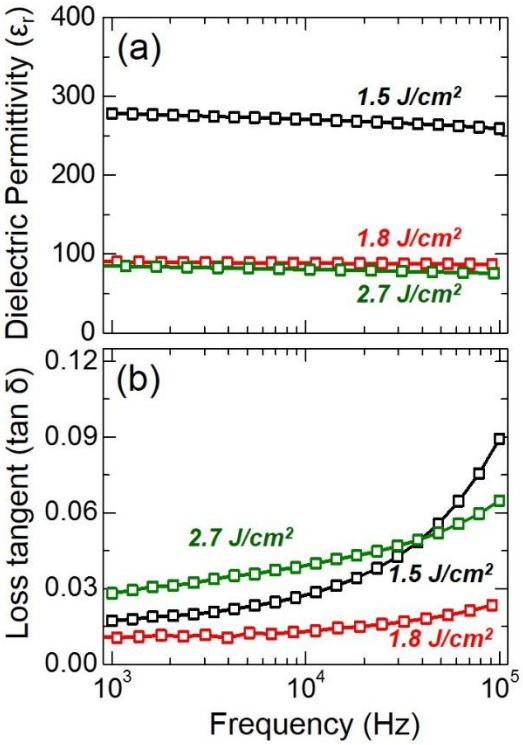

Fig. 5.4: Room-temperature (a) dielectric response and (b) loss tangent as a function of measurement frequency for $BaTiO_3$ heterostructures grown at laser fluences of 1.5, 1.8, and 2.7 J/cm^2.

5.5 Mechanism for Formation of Aligned Defect Dipoles

For ferroelectric materials with aligned defect dipoles, the expansion of the out-of-plane lattice parameter and the shift in the hysteresis loop are thought to be related to the elastic- and electric-dipole moments of the defect dipoles, respectively [174]. The effect of the latter is well characterized in the literature as the coupling between the electric-dipole moment and the

spontaneous polarization of the ferroelectric is known to break the degeneracy of the up/down polarization states (*i.e.*, giving rise to local built-in fields that pin the ferroelectric polarization and result in shifted and pinched loops). Shifted loops are expected when all of the defect dipoles are aligned and pinched loops when there is a mixture of up- and down-oriented defect dipoles. Likewise, the lattice distortion associated with the elastic-dipole depends on the orientation of the defect dipole and the net lattice deformation is proportional to the number of dipoles aligned in any direction [174,175]. It is known that external stresses can also break the degeneracy between symmetrically equivalent orientations of the elastic dipoles [175,176]. The $BaTiO_3$ films exhibit large expansion in the out-of-plane lattice parameter, while the in-plane lattice parameters remain constrained to that of the underlying $GdScO_3$ substrate, suggesting that the strain field from the (compressive) epitaxial strain can produce similar out-of-plane alignment of defect dipoles. The idea that stress (or strain) can drive the alignment of defect dipoles has been around for some time[174] and ultimately the electric and the elastic dipole energies can have different signs which can lead to complex alignment geometries. In our epitaxially-constrained thin films, however, we have a direct measure of the lattice deformation from both epitaxial strain and defects which enables us to estimate the elastic energy and compare it to the electric energy of a misaligned defect dipole in the background polarization.

5.5.1 Estimating Energies for Defect Dipole Alignment

From our direct measurements of defect-dipoled-induced lattice deformation and built-in internal fields, it is possible to estimate the realtive magnitude of the elastic and electric energies, respectively. To do this, let us first focus on the electric energy first. In general it is possible to consider that the defect dipole could align in one of six different geometries relative to the polarization: 1) aligned parallel to (one possible direction), 2) aligned anti-parallel to (one possible direction), or 3) aligned orthogonal to (four energetically degenerate directions) the polarization. Based on these possible alignment geometries, the maximum energy difference is between the parallel and antiparallel alignment. In general, it is assumed that the defect dipoles are set by the polarization and remain fixed in their alignment even under electric field switching of the polarization, which drives the formation of shifted ferroelectric hysteresis loops and stabilization of a single or preferred polarization direction (essentially driving back-switching as soon as the applied field is removed). Thus we can estimate the electric dipole moment interaction energy (which drives parallel alignment of the defect dipoles and the polarization) by using the

experimentally measured shift of the ferroelectric hysteresis loops (E_{shift}) as a measure of the energy difference between the parallel and antiparallel aligned geometries. Thus the energy gained by having the polarization and the defect dipoles aligned parallel (as opposed to antiparallel) is $W_{electric} = P * E_{shift}$ where P is the spontaneous polarization of the film. Based on the hysteresis loops measurements (Fig. 5.3b), we estimate this electric driving force to be ~7 J/cm^3 for $BaTiO_3$ films grown on $GdScO_3$ (110) substrates at a laser fluence of 1.8 J/cm^2.

At the same time, in the presence of external stresses (as in the case of epitaxial strained thin films), the interaction energy of the elastic dipoles with the strain fields must also be considered to determine the final orientation of these defects [174,177]. The elastic energy for an out-of-plane alignment of defect dipoles due to the bi-axial, in-plane strain field from the epitaxial constraints can be estimated from the misfit strain differences that would arise from an in-plane alignment of the defects and the associated in-plane lattice deformations. The films grown on $GdScO_3$ (110) substrates at a laser fluence of 1.5 J/cm^2 possess an excess out-of-plane lattice deformation of 0.6% from the out-of-plane alignment of the defect dipoles. Assuming an in-plane alignment of all of these defects, the in-plane lattice parameter of the film would be expanded thereby resulting in an increase in the compressive misfit strain for films on $GdScO_3$ (110) substrates from 1% to 1.3 % (calculated by assuming equal fractions of the defect dipoles aligned in the plane of the film that would give rise to a net increase in the in-plane lattice parameter by 0.3% along both directions). Subsequently, the elastic energy can be estimated by $\frac{u_m^2}{S_{11}+S_{12}}$ where u_m is the lattice misfit and S_{ij} are the elastic compliances. Thus the difference in elastic energy for out-of-plane as compared to an in-place alignment of the defect dipoles is found to be ~70 J/cm^3. This number grows as the laser fluence increases and the excess lattice deformation is increased. This suggests that the elastic-driving force for defect dipole alignment can be an order of magnitude larger than electric driving force in these films. This observation is consistent with prior work by Varnhorst *et al.*[178] which showed using electron paramagnetic resonance (EPR) spectroscopy-based studies that the alignment of paramagnetic Na^+-O^- dipoles in $BaTiO_3$ crystals could be achieved under the application of a uniaxial mechanical stress. For additional comparison, we can calculate the electrostrictive energy associated with the strain-stabilization of a ferroelectric material. This energy is responsible for much that we know takes place in thin-film ferroelectrics – including stabilizing out-of-plane polarization, tetragonal structures, and enhancing T_C in

compressively strained films. Estimates of this energy for $BaTiO_3$ give rise to an energy on the order of ~12 J/cm^3. What this shows is that among a number of active energies in the material, the presence of the elastic coupling between the defect dipoles and the strain fields in the material are among the most dramatic and thus are thought to play a significant role in the evolution of the effects observed herein.

5.5.2 Supporting Experiments for Alignment Mechanism

To further probe this idea, samples were grown at a laser fluence of 1.8 J/cm^2 on a range of different substrates including $DyScO_3$ (110), $GdScO_3$ (110), and $NdScO_3$ (110). Consistent with the films described above, all films are coherently strained to the various substrates and as one moves from films grown on $NdScO_3$ to $GdScO_3$ to $DyScO_3$ the out-of-plane lattice parameter of the $BaTiO_3$ increases as is expected based on the changing strain condition (Fig. 5.5). Subsequent hysteresis loop measurements (Fig. 5.6a and b, measured at 1 Hz and 10 kHz, respectively) reveal that films grown on substrates that provide a compressive strain (*i.e.*, $DyScO_3$ and $GdScO_3$) exhibit large horizontal shifts of the hysteresis loops indicating built-in fields arising from aligned defect dipoles while films grown on substrates that provide a small tensile strain (*i.e.*, $NdScO_3$) reveal negligible built-in fields suggesting that the defect dipoles are not preferentially aligned in the out-of-plane direction. Again, this data suggests that the epitaxial strain plays a crucial role in directing the out-of-plane alignment of the defect dipoles and the observation of built-in fields. As the elastic boundary conditions are changed from compressive to tensile in nature, we see clear trends (*i.e.*, increasing shifts of the hysteresis loop with increasing compressive strain) that suggest that epitaxial strain, not just polarization, are key to understand the alignment of the defect dipoles.

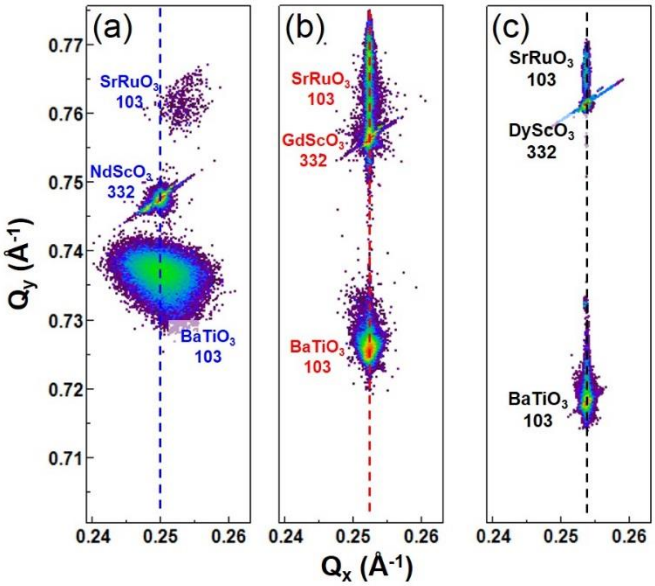

Fig. 5.5: Off-axis reciprocal space mapping studies about the 103 and 332 diffractions conditions for the films and substrate, respectively, for (a) $BaTiO_3$ / $SrRuO_3$ / $NdScO_3$ (110) and (b) $BaTiO_3$ / $SrRuO_3$ / $GdScO_3$ (110) heterostructures and about the 103 diffraction conditions for both film and substrate for a (c) $BaTiO_3$ / $SrRuO_3$ / $DyScO_3$ (110) heterostructure.

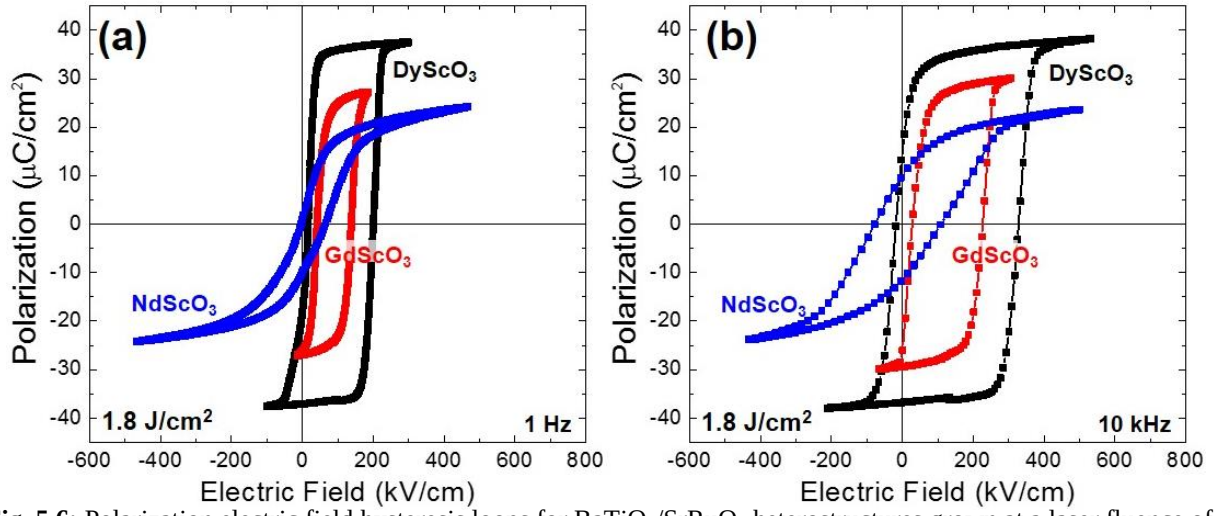

Fig. 5.6: Polarization electric field hysteresis loops for $BaTiO_3/SrRuO_3$ heterostructures grown at a laser fluence of 1.8 J/cm^2 on substrates producing a compressive ($SrTiO_3$ and $GdScO_3$) and tensile ($NdScO_3$) epitaxial strain as measured at (a) 1 Hz and (b) 10 kHz. A change in the sign of the strain results in a change in the nature of the loops with compressive strains driving shifted loops and tensile strains resulting in no shifts.

5.6 Impact on Ferroelectric Phase Transition Temperatures

So far we have demonstrated that compressive epitaxial strain can drive an out-of-plane alignment of growth-induced defect dipoles that manifest structurally as large expansions in the *c*-axis lattice parameter of the films. Such deformations signify the presence of large internal-stresses in the out-of-plane direction that arise from the elastic interactions between the aligned defect-structures and the host lattice. It has been shown that the presence of lattice strains can dramatically impact the magnitude and temperature-dependence of the polar state in $BaTiO_3$ [30,179]. In fact, researchers have shown that epitaxial strain alone can increase the T_C of $BaTiO_3/GdScO_3$ (110) heterostructures from 120°C to 400°C [60]. To explore the added effect of the out-of-plane lattice strains from the aligned defect dipoles on the T_C of $BaTiO_3$ films, we conducted temperature-dependent XRD studies of $BaTiO_3$ / $SrRuO_3$ / $GdScO_3$ (110) heterostructures grown at laser fluences of 1.5, 1.8, and 2.1 J/cm^2 (Fig. 5.7a). The temperature-dependent evolution of the out-of-plane lattice parameter reveals two regimes of thermal expansion over the temperature range from 25-900°C separated by a kink that is characteristic of a phase transition. RSM studies were completed at various temperatures throughout these studies and, in all cases, the films were found to remain coherently strained to the substrate [characteristic data for films grown at 1.8 J/cm^2 are provided for studies at 25°C (Fig. 5.7b) and 750°C (Fig. 5.7c)]. Subsequently, from the evolution of the out-of-plane lattice parameter, the presence of phase transitions at temperatures of ~500°C, ~650°C, and ~800°C for films grown at laser fluences of 1.5, 1.8, and 2.1 J/cm^2, respectively, are

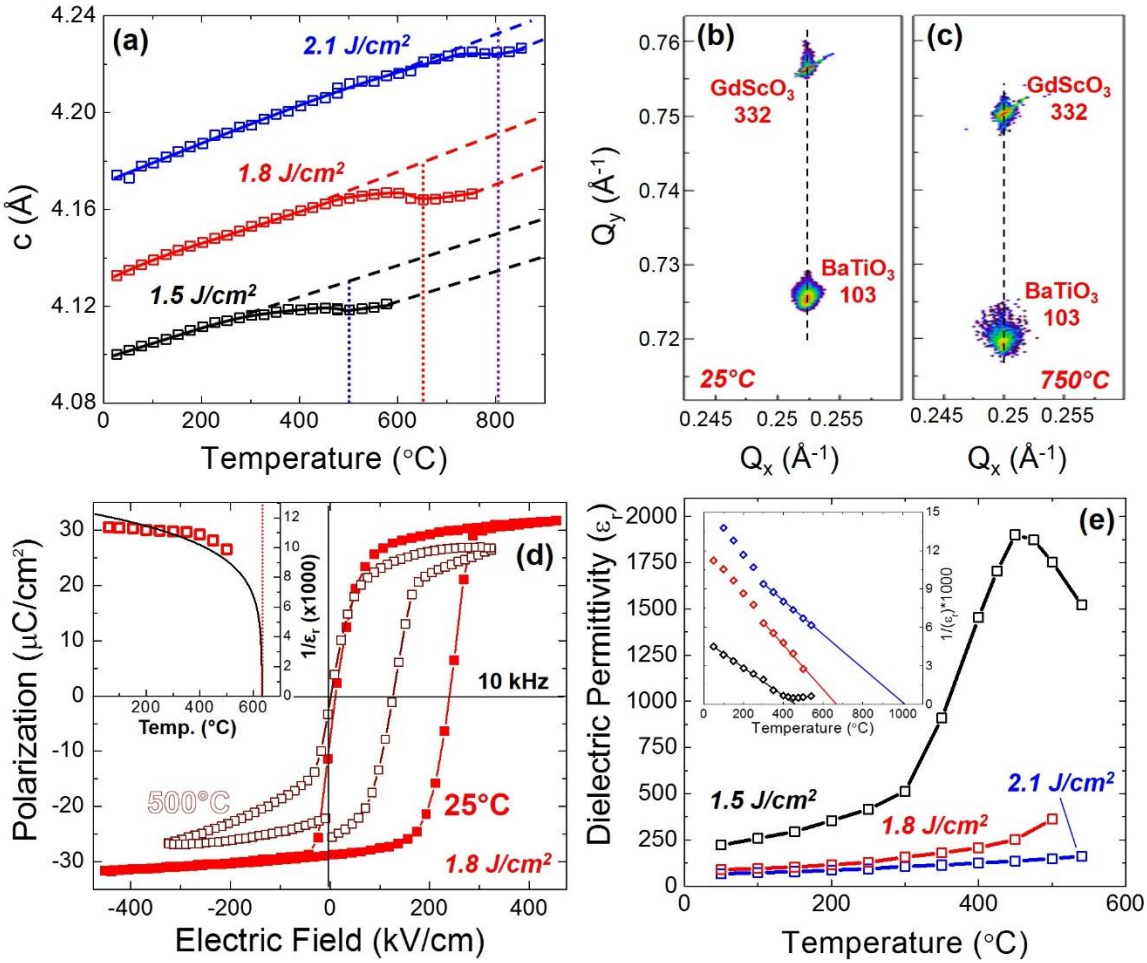

Fig. 5.7: (a) Temperature-dependence of out-of-plane *c*-axis lattice parameter evolution as measured from XRD for $BaTiO_3/SrRuO_3/GdScO_3$ (110) heterostructures where the $BaTiO_3$ was grown at laser fluences of 1.5 (black), 1.8 (red), and 2.1 (blue) J/cm^2. Two distinct regimes, separated by a kink in the lattice parameter are observed. Corresponding X-ray reciprocal space mapping studies of the heterostructure grown at 1.8 J/cm^2 at (b) 25°C and (c) 750°C revealing that the films remain coherently strained even at high temperatures. (d) Ferroelectric hysteresis loops, measured at 10 kHz, for the heterostructure grown at 1.8 J/cm^2 revealing the presence of strong polarization even at 500°C. The inset shows a summary of the evolution of the polarization from 25-500°C. (e) Dielectric permittivity of $BaTiO_3$ films grown at laser fluences of 1.5 (black), 1.8 (red), and 2.1 (blue) J/cm^2 measured as a function of temperature. The inset shows the inverse permittivity as a function of temperature a linear fit of the high-temperature response to extract an estimate for the transition temperature.

suggested. We also note that the excess lattice deformation (beyond that resulting from epitaxial strain) associated with the defect dipoles is observed to persist to even above the phase transition temperature which is further proof that the defect dipoles are coupled strongly to the epitaxial strain condition in the films.

To verify that the structural transitions observed in the XRD studies correspond to the transition from a ferroelectric-to-paraelectric state, we probed the temperature dependence of the dielectric and ferroelectric properties. To begin, we show data for the temperature-dependent

evolution of spontaneous polarization for a film grown at 1.8 J/cm^2 (Fig. 5.7d). Ferroelectric hysteresis loops were obtained up to 500°C and reveal a spontaneous polarization value of 27 μC/cm^2 (~80% of the room-temperature value) despite being 100°C above the T_C for a defect-free, coherently strained film [60]. This suggests that the stabilization of the ferroelectric state of $BaTiO_3$ from aligned defect dipoles can dramatically impact the properties. The temperature dependence of the ferroelectric polarization (inset, Fig. 5.7d) are provided to summarize the response from 25-500°C. To further explore the mechanism for the enhancement of T_C, we employed Ginzburg-Landau-Devonshire (GLD) models [180] to predict the temperature evolution of the spontaneous polarization considering both the out-of-plane elastic strain arising from aligned defect-dipoles and the in-plane biaxial epitaxial strain from the substrate (Fig. 5.8, details in Appendix B). The predicted temperature dependence of the spontaneous polarization for the film grown at 1.8 J/cm^2 matches closely with the experimentally measured values (inset, Figure 5.7d) and suggests a phase transition at $T_C \approx 650$°C that coincides with the phase transition observed in the temperature-dependent XRD. Likewise, the predicted T_C for films grown at 1.5 and 2.1 J/cm^2 are ≈515°C and ≈810°C, respectively; in excellent agreement with the temperature-dependent XRD (Fig. 5.7a) and strongly suggesting that the anomalies in the XRD studies correspond to ferroelectric-to-paraelectric transitions. These observations also lead us to conclude that these enhancements in the T_C can be attributed to the epitaxial strain-induced alignment of growth-induced defect dipoles that in turn produce anisotropic lattice deformations and enhanced strain states.

Further insight into the ferroelectric nature of these transitions is obtained from temperature dependent dielectric measurements (Fig. 5.7e) for the films grown at 1.5, 1.8, and 2.7 J/cm^2. Fits of the inverse dielectric response as a function of temperature (inset, Fig. 5.7e) for these films suggests $T_C \approx$ 475°C, 650°C, and 1000°C for films grown at 1.5, 1.8, and 2.7 J/cm^2, respectively. These

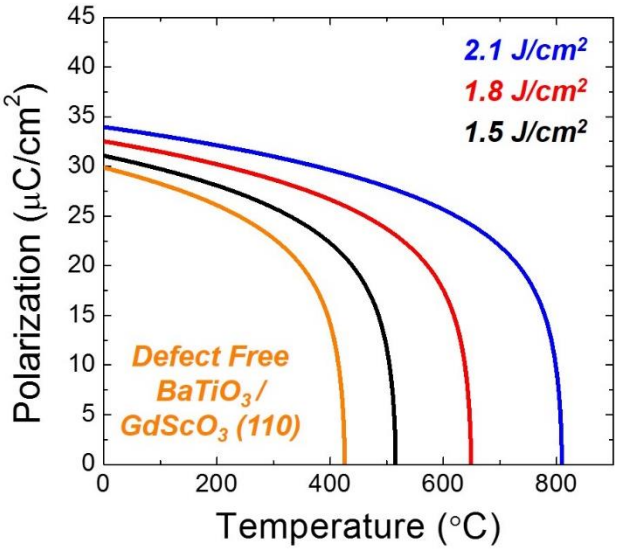

Fig. 5.8: Predicted temperature-evolution of polarization in coherently strained $BaTiO_3/GdScO_3$ (110) heterostructures possessing various levels of additional out-of-plane strain as measured by X-ray diffraction. The transition temperature scales with increasing out-of-plane lattice distortion which corresponds to increasing laser fluence.

values are in excellent agreement with the predictions from the GLD models which can be used to predict the T_C for a given combination of epitaxial and defect dipole strain. Moreover, in the case of the films grown at a fluence of 1.5 J/cm^2, we observe a sharp dielectric anomaly through the structural transition ~475°C (black data, Figure 5.7e) confirming the presence of a ferroelectric-to-paraelectric phase transition at this temperature.

5.7 Conclusions

In this chapter, we have explored the coupling between epitaxial strain and defect dipoles that form due to the PLD growth process to controllably tune the T_C of $BaTiO_3$ to over 800°C. Purely epitaxial strain-based approaches for T_C enhancement are limited by the magnitude of strain that can be applied, the thicknesses that can be achieved before film relaxation, and a lack of strain tunability. In this work we show that epitaxial strain can be used to control the ordering of defect dipoles inducing additional out-of-plane strains and enabling controlled enhancement of T_C without the need to change substrates. This is especially exciting since neither the polarization or leakage properties are diminished thereby enabling the measurement of well-defined ferroelectric hysteresis loops to at least 500°C. It should be noted that even in bulk crystals, aging (a time dependent alignment of defect complexes in the direction of polarization) can give rise to enhanced T_C, but the exact mechanism was not well understood nor is it known how to deterministically control the magnitude and nature of these effects [181]. Additionally, in bulk materials the enhancement of T_C has also been observed to be fleeting or time-dependent, but our enhanced properties have been observed to be stable for > 6 months likely due to the added stabilizing power of the epitaxial constraints. Such a combined control of epitaxial strain and growth-induced defect-structures to control ferroelectricity in materials opens up a new paradigm in strain control of properties. We note, however, that this is not the first time that the growth process has been used to manipulate the density of defects in a material. In fact, in group IV semiconductors (*e.g.*, Si_xGe_{1-x}) it has been shown that ion-assisted deposition methods can produce defect complexes that can be used to modify the strain state of materials [182]. Early work in this capacity even lead some researchers to suggest that "strain 'engineering' by controlled ion beam defect injection may have interesting implications for lattice-mismatched heteroepitaxy" and may lead to the "accommodation of film-substrate lattice mismatch in a novel manner" [182]. This work provides a new application of this concept to complex oxide ferroelectrics and represents an exciting discovery with implications for utilization of these materials in high-temperature applications.

CHAPTER 6

ENGINEERING DIELECTRIC RESPONSES *VIA* CONTROLLED CHEMICAL- AND STRAIN-GRADIENTS IN FERROELECTRIC THIN FILMS

In the chapters so far, we explored new strain-based routes to engineer novel and enhanced functionalities in ferroelectric thin films of uniform composition. In this chapter, we introduce the possibility of using spatial gradients in composition and strain to engineer optimized dielectric responses with superior thermal stability. We present preliminary measurements for the temperature dependence of dielectric permittivity for monodomain BST-films with highly controlled composition- and strain- gradients. Our studies reveal that high values of dielectric permittivity (ε_r ~750) that is stable over a wide temperature range (25-350°C) are attainable for coherently-strained and compositionally-graded epitaxial BST films.

6.1 Introduction

Rapid growth and advancements in the area of wireless communication in recent years has led to an ever increasing demand for broad bandwidth, reliable and low cost RF tunable microwave devices that deliver superior performance needed to support emerging applications [183]. While traditional materials including ferrites and semiconductors have been considered for these devices, they suffer several drawbacks including slow tuning speeds in the case of ferrites and high losses at microwave frequencies in the case of semiconductor-based devices [183,184]. BST-based solid solution, on the other hand, show large dielectric responses and low dielectric losses at microwave frequencies. The dielectric response in BST thin films can be easily tuned by the application of external biases of only a few volts, and are therefore candidate materials for electronically-tunable microwave devices such as filters, oscillators, phase-shifters and resonators [185,186,187,188].

However, in addition to the aforementioned properties of high dielectric permittivity, low dielectric losses and large tunability, it is also imperative that these properties are temperature-insensitive to ensure device performance that is consistent and reliable under harsh operating conditions. While the dielectric permittivity and tunability of a single-composition BST films are maximal at the Curie temperature, they are strongly influenced by temperature changes in the vicinity of the Curie point. To overcome this limitation and to achieve temperature-insensitive dielectric responses, researchers since the mid-1990s have explored the use of compositionally-graded ferroelectrics in which the ferroelectric to paraelectric phase transition is substantially diffused (broadening of phase transition is tunable by tuning the composition gradient) [189,190,191].

Over the last decade, researchers have also demonstrated that strain-gradients in ferroelectric thin films can also result in a similar broadening of ferroelectric to paraelectric phase transition and thereby enhance the thermal stability of ferroelectric susceptibilities [192,193]. Based on such insights, the aim of the work presented in this chapter is to synthesize high quality monodomain versions of compositionally-graded BST films that simultaneously possess composition- and strain- gradients, and attempt to achieve desired temperature-stable dielectric property enhancements. We also compare the experimentally measured temperature dependence of dielectric permittivity to those predicted by advanced GLD-based models that incorporate energy terms related to composition-, strain- and polarization- gradients that exist in such compositionally graded ferroelectric thin films. Based on these studies, we also comment on the

relative importance, and necessity, of each of these contributions in describing the response of graded ferroelectric thin films.

6.2 Background on the Physics of Graded Ferroelectrics

Graded ferroelectrics refers to materials that possess a gradient in ferroelectric polarization across the thickness of the ferroelectric sample [194]. There are several routes to engineer polarization gradients in ferroelectrics, including: (1) The imposition of a gradient in temperature across the sample [195,196], (2) Controllably changing composition during growth to engineer composition- and polarization- gradients in a direction that is normal to the growth front [197,198], and (3) Designing structures with engineered stress/strain gradients across the sample thickness [199,200,201,202,203]. Of these approaches, gradients in composition and strain are easily realizable and have emerged as promising routes to design graded ferroelectrics for real world device applications. It has been demonstrated that the presence of such gradients break the macroscopic inversion symmetry across the ferroelectric device giving rise to novel properties such as self-poling, built-in fields, asymmetric/shifted hysteresis loops, as well as electric-field, thermal, and stress susceptibilities that are distinctly different from their ungraded counterparts [194,195,204]. Such effects have been explored theoretically *via* first-principles calculations [205,206], as well as phenomenological Landau theory [193,207,208,209] to understand the mechanisms underlying the origin of such distinct properties. It has been shown that the observed self-poling and asymmetric hysteresis loops for graded-ferroelectrics can be modelled by modifying phenomenological GLD-based models for homogeneous ferroelectrics with the inclusion of the following additional symmetry-breaking energy terms to the Landau free energy functional,

$$G_\gamma = \gamma P \frac{\partial c}{\partial z}; G_f = f_{ij} P \frac{\partial \varepsilon_{ij}}{\partial z} \qquad (6.1)$$

where P is the ferroelectric polarization, $\frac{\partial c}{\partial z}$ and $\frac{\partial \varepsilon_{ij}}{\partial x_j}$ are the composition- and strain- gradients respectively, G_γ is the energy term for the coupling between polarization and composition-gradients, G_f is the energy term for the coupling between polarization and strain-gradients, γ is the phenomenological coefficient for composition-gradients and f_{ij} is the phenomenological coefficient related to strain-gradients, more commonly termed as the flexoelectric coefficient [209,210]. The strain-gradient related effects in particular, also known as flexoelectricity, is a

property of all insulators whereby they develop a spontaneous polarization under conditions of inhomogeneous deformation [211]. Till recent times, the role of such flexoelectricity-related electromechanical contributions to properties of bulk ferroelectrics have been mostly neglected due to the relative weakness of the effect compared to its piezoelectric and electrostrictive counterparts. In nanoscale materials, however, the strain gradients achievable are several orders of magnitude higher than what is possible in bulk and can dramatically impact their dielectric, ferroelectric and electromechanical properties.

Recent GLD-based phenomenological studies for epitaxial monodomain graded-BST films have shown that in addition to the effects discussed above, depolarization fields that oppose the spatial variation in polarization across the thickness of graded ferroelectric thin films, can dramatically impact the magnitude as well as temperature-dependence of ferroelectric susceptibilities [193]. Under short circuit boundary conditions, such depolarization effects in graded-ferroelectric films result in the addition of a depolarization energy term (G_D) to the Landau free energy functional,

$$G_D = -\frac{1}{2}E_D P,\ E_D = \frac{1}{\varepsilon_0 \varepsilon_b}\left[P - \frac{1}{h}\int_0^h P.dz\right] \qquad (6.2)$$

where E_D is the depolarization field, h is film thickness, ε_b is the background permittivity that incorporates the effect of intrinsic dielectric screening as well as extrinsic contributions from defects and free charge carriers that can screen or compensate depolarization fields in real systems.

In all, we have discussed aspects of graded-ferroelectrics that can dramatically impact ferroelectric susceptibilities and their temperature-stability. Systematic experimental studies are desired to investigate the relative strengths of each of the individual effects. In the sections that follow, we describe preliminary studies on a systematic set of high quality epitaxial BST films to probe the impact of each of these effects.

6.3 Growth of Graded BST Thin Films

In this section, we focus our attention on the growth of graded films of $Ba_xSr_{1-x}TiO_3$ with compositions between x = 0.6 to 1.0. The two end-members are: 1) $Ba_{0.6}Sr_{0.4}TiO_3$ (henceforth referred to as BST 60:40), which in bulk exists as a cubic paraelectric (T_C ~ 0°C) with a unit-cell lattice parameter of a = 3:965 Å at room temperature, and 2) $BaTiO_3$, which in bulk exists as a tetragonal ferroelectric (T_C ~ 120°C) at room temperature with unit-cell lattice parameters a =

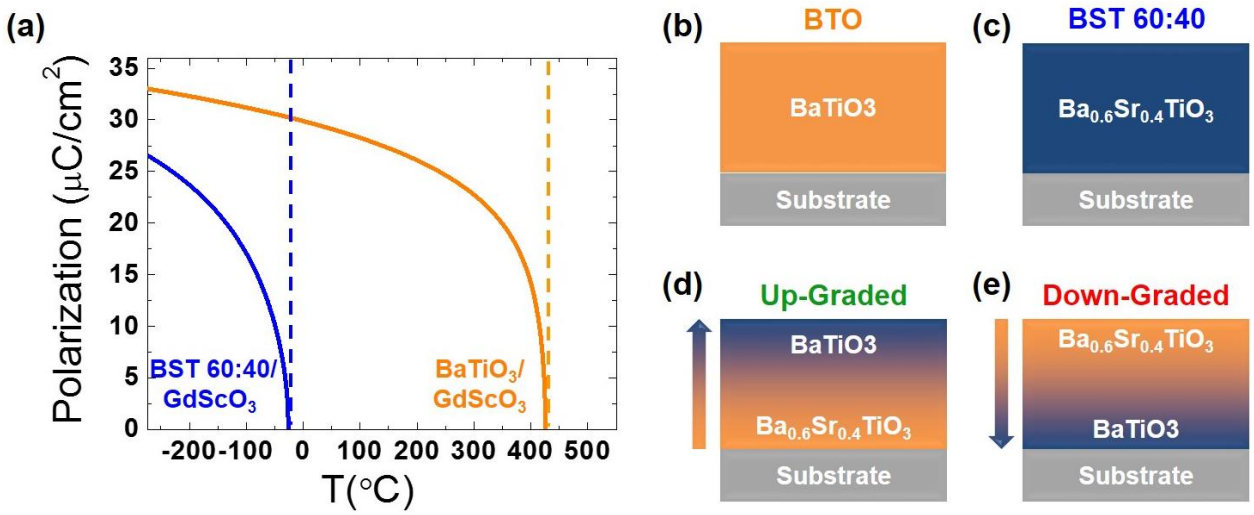

Fig. 6.1: (a) Predicted temperature-evolution of polarization in coherently strained BST 60:40/$GdScO_3$ (110) and $BaTiO_3$/$GdScO_3$ (110) heterostructures. Schematic illustrations of the four sample variants studied in this work including (b) single-layer $BaTiO_3$, (c) single-layer BST 60:40, (d) up-graded heterostructures (which smoothly transition from BST 60:40 to $BaTiO_3$ from the substrate to the film surface), and (e) down-graded heterostructures (which smoothly transition from $BaTiO_3$ to BST 60:40 from the substrate to the film surface).

3.992 Å and c = 4.036 Å (pseudocubic lattice parameter, a_{pc} = 4.006 Å) [9,11,212,213]. As discussed in chapter 5, a compressive in-plane strain of 1% that occurs in coherently-strained $BaTiO_3$ films (free of lattice-expanding defects) grown on $GdScO_3$ (110) substrates (pseudocubic lattice parameter, a_{pc} = 3.967 Å) results in an out-of-plane tensile strain of 1.7% (with contributions from both Poisson and electrostriction effects) and is also accompanied by enhancements of ferroelectric T_C to nearly 400°C. On the other hand, BST 60:40 possesses negligible lattice match (+0.05%) with $GdScO_3$ (110) substrates. Correspondingly the T_C for BST 60:40 films grown on $GdScO_3$ (110) substrates are virtually unchanged. This is also seen in the temperature-dependent evolution of polarization predicted using GLD-based thin film models (Fig. 6.1a) for the two end-members. While dielectric responses for strained-films of each of these end-members peak at their respective T_C's, they demonstrate strong temperature-dependencies near the Curie point that is often undesirable for applications.

In order to design for temperature-stable performance, in this work we focus on films where we gradually change the composition between the two end-member compositions across the film thickness. Since the phase transition characteristics of BST films are monotonic function of the Ba/Sr ratio, grading the composition across the thickness have been shown to result in diffuse ferroelectric-to-paraelectric phase transition that extends between the T_C's of the two end-member compositions, and thereby achieve enhanced temperature-independent responses [214]. This also

suggests that such compositional gradients when used in conjunction with epitaxial strain, can result in an even broader temperature regime for temperature-insensitive dielectric responses as the T_C's of the end member compositions in the strained state are further apart. In order to investigate such effects, we employed PLD to synthesize four different kinds of BST-based thin film heterostructures on $SrRuO_3$- buffered $GdScO_3$ (110) substrates: 1) single-layer $BaTiO_3$ (Fig. 6.1b), 2) single-layer BST 60:40 (Fig. 6.1c), 3) compositionally up-graded heterostructures (which smoothly transition from BST 60:40 to $BaTiO_3$ from the substrate to the film surface) (Fig. 6.1d), and 4) compositionally down-graded heterostructures (which smoothly transition from $BaTiO_3$ to BST 60:40 from the substrate to the film surface) (Fig. 6.1e). We included end-member films of uniform composition in the study to enable a systematic analysis of the ferroelectric properties of graded-BST films in comparison with uniform composition films synthesized *via* PLD using the same growth conditions. In all cases, the BST films synthesized were 150 nm thick, and were grown using the optimized growth parameters for $BaTiO_3$ films as discussed in chapter 2. Compositionally graded heterostructures were synthesized by using a programmable target rotator (Neocera, LLC) that was synced with the excimer laser to controllably vary the number of laser pulses on pure $BaTiO_3$ and BST 60:40 targets to achieve the desired composition gradient.

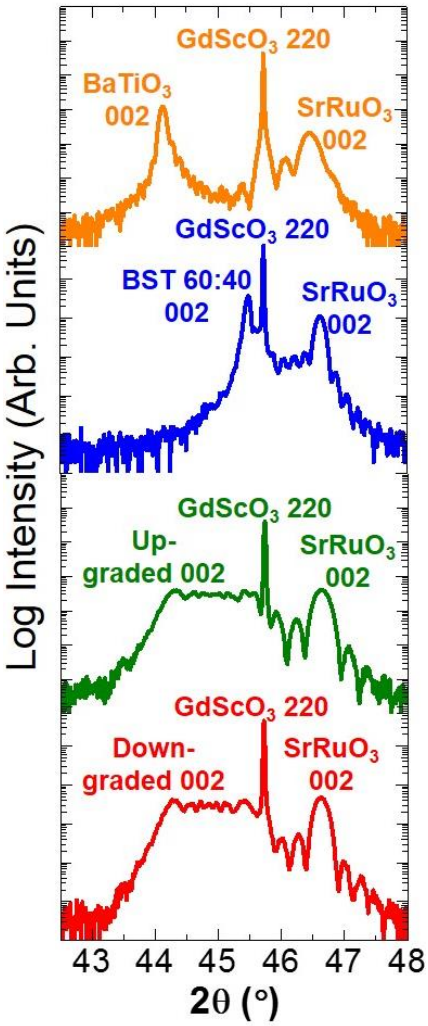

Fig. 6.2: (a) XRD about the 002-diffraction condition for (top to bottom) $BaTiO_3$, BST 60:40, upgraded and downgraded films respectively grown on $SrRuO_3$-buffered $GdScO_3$ (110) single crystal substrates

6.4 Crystal and Ferroelectric Domain Structure of Graded BST Thin Films

XRD studies for the various BST / $SrRuO_3$ / $GdScO_3$ (110) heterostructures reveal that all films are epitaxial and single phase. Fig. 6.2 shows a zoom-in of the high resolution X-ray θ-2θ line scans around the 002-diffraction condition for the various films. The uniform composition $BaTiO_3$ and BST 60:40 films show sharp well-defined peaks along with the presence of Laue oscillations that are typical of films with high crystalline quality, and possess smooth surface and interfacial topography. On the other hand, X-ray θ-2θ scans for the

upgraded and downgraded films reveal a top-hat peak structure that stretches across the peak positions of the two end-member compostions. Subsequent off-axis X-Ray RSM studies about the 103- diffraction conditions for the up-graded and down-graded films (Fig. 6.3a and b, respectively) reveal that the films are coherently strained to the $GdScO_3$ substrate (same Q_x value for off-axis film and substrate peaks). In the Q_y direction, the film peak for the graded films stretch across locations corresponding to the strained end-member compositions, indicative of a smooth gradiation in lattice parameters due to the compostion gradient across film thickness. Furthermore, the uniformity of peak width in the Q_x-direction verifies the linear grading of composition across thickness for both the up-graded and down-graded films.

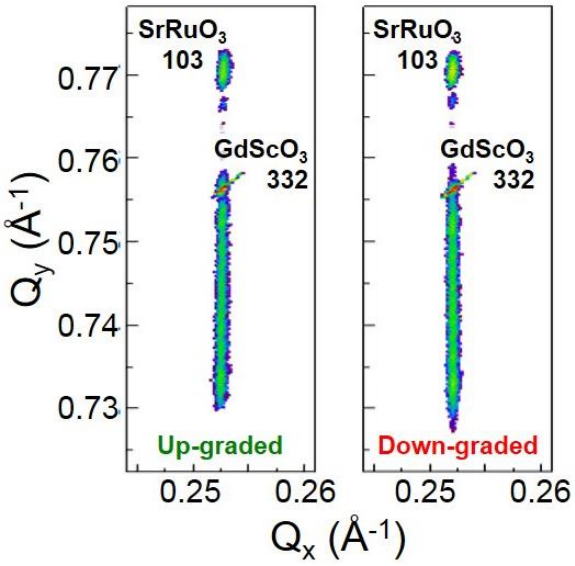

Fig. 6.3: Off-axis RSMs about the pseudocubic 103-diffraction condition for the graded films showing that the films are coherently strained to

The ferroelectric domain structure for all films synthesized was studied using PFM. For brevity, we present PFM scans for up-graded film heterostructures (Fig. 6.4). All films synthesized are found to be monodomain revealing uniform contrast in the vertical- and lateral- PFM images. We found no evidence for the presence of either 180° domains or 90° domain walls that could potentially exist in tetragonal ferroelectrics. Based on the XRD and PFM studies we conclude that all films studied are coherently strained and monodomain, and therefore serve as simple model systems to investigate the effects of composition- and strain- gradients on ferroelectric susceptibility.

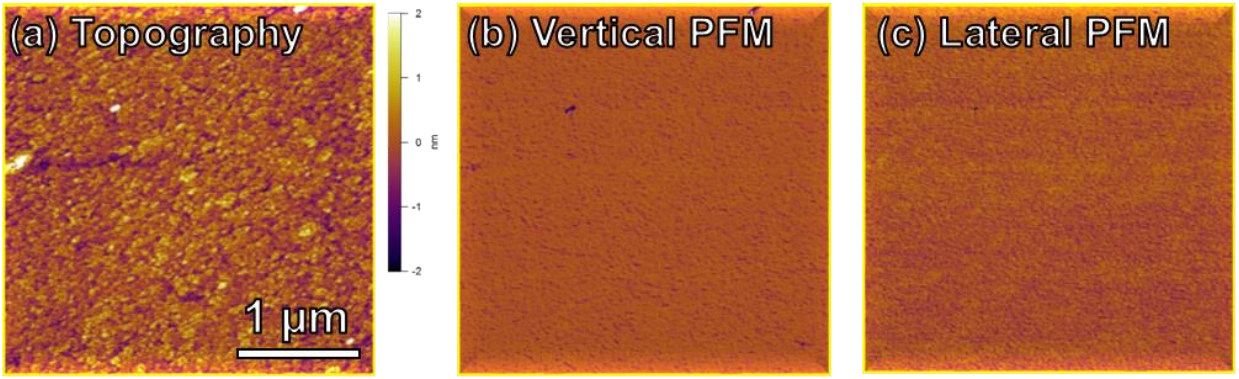

Fig. 6.4: (a) Topography, (b) Vertical PFM and (c) Lateral PFM images for up-graded BST films. Lack of any contrast in the PFM images suggests monodomain films.

6.5 Gradient Effects on Ferroelectric Properties

In this section, we compare the ferroelectric properties of the four thin-film heterostructure variants synthesized using symmetric capacitor devices (circular capacitors, diameter 25-100 µm) with epitaxial top $SrRuO_3$ electrodes fabricated using an MgO-based hard-mask process [169]. The use symmetric $SrRuO_3$ capacitor structures suppresses extrinsic mechanisms for the hysteresis loop shifts including metal-ferroelectric interface related effects such as imprint, asymmetric leakage and lossy dielectric responses [170]. We begin by looking at the P-E hysteresis loops for the end-member films of uniform composition (Fig. 6.5a). The uniform-composition $BaTiO_3$ heterostructure capacitors show symmetric and square hysteresis loops that are horizontally centered, without evidence of any asymmetry. P-E loops for BST 60:40 heterostructure devices are also horizontally centered. They display non-hysteretic characteristic typical of a non-linear dielectric, and is in tune with BST 60:40 being a room temperature paraelectric (T_C ~ 0°C) under small tensile strain. Next, we move on to P-E hysteresis loops measured on the graded films (Fig. 6.5b). Focusing first on the upgraded films, we notice asymmetric loops that are shifted to the right by ~32 kV/cm. By inverting the composition gradient across the film thickness, as in the case of the down-graded films, the loops are found to be shifted by nearly an equal amount (28 kV/cm) to the left, confirming that the shifts are intrinsic and related to the composition- and strain- gradients in the graded films.

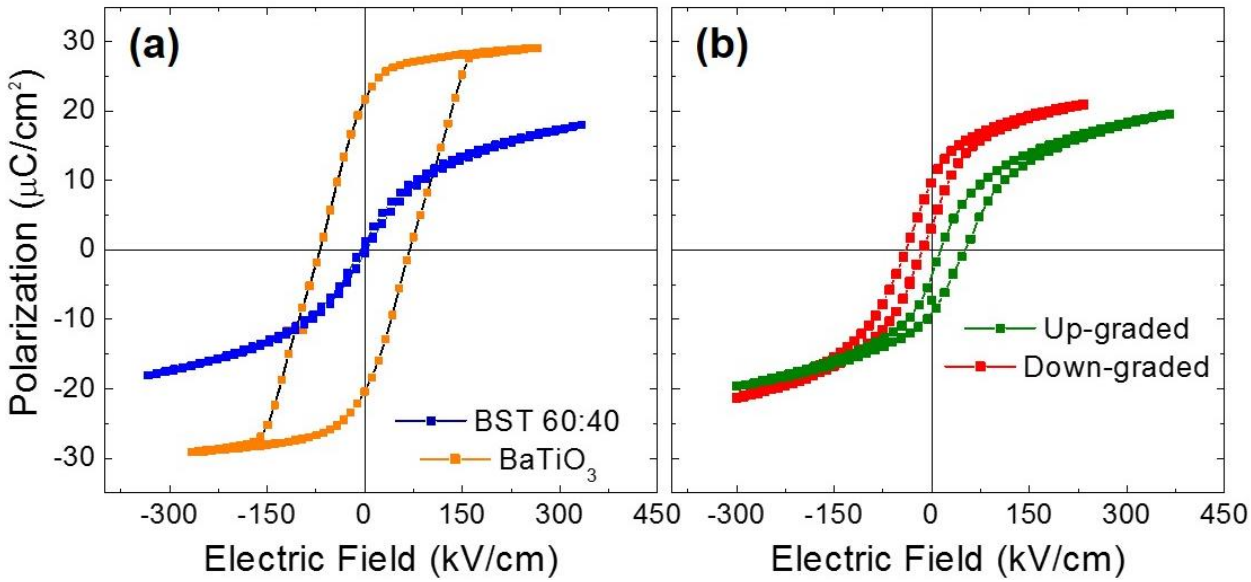

Fig. 6.5: Polarization-electric field hysteresis loops measured at 10 kHz for (a) Uniform-composition BaTiO3 (orange) and BST 60:40 (blue) heterostructure devices showing horizontally centered loops, and (b) Graded heterostructure devices showing asymmetric hysteresis loops with positive and negative offsets of ~30 kV/cm for up-graded and down-graded films respectively.

Since composition gradients, as well as in-plane and out-of-plane strain gradients simultaneously exist in the graded-film heterostructures, it is not possible to separate out contribution from each of these symmetry-breaking effects to the total shift observed in P-E hysteresis loops. However, previous studies have established the equivalence between Sr-alloying and applied mechanical stress/strain towards ferroelectric property evolution in $BaTiO_3$ [28,215]. Based on such arguments, we propose that the effects of the compostition- and strain- gradients that exist in the graded-BST films can be combined into an effective strain gradient. RSM studies for graded films (Fig. 6.3) had revealed that the combination of compressive epitaxial strain and a controlled composition-gradient across the thickness in BST thin films helps to engineer a state where the in-plane dimensions of the BST unit-cell are held constant by the substrate while the out-of-plane dimension varies linearly across the film thickness, indicating an effective strain gradient that is purely longitudinal. Based on the hysteresis loop shift of ~30kV/cm and the fact that the strain changes by 2.6 % across the film thickness of 150 nm, we calculate an effective longitudinal flexoelectric coefficient (f_{eff}) of ~10^{-10} m^3/C for the graded BST films.

6.6 Gradient Effects on Thermal Stability of Dielectric Responses

In this section, we focus on the thermal stability of dielectric responses for graded BST thin films. To begin with, we look at the temperature dependence of dielectric permittivity for uniform-composition $BaTiO_3$ and up-graded BST films ((Fig. 6.6a, orange and green data respectively) measured at a frequency of 10kHz. It is easily seen that the strained single-composition $BaTiO_3$ heterostructure devices demonstrate strongly temperature-dependant dielectric responses in the viscinity of the ferroelectric T_C. While the dielectric permittivity is relatively stable at lower temperatures away from the T_C, its magnitude is highly diminished. On the other hand, the temperature dependence of dielectric responses for up-graded BST heterostructure devices demonstrate high values for dielectric permittivity (ε_r ~ 750) that varies by less than 10% over the entire range measured from 25-350°C. From the measured value of effective flexoelectric coefficient of 10^{-10} m^3/C in the previous section, we have also calculated the temperature dependance of the dielectric permittivity for the up-graded films (Fig. 6.6b) using advanced monodomain GLD-models for graded ferroelectrics (see ref. 193 for details) for different values of background dielectric permittivity. The concept of background permittivity represents the energy cost due to depolarization fields that arise from polarization gradients and is often used

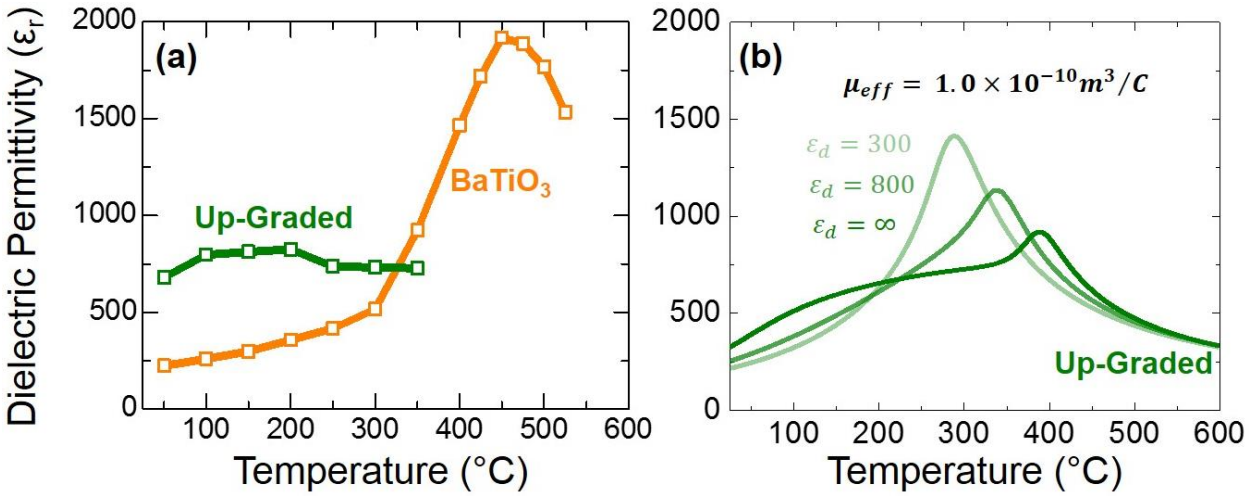

Fig. 6.6: (a) Temperature-dependence of dielectric permittivity for up-graded (data in green) and single composition BaTiO3 (data in orange) thin film heterostructures, and (b) Predicted temperature dependence of dielectric permittivity for up-graded films using advanced GLD models.

as a fitting parameter to match experimental results. Even higher temperature dielectric measurements are yet to be done for a clear comparison of the measured temperature-dependence of dielectric permittivity for up-graded films with features predicted using the GLD model. Nevertheless, based on our measurements so far, dielectric response of the up-graded BST film suggests zero depolarization energy costs for polarization gradients in the graded-BST heterostructure devices ($G_D = 0$ for $\varepsilon_b = \infty$, using eq. 6.2). This potentially suggests that the polarization gradients in the graded films are sufficiently weak to be completely screened by extrinisc factors including free charges and defects that are present in real films. We note that these are preliminary findings and additional measurements are underway to understand the trends observed in the dielectric studies.

6.7 Conclusions

In this chapter, we have used epitaxial strain in conjunction with controlled composition- and strain- gradients to tune the thermal stability of dielectric responses of BST-based ferroelectric thin films. For this, we have synthesised a systematic set of single-composition and compostionally-graded BST samples that are monodomain and coherently-strained that serve as model systems to effectively probe the role of such spatial gradients in composition and strain towards engineering novel responses in ferroelectric thin films. Ferroelectric measurements on epitaxial monodomain graded-BST films that are coherently strained to $GdScO_3$ (110) substrates have revealed an effective longitudinal flexoelectric coefficient of 10^{-10} m^3/C as well as enhanced values of dielectric permittivity (ε_r ~750) that varies by less than 10% over a wide temperature

range (25-350°C). Preliminary comparisons with advanced GLD-based models for graded ferroelectric films suggest negligible impact of depolarization effects on polarization gradients in the graded-BST films suggesting the presence of extrinsic mechanisms for the screening of depolarization fields in these materials. Additional high temperature and high frequency dielectric and tunability measurements for the graded-BST films are underway, and will shed more light on the physics and functionality of graded ferroelectrics in general.

CHAPTER 7

SUMMARY OF FINDINGS AND SUGGESTIONS FOR FUTURE INVESTIGATIONS

7.1 Summary of Findings

7.1.1 Summary of Chapter 1

Chapter 1 begins with a review of the basic concepts of ferroelectricity with a brief overview of the technological significance of these materials. This is followed by a discussion of prototypical perovskite ferroelectric systems along with conventional materials design strategies including concepts of chemical alloying and morphotropic phase boundaries to tune and maximize their responses. While lead-based perovskites dominate the current market of ferroelectric devices, we highlight the need to develop lead-free alternatives, especially in the thin film form, that would enable a seamless integration of these technologies in next-generation devices. This naturally, leads to a discussion of the current state-of-art in ferroelectric thin-film growth and concepts of epitaxy and strain-engineering which have been widely utilized as an additional knob to control structure and responses of these materials. Having cited several examples of large enhancements in ferroelectric properties of thin films *via* epitaxial strain control, we briefly discuss the merits and limitations of current strain-engineering based approaches. This sets up the central goal of the current dissertation and motivates the need to develop new modalities in material growth and design that can extend the limits of strain-engineering and device performance in lead-free ferroelectric materials. We then outline the work presented in this dissertation including the formation of MPB-like features in highly compressively strained $BiFeO_3$ that demonstrate highly enhanced electromechanical responses, as well as the stabilization of the ferroelectric state of $BaTiO_3$ thin films to temperatures exceeding 800°C by employing epitaxial-strain driven alignment of growth-induced defect dipoles. We then outline the organization of chapters in this dissertation, and conclude Chapter 1 with a brief summary of the individual chapters.

7.1.2 Summary of Chapter 2

In Chapter 2, we begin with a discussion of the PLD growth process, followed by a brief description of the experimental setup and the growth parameters that were used to synthesize two prototypical lead-free ferroelectrics studied in this dissertation, namely $BiFeO_3$ and $BaTiO_3$. For each of the two systems, we begin with a brief review of relevant background literature, followed by detailed investigations of the structure, chemistry and property measurements of PLD-grown films. We first demonstrate our ability to grow high-quality epitaxial thin films of $BiFeO_3$ on a variety of single crystal oxide substrates with lattice matched $SrRuO_3$ as a bottom electrode. We then present structural, chemical and ferroelectric studies conducted on these films that demonstrate the excellent quality of the films synthesized. At the same time we describe several characterization techniques including XRD, RBS, RSM, and PFM that have been employed for investigating structure-property relationships throughout this dissertation. We then move on to the study of PLD growth of epitaxial $BaTiO_3$ thin films, where we demonstrate large impact of laser fluence on film quality. Using a combination of XRD, RBS, and TDTR-based thermal conductivity measurements, we demonstrate a laser fluence condition of 1.5 J/cm^2 to be optimum for the growth of epitaxial $BaTiO_3$ thin films. In short, this chapter lays the ground work for the PLD growth as well as various characterization techniques that are important for the research presented in rest of the chapters.

7.1.3 Summary of Chapter 3

In Chapter 3, we investigate new routes for enhanced electromechanical responses by using epitaxial strain in lead-free $BiFeO_3$ to drive the formation of mixed-phase structures that are mechanical analogs to the chemistry driven MPB's found in several lead-based ferroelectrics. Recent studies have observed mixed phase structures of rhombohedral- and tetragonal-polymorphs in highly compressively strained $BiFeO_3$ films that demonstrate enhanced piezoresponse as compared to either of the parent phases. In order to understand these effects, we have examined the intricate nanoscale spatial arrangement of metastable mixed-phase structures that form in highly compressively strained $BiFeO_3$ thin films. Based on detailed characterization of the phase- and surface- structure of these films using a combination of high resolution XRD and scanning probe-based techniques, we have uniquely identified and examined the numerous phases present at these phase boundaries and have discovered an intermediate monoclinic phase

(much akin to what has been observed in MPB systems) in addition to the previously observed rhombohedral- and tetragonal-like phases. They reveal that the so-called mixed-phase films are not mixtures of rhombohedral- and tetragonal-like phases, but intimate mixtures of highly-distorted monoclinic phases (designated as M_I- and M_{II}- phases) with no evidence for the presence of the rhombohedral-like parent phase. With such an understanding of the nanoscale phase structure, we conducted bias-induced nanoscale swithching among the various phases present using PFM to investigate the mechanism for highly enhanced piezoresponses that have been reported in these films. Based on these studies, we show that the ability to reversibly transform from between the monoclinic M_I and M_{II} -phases under external fields are key to the observed enhance electromechanical responses. The findings presented in this chapter represent an unprecedented picture of the phase complexity associated with this exciting strain-induced structural phase transition as well as direct evidence of the pathway for enhanced electromechanical response in these materials. Such unique behavior has significant implications for numerous applications and could help shed light on similar boundaries in other high-performance piezoelectrics.

7.1.4 Summary of Chapter 4

In Chapter 4, we seek to understand the origins of complex mixed phase formation that has been observed in highly compressively strained $BiFeO_3$ thin films. For this, we investigate the temperature- and thickness- dependent structural and morphological evolution of strain-induced phase boundaries in epitaxial $BiFeO_3$ films deposited on $LaAlO_3$ (001) substrates using a combination of high-resolution X-ray diffraction and temperature-dependent scanning-probe-based studies. We observe in these films, a thickness dependent evolution from a single monoclinically distorted metastable tetragonal-like phase, to a complex mixed-phase structure in film of intermediate thickness, to an eventual breakdown in epitaxy to microcrystals of the bulk rhombohedral phase in thicker films. These observations draw parallels with reports of unusual strain-relaxation in strain-stabilized metastable phases of simpler metallic systems, and suggest the possibility of a strain-induced spinodal instability as the cause for the thickness-dependent mixed phase formation in highly strained $BiFeO_3$ films. Based on earlier models that explain the unusual phase evolution in materials that have a strain stabilized metastable phase, we propose a schematic thickness-strain phased diagram to summarize the nature of the phase evolution in strained $BiFeO_3$ thin films. Based on such an understanding of the thickness-driven phase

evolution in epitaxial $BiFeO_3$ films, we then present suitable chemical-alloying strategies that can delay the onset of epitaxial breakdown in the highly compressively strained films and stabilize the necessary nanostructure to assure strong electromechanical responses. By alloying the $BiFeO_3$ with Pb (1-3%) we have stabilized the mixed-phase structures to film thicknesses in excess of 500 nm and have demonstrated surface height depressions greater than 20 nm. These observations provide insight into the nature of the phases of $BiFeO_3$ and their stability and routes to further utilize these materials.

7.1.5 Summary of Chapter 5

In Chapter 5, we demonstrate a new route to engineering strain in materials involving the use of chemical strain from growth-induced defect dipoles in combination with substrate-induced compressive epitaxial strain. More specifically, we utilize the high energetics associated with the PLD growth process to tune the concentration of bombardment-related point defects that occur in $BaTiO_3$ thin films, that in turn form charged point defect complexes also known as defect dipoles. By directly coupling the electrical and elastic dipoles of the defect complexes with the polarization and epitaxial strain state of the film, respectively, we can align the defects thereby inducing an additional anisotropic lattice deformation. Such a coupling of the elastic dipole of the defects with stress has been demonstrated before, but here we develop a new paradigm in strain control of ferroelectric materials whereby we leverage this and the corresponding coupling with the primary order parameter of the materials to enhance material performance. We demonstrate that in $BaTiO_3$ films, known to possess a strong coupling between strain and polarization, that deterministically controlling the electric- and elastic-dipole moments of engineered defect complexes allows us to systematically enhance the T_C to nearly 800°C without degradation of the polarization or leakage properties. This work highlights the potential of the combination of strain- and defect-engineering as a new route to control material properties.

7.1.6 Summary of Chapter 6

In Chapter6, we focus on a novel combination of compressive epitaxial strain and a controlled composition-gradient across the thickness in BST thin films to engineer a state where the in-plane dimensions of the BST unit-cell are held constant by the substrate while the out-of-plane dimension is linearly tuned as a function of composition, thereby, creating an effective out-of-plane strain gradient and associated polarization gradient in the film. Here, we explore the

possibility of using spatial gradients in composition and/or strain to engineer enhanced dielectric responses with excellent temperature stability over a wide temperature range for use in next-generation microwave devices. Preliminary measurements for the temperature-dependence of dielectric susceptibility for epitaxial monodomain graded-BST films grown on $GdScO_3$ (110) substrates with highly controlled composition- and strain- gradients have revealed high values of dielectric permittivity (ε_r ~750) that is stable over a wide temperature range (25-350°C). Furthermore, by comparing our measurements with those from advanced GLD-based models for graded ferroelectric films, we comment on the role of composition gradient, flexoelectric (strain-gradient) and depolarization effects that are important for the observed responses.

7.1.7 Summary of Appendices

Appendix A introduces the PFM technique, showing the experimental setup and procedure for imaging ferroelectric order in materials. **Appendix B** discusses the GLD model constructed for the phenomenological description of the ferroelectric phase transitions in monodomain $BaTiO_3$ films subject to in-plane and out-of-plane strain constrains.

7.2 Suggestions for Future work

1. Pyroelectric and electrocaloric responses of pure M_{II}-phase and mixed-phase $BiFeO_3$: The M_I- and M_{II}- phases that occur in mixed-phase $BiFeO_3$ films have dramatically different structure, ferroelectric and ferromagnetic order parameters. In Chapters 4 and 5, we saw that for thicker films of highly compressively strained $BiFeO_3/LaAlO_3$, it is possible to reversibly transform between the mixed phase state (where tilted-version of M_I- and M_{II}- phases coexist) to one that is purely M_{II}. These transitions can be brought about by application of electric fields or by simply heating the films, and are characterized by changes in the volume and average film polarization. Thus, one could expect large extrinsic contributions to pyroelectric and electrocaloric responses in these films over a wide temperature range where such mixed phase structures stabilize in these films. Experiments that directly measure these responses naturally follow from the work presented in this dissertation. However, there are several challenges for such studies including the difficulty in stabilizing the purely M_{II}- and mixed- phase $BiFeO_3$ phases with a bottom electrode buffer layer that is needed for these measurements.

2. Tuning polymorph stability using substrate orientation: The stabilization of the metastable tetragonal phase of $BiFeO_3$ films on highly compressive 001-oriented substrates is indicative of the role of biaxial strain towards the stabilization of metastable polymorphs that are mechanically compatible with the strain-induced lattice deformation. Such effects are also responsible for the stabilization of the room temperature tetragonal phase of $BaTiO_3$ to temperatures exceeding 400°C in the case of compressively strained 001-oriented films. In a similar manner, it can be argued that compressive epitaxial strain in (111)-oriented films should favor a rhombohedral polymorph with out-of-plane polarization, and a tensile in-plane biaxial strain would stabilize the orthorhombic ferroelectric phase. A thorough understanding of strain-tuning of the stability of polymorphic phases would enable the design of new ferroelectric systems that possess strain-induced MPB like features akin to the one observed in highly compressively strained $BiFeO_3$ thin films. Towards such an understanding, I propose experiments exploring such possibilities on $BaTiO_3$ and other perovskite ferroelectric systems.

3. Engineering functionalities of complex oxide perovskites using lattice strains from defects: Structural and electrical measurements of $BaTiO_3$ thin films (chapter 5) revealed the presence of aligned defect-dipoles that form due to energetic bombardment during PLD growth. These defects in turn generate enhanced anisotropic deformation states with large implications for ferroelectric properties of $BaTiO_3$. Lattice deformation in complex oxide perovskites, in general, strongly impact electronic and magnetic properties. Some representative experimental observations include the enhancement of T_C in superconducting $La_{1.9}Sr_{0.1}CuO_4$ thin films, room temperature ferroelectricity in paraelectric $SrTiO_3$, the metal insulator transition in rare-earth nickelates, the colossal magnetoresistance in $La_{0.67}Ca_{0.33}MnO_x$ and more. I therefore propose experiments that utilize a combination of epitaxial strain and high energy growth-induced defects to induce highly enhanced deformation states (beyond what is possible via epitaxial strain alone) in complex oxide perovskite materials to engineer lattice deforming defects to tune functionalities. To begin with, I propose experiments investigating high energy growth of $SrTiO_3$ films on a variety of substrates including $NdGaO_3$ (110), $SrTiO_3$ (001), and $DyScO_3$ (110) for room temperature ferroelectricity. I also propose possibilities of

enhancing the stability regime of M_{II}-phase $BiFeO_3$ grown on $LaAlO_3$ (001) substrates via additional out-of-plane strains from growth induced defects.

4. Enhanced critical thickness for strain-relaxation in $BaTiO_3$ films with aligned defect dipoles: Critical thickness studies of MBE-grown $BaTiO_3$ films on $DyScO_3$ (110) substrates (compressive strain of ~1.7%) have shown that the critical thickness for strain relaxation is ~50 nm. This limits the potential for epitaxial strain engineering for high voltage applications (such as applications requiring large piezoelectric displacements) where thicker films are needed to avoid leakage and dielectric breakdown related issues. However, using PLD growth at higher laser fluences, we have been able to synthesize $BaTiO_3$ films exceeding 150 nm in thickness that remain coherently strained on $DyScO_3$ (110) substrates. These observations are indicative of the fact that the presence of aligned defect dipoles can dramatically impact strain relaxation in thin films. Earlier theoretical studies have predicted that under conditions of negative hydrostatic pressure (corresponding to a net unit cell volume expansion), anomalous lattice deformation states involving large expansions in the *c*-lattice parameter and anomalous reduction in the *a*-lattice parameter occur in tetragonal ferroelectrics such as $BaTiO_3$. If we were to assume that the introduction of defect dipoles (volume expanding point defect complexes) in the bulk of $BaTiO_3$ can lead to similar effects, then we can expect highly reduced *a*-lattice parameter values for unstrained films with defects as compared to bulk. This would result in an effective lowering of the lattice mismatch with the underlying substrate and explain the observed enhancements in the critical thickness values. Based on such a hypothesis, I propose to conduct a series of experiments involving growth of $BaTiO_3$ films of varying thicknesses with controlled densities aligned defect dipoles followed by detailed studies of evolution of strain relaxation with film thickness using X-ray RSM and TEM based studies.

5. Flexoelectric control of defect dipole alignment: The systematic shift observed in ferroelectric hysteresis loop for $BaTiO_3$ films grown at increasing values of laser fluences towards the positive voltage axis is indicative of increasing densities of aligned defect dipoles. However, the mechanism by which the electric moment of these defects choose

an upward pointing orientation over a downward pointing one is unclear. Consequently, even though we can employ compressive epitaxial strain to enforce an out-of-plane orientation of defect dipoles, we have no way of choosing between upward/downward pointing configurations. The ability to control between the two configurations could provide clues to the origin of the observed symmetry breaking effects. For this, I propose a study where we grow $BaTiO_3$ films with a gradient in defect concentration across film thickness. This can be easily done by continuously varying the laser fluence during growth between 1.5 J/cm^2 to 2.7 J/cm^2. This would result in a longitudinal strain gradient (related to defect density gradient) across the films thickness giving rise to a net built-in field as a consequence of the flexoelectric effect. Thus, by making upward and downward graded films, we could potentially choose between the upward/downward pointing configurations of aligned defect dipoles.

APPENDIX A

FERROELECTRIC DOMAIN ANALYSIS WITH PIEZORESPONSE FORCE MICROSCOPY

Piezoresponse force microscopy (PFM) [216,217] is a scanning probe microscopy (SPM)-based technique used to probe and understand polar materials on the nanoscale. In this appendix we investigate the basic principles of operation for PFM.

A.1 Principles of PFM

PFM is based on the detection of a bias-induced surface deformation in polar materials. Using a scanning probe setup, a tip is brought into contact with the surface of a material and the piezoelectric response of the surface is detected as the tip deflection during application of an AC bias to the tip. In PFM, the tip follows the local deformation of the sample surface that takes place directly at the apex of the tip, driven by the alternating voltage applied to it. The forces acting on the tip can be resolved into 3-components, F_{ver}, F_{lat} and F_{long} that manifest as a vertical deflection, lateral torsion and buckling respectively of the cantilever (Fig. A1). The phase of the electromechanical response of the surface yields information on the polarization direction below the tip (Fig. A2). For domains with polarization pointing normal to the surface for the material, the application of a positive tip bias results in the expansion of the sample and the surface oscillations are in phase with the tip voltage. For domains with downward pointing polarization the response is 180°

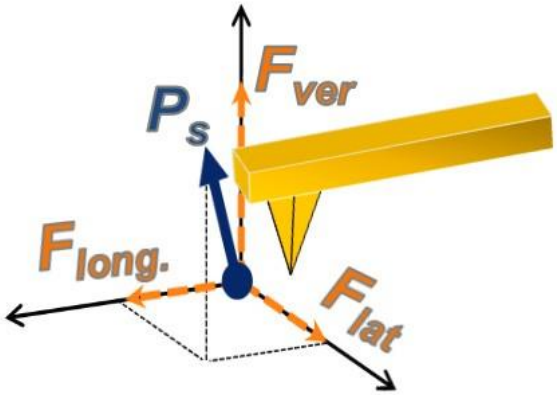

Fig. A.1: Possible movements of the cantilever due to forces acting on the tip.

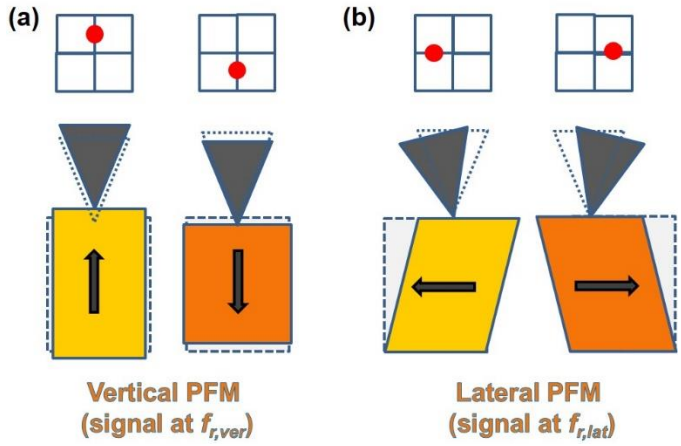

Fig. A2: Schematic for possible movements of the cantilever due to piezoresponse from the ferroelectric film with corresponding change on the detector(a) F_{ver} leading to vertical deflection, and (b) F_{lat} leading to vertical deflection

out of phase. The vertical displacement of the cantilever, giving rise to out-of-plane or the vertical PFM contrast and information about the vertical direction of the polarization. In the same manner, torsion of the cantilever or the lateral deflection in the detector can be measured, thus allowing for determination of the in-plane or the lateral piezoresponse. In order to image the longitudinal response, the image must be recorded again after rotation of the sample by 90°.

A.2 Experimental Setup

A schematic of the experimental setup for PFM is shown in Fig. A3. The left side (Fig. A3, blue box) of the scheme depicts a standard contact mode AFM setup. On the right side (Fig. A3, red box), the additional components for PFM operation are shown. The AC bias is applied to conducting AFM tip (Micromasch 0.6 N/m, tip radius ~20 nm, f_r = 75 kHz) using a function generator and the resulting oscillations of the cantilever are read out with a lock-in-amplifier (LIA). The vertical and lateral PFM images obtained in this dissertation were obtained near resonance to take advantage of the resonant enhancement in signal. The PFM cantilever is excited with an AC bias, V_{ac} (typically 0.1-1 V) with components at both the vertical resonance frequency (f_{ver} ~ 300 kHz) and the lateral resonance frequency (f_{lat} ~ 750 kHz). The vertical and lateral responses are read out by the LIA at the respective frequencies, enabling simultaneous imaging.

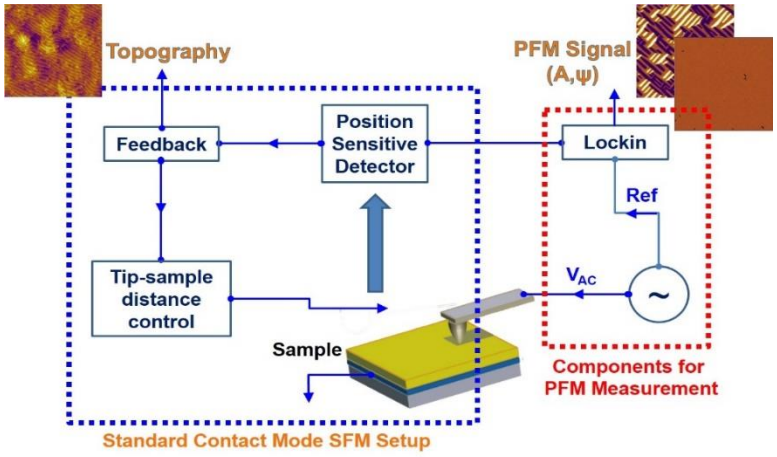

Fig. A3: Schematic for contact-mode scanning force microscopy (left side) upgraded for piezoresponse force microscopy operation (right side).

APPENDIX B

PHENOMENOLOGICAL GLD MODELING OF STRAIN EFFECTS IN MONODOMAIN $BaTiO_3$ THIN FILMS

For this work, we constructed a phenomenological description of the ferroelectric phase transitions in $BaTiO_3$ in which the spontaneous polarization $P = (P_1, P_2, P_3)$ is chosen as the order parameter. The free energy, G, is usually expanded as a polynomial of the polarization components P_i (i =1, 2, 3). In order to more accurately describe the various structural transitions in a $BaTiO_3$ single crystal (*i.e.*, from cubic, paraelectric to tetragonal-ferroelectric to orthorhombic to rhombohedral) we expressed the Ginzburg-Landau-Devonshire Gibbs free energy with an eighth-order polynomial [7,9]. Under stress-free conditions it is given as:

$$G = \alpha_1(P_1^2 + P_2^2 + P_3^2) + \alpha_{11}(P_1^4 + P_2^4 + P_3^4) + \alpha_{12}(P_1^2P_2^2 + P_2^2P_3^2 + P_1^2P_3^2) + \alpha_{111}(P_1^6 + P_2^6 + P_3^6) + \alpha_{112}[P_1^4(P_2^2 + P_3^2) + P_2^4(P_3^2 + P_1^2) + P_3^4(P_1^2 + P_2^2)] + \alpha_{123}P_1^2P_2^2P_3^2 + \alpha_{1111}(P_1^8 + P_2^8 + P_3^8) + \alpha_{1112}[P_1^6(P_2^2 + P_3^2) + P_2^6(P_3^2 + P_1^2) + P_3^6(P_1^2 + P_2^2)] + \alpha_{1122}(P_1^4P_2^4 + P_1^4P_3^4 + P_2^4P_3^4) + \alpha_{1123}(P_1^4P_2^2P_3^2 + P_2^4P_3^2P_1^2 + P_3^4P_2^2P_1^2) \quad (1)$$

where α_1, α_{ij}, and α_{ijk} are the dielectric stiffnesses at constant stress. All of the coefficients are assumed to be temperature-independent except $\alpha_1 = (T - \theta)/(2\varepsilon_0 C)$ where ε_0 is the permittivity of vacuum, C is the Curie-Weiss constant, and θ is the Curie-Weiss temperature. The free energy for a tetragonal c domain with $P = (0,0,P_3)$ in a bi-axially confined $BaTiO_3$ thin film with in-plane stresses $\sigma_1 = \sigma_2$ from the epitaxial constraint of the substrate and out-of-plane stresses σ_3 from the elastic dipole of the defect structures that result in additional lattice deformations are given as:

$$G = \alpha_1P_3^2 + \alpha_{11}P_3^4 + \alpha_{111}P_3^6 + \alpha_{1111}P_3^8 + -\frac{1}{2}s_{11}(\sigma_1^2 + \sigma_2^2 + \sigma_3^2) - s_{12}(\sigma_1\sigma_2 + \sigma_2\sigma_3 + \sigma_1\sigma_3) - \frac{1}{2}s_{44}(\sigma_4^2 + \sigma_5^2 + \sigma_6^2) - Q_{11}\sigma_3P_3^2 - Q_{12}(\sigma_1 + \sigma_2)P_3^2 \quad (2).$$

The strain components can be obtained from the Gibb's free energy from $u_i = -\frac{\delta G}{\delta \sigma_i}$ giving

$$u_1 = s_{11}\sigma_1 + s_{12}(\sigma_2 + \sigma_3) + Q_{12}P_3^2, \quad u_2 = s_{11}\sigma_2 + s_{12}(\sigma_1 + \sigma_3) + Q_{12}P_3^2,$$
$$u_3 = s_{11}\sigma_3 + s_{12}(\sigma_2 + \sigma_1) + Q_{11}P_3^2,\ u_4 = s_{44}\sigma_4,\ u_5 = s_{44}\sigma_5,\ u_6 = s_{44}\sigma_6 \quad (3).$$

Additionally, the strain is easily measurable experimentally using the X-ray diffraction-based techniques and are experimentally found to be:

$$u_1 = u_2 = u_m = \frac{a_{sub}-a_{pc}}{a_{pc}}, u_3 = \frac{c_{film}-a_{pc}}{a_{pc}}, u_4 = u_5 = u_6 = 0 \qquad (4)$$

where u_m is the epitaxial misfit strain from the substrate, $a_{sub}$is the pseudocubic in-pane lattice parameter of the substrate, and $a_{pc}$is the pseudocubic lattice parameter of $BaTiO_3$. Using Eqs. (3) and (4), we can calculate the various stress components as

$$\sigma_1 = \sigma_2 = \sigma_m = \frac{(s_{12}Q_{11}-s_{11}Q_{12})P_3^2}{(s_{11}-s_{12})(s_{11}+2s_{12})} + \frac{(s_{11}u_m-s_{12}u_3)}{(s_{11}-s_{12})(s_{11}+2s_{12})} \qquad (5)$$

$$\sigma_3 = \frac{(2s_{12}Q_{12}-s_{11}Q_{11}+s_{12}Q_{11})P_3^2}{(s_{11}-s_{12})(s_{11}+2s_{12})} + \frac{(s_{11}+s_{12})u_3-2s_{12}u_m}{(s_{11}-s_{12})(s_{11}+2s_{12})}, \sigma_4 = \sigma_5 = \sigma_6 = 0 \qquad (6).$$

Given the mechanical constraints on the films from the substrate, it is convenient to apply the Helmholtz free energy *F* that can be derived from the Legendre transformation of Gibbs free energy *G* via $F = G + \sum_{n=1}^{6} \sigma_n u_n$ that yields

$$F = [\alpha_1 + \frac{(2s_{12}Q_{12}-s_{11}Q_{11}+s_{12}Q_{11})u_3}{(s_{11}-s_{12})(s_{11}+2s_{12})} + \frac{(s_{12}Q_{11}-s_{11}Q_{12})u_m}{(s_{11}-s_{12})(s_{11}+2s_{12})}]P_3^2 + [\alpha_{11} + \frac{2s_{12}Q_{12}^2+(s_{11}+s_{12})Q_{12}^2-4s_{11}Q_{11}Q_{12}}{(s_{11}-s_{12})(s_{11}+2s_{12})}]P_3^4 + \alpha_{111}P_3^6 + \alpha_{1111}P_3^8 + -\frac{1}{2}s_{11}(\sigma_1^2+\sigma_2^2+\sigma_3^2) - s_{12}(\sigma_1\sigma_2+\sigma_2\sigma_3+\sigma_1\sigma_3) - \frac{1}{2}s_{44}(\sigma_4^2+\sigma_5^2+\sigma_6^2) - Q_{11}\sigma_3P_3^2 - Q_{12}(\sigma_1+\sigma_2)P_3^2 \qquad (7)$$

where s_{mn} are the elastic compliances at constant polarization and Q_{ij} are the electrostrictive constants of the paraelectric phase. Thus, the spontaneous polarization of the tetragonal *c* domains can be obtained as a function of temperature by minimizing the free energy and solving the equation $\alpha_1^* + 2\alpha_{11}^* P_3^2 + 3\alpha_{111}P_3^4 + 4\alpha_{1111}P_3^6 = 0$ where $\alpha_1^* = [\alpha_1 + \frac{(2s_{12}Q_{12}-s_{11}Q_{11}-s_{12}Q_{11})u_3}{(s_{11}-s_{12})(s_{11}+2s_{12})} + \frac{(s_{12}Q_{11}-s_{11}Q_{12})u_m}{(s_{11}-s_{12})(s_{11}+2s_{12})}]$ and $\alpha_{11}^* = [\alpha_{11} + \frac{2s_{12}Q_{12}^2+(s_{11}+s_{12})Q_{12}^2-4s_{11}Q_{11}Q_{12}}{(s_{11}-s_{12})(s_{11}+2s_{12})}]$. Finally, to calculate the temperature dependence of polarization, we use coefficients that are within the range of values used in Ref. 60 or from our own data: Q_{11} = 0.10 $m^4 C^2$, Q_{12} = −0.042 $m^4 C^2$, s_{11} = 9.4×10^{-12} m^2/N, s_{12} = −3.0×10^{-12} m^2/N, C_0 = 1.0×10^5, α_{11} = −508.55α_0 N $m^6 C^4$, α_{111} = 3137.11α_0 N m^{10} C^6, and α_{1111} = 93673.45α_0 N m^{14} C^8 where $\alpha_0 = 1/(2\varepsilon_0 C)$. Utilizing these we obtain the equation:

$$(T-115) - 42233(0.38u_3 - 0.09u_m) + 933.21P_3^2 + 9411.33P_3^4 + 374693.8P_3^6 = 0 \qquad (8)$$

The predicted evolution of polarization as a function of temperature for the coherently strained $BaTiO_3$ films grown on $GdScO_3$ (110) substrates corresponding to an epitaxial compressive strain of 0.99%, for defect free films as well as films grown at fluences of 1.5, 1.8, and 2.1 J/cm^2 possessing additional out-of-plane strains (u_3) of 0.6%, 1.4%, and 2.4%, respectively, are provided (Fig. B1). We can express the total out-of-plane strain for these films as $u_3 = u_{3i} + u_{3d}$, where u_{3i} is the out-of-plane strain for a defect-free (ideal) material and u_{3d} is the excess out-of-plane strain from defects. Thus, utilizing the fact that $P = 0$ at $T = T_C$ we can write out the following relationship which directly relates the expected T_C to the anisotropic lattice deformation from growth induced defects:

$$T_C = 115 + 42233[(0.38(u_{3i}+u_{3d}) - 0.09u_m] = T_{C_{defect-free}} + 16048.54u_{3d} \quad (9)$$

This relationship predicts the ferroelectric-to-paraelectric phase transitions for the films grown at fluences of 1.5, 1.8, and 2.1 J/cm^2 to be 515°C, 650°C, and 810°C, respectively, as compared to 425°C for the defect-free coherently strained films. These predicted values match closely the experimentally observed phase transition temperatures.

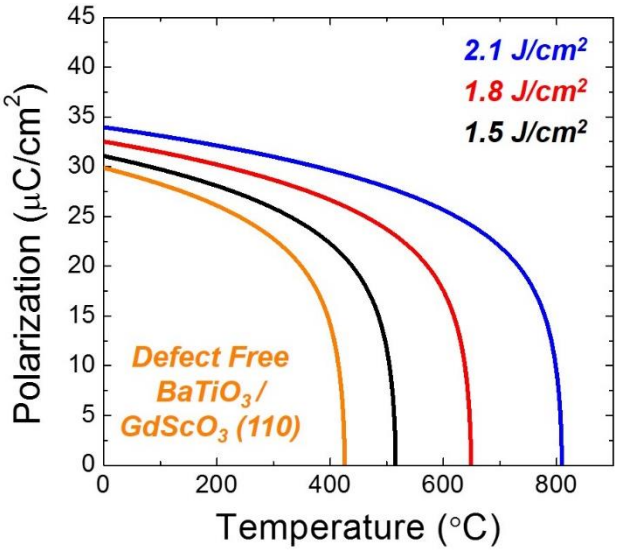

Fig. B1: Predicted temperature-evolution of polarization in coherently strained $BaTiO_3/GdScO_3$ (110) heterostructures possessing various levels of additional out-of-plane strain as measured by X-ray diffraction. The transition temperature scales with increasing out-of-plane lattice distortion which corresponds to increasing laser fluence.

REFERENCES

[1] B. Jaffe, W. R. Cook, H. Jaffe, *Piezoelectric Ceramics* (Academic, London, 1971).

[2] J. F. Scott, C. A. Araujo, *Science* **1989**, 246, 954.

[3] R. E. Newnham, G. R. Ruschau, *J. Amer. Cer. Soc.* **1991**, 74, 463.

[4] G. H. Haertling, *J. Am. Ceram. Soc.* **1999**, 82, 797.

[5] J. F. Scott, *Science* **2007**, 315, 954.

[6] Y. Qi, N. T. Jafferis, K. Lyons, Jr., C. M. Lee, H. Ahmad, M. C. McAlpine, *Nano Lett.* **2010**, 10, 524.

[7] E. Fatuzzo, W. E. Merz, *Ferroelectricity* (North-Holland, Amsterdam, 1967).

[8] T. Mitsui, I. Tatsuzaki, E. Nakamura, *An Introduction to the Physics of Ferroelectrics* (Gordon & Breach, London, 1976).

[9] M. E. Lines, A. M. Glass, *Principles and Applications of Ferroelectrics and Related Materials* (Oxford University Press, New York, 1977).

[10] K. M. Rabe, M. Dawber, C. Lichtensteiger, C. H. Ahn, J. -M. Triscone, *Physics of Ferroelectrics: A Modern Perspective* (Springer-Verlag, Berlin, 2007).

[11] B. A. Strukov, A. P. Levanyuk, *Ferroelectric Phenomena in Crystals* (Springer-Verlag, Berlin, 1998).

[12] J. F. Nye, *Physical Properties of Crystals* (Oxford University Press, New York, 1985).

[13] L. E. Cross, *Ferroelectric Ceramics: Tailoring Properties for Specific Applications* (Birkhäuser Basel, 1993).

[14] A. K. Tagantsev, L. E. Cross, J. Fousek, *Domains in Ferroic Crystals and Thin Films* (Springer-Verlag, Berlin, 2010).

[15] H. Ishiwara, M. Okuyama, Y. Arimoto (Eds.), *Ferroelectric Random Access Memories* (Springer-Verlag, Berlin, 2004).

[16] J. F. Scott, *Ferroelectric Memories (*Springer, Berlin, 2000).

[17] W. G. Cady, *Piezoelectricity* (McGraw-Hill & Co., New York, 1946).

[18] D. Damjanovic, *Rep. Prog. Phys*. **1998**, 61, 1267.

[19] J. Valasek, *Phys. Rev.* **1920**, 15, 537.

[20] G. Busch, P. Scherrer, *Naturwiss* **1935**, 23, 737.

[21] G. Busch, *Ferroelectrics* **1987**, 74, 267.

[22] L. E. Cross, R. E. Newnham, *History of Ferroelectrics, Ceramics and Civilization, Vol. III* (The American Ceramic Society, Ohio, 1987).

[23] S. A. Chambers, T. C. Droubay, C. M Wang, K. M. Rosso, S. M. Heald, D. A. Schwartz, K. R. Kittilstved, D. R. Gamelin, *Mater. Today* **2006**, 9, 28.

[24] A. P. Ramirez, *J. of Phys.: Condens. Matter* **1997**, 9, 8171.

[25] G. Chen, J.-M. Langlois, Y. Guo, W. A. Goddard III, *Proc. Natl. Acad. Sci. USA* **1989**, 86(10), 3447.

[26] Y. Kobayashi, S. Endo, K. Deguchi, L.C. Ming, G. Zou, *Solid State Commun.* **2001**, 120, 515.

[27] R. E. Cohen, *Journal of Physics and Chemistry of Solids* **2000**, 61, 139.

[28] R.E. Cohen, *Nature* **1992**, 358, 136.

[29] N. A. Hill, *Annu. Rev. Mater. Res*. **2002**, 32, 1.

[30] C. Ederer, N. A. Spaldin, *Phys. Rev. Lett*. **2005**, 95, 257601.

[31] K. A. Miiller, H. Burkhard, *Phys. Rev. B* **1979**, 19, 3593.

[32] O. G. Vendik, *Ferroelectrics for Microwave Applications* (Soviet Radio, Moscow, 1979).

[33] E. Cross, *Nature* **2004**, 432, 24.

[34] M. J. Haun, E. Furman, S. J. Jang, L. E. Cross, *Ferroelectrics* **1989**, 99, 13.

[35] S. A. Mabud, *J. App. Cryst.* **1980**, 13, 211.

[36] X. –H. Du, J. Zheng, U. Belengundu, K. Uchino, *Appl. Phys. Lett.* **1998**, 72, 2421.

[37] B. Noheda, D. E. Cox, G. Shirane, J. A. Gonzalo, L. E. Cross, S. E. Park, *Appl. Phys. Lett.* **1999**, 74, 2059.

[38] B. Noheda, J. A. Gonzalo, L. E. Cross, R. Guo, S. –E. Park, D. E. Cox, G. Shirane, *Phys. Rev. B*. **2000**, 61(13), 8687.

[39] R. Guo, L. E. Cross, S. E. Park, B. Noheda, D. E. Cox, G. Shirane, *Phys. Rev. Lett.* **2000**, 84, 5423.

[40] H. Fu, R. E. Cohen, *Nature* **2000**, 403, 281.

[41] R. E. Cohen, *Nature* **2006**, 441, 941.

[42] M. Ahart, M. Somayazulu, R. E. Cohen, P. Ganesh, P. Dera, H.-K. Mao, R. J. Hemley, Y. Ren, P. Liermann, Z. Wu, *Nature* **2008**, 451, 545.

[43] B. Noheda, D. E. Cox, *Phase Transitions* **2006**, 79(1-2), 5.

[44] Y. Saito, H. Takao, T. Tani, T. Nonoyama, K. Takatori, T. Homma, T. Nagaya, M. Nakamura, *Nature* **2004**, 432, 84.

[45] S. –T. Zhang, A. B. Kounga, E. Aulbach, T. Granzow, W. Jo, H. -J. Kleebe, J. Rödel, *J. App. Phys.* **2008**, 103 (3), 34107.

[46] C. Ma, H. Guo, S. P. Beckman, X. Tan, *Phys. Rev. Lett.* **2012**,109 (10), 107602.

[47] N. Setter, D. Damjanovic, L. Eng, G. Fox, S. Gevorgian, S. Hong, A. Kingon, H. Kohlstedt, N. Y. Park, G. B. Stephenson, I. Stolitchnov, A. K. Taganstev, D. V. Taylor, T. Yamada, S, Streiffer, *J. App. Phys*. **2006**, 100, 051606.

[48] D. G. Schlom, L. Q. Chen, C. B. Eom, K. M. Rabe, S. K. Streiffer, J. M. Triscone, *Annu. Rev. Mater. Res.* **2007**, 37, 589.

[49] M. Dawber, K. M. Rabe, J. F. Scott, *Rev. Mod. Phys.* **2005**, 77, 1083.

[50] L. W. Martin, Y. –H. Chu, R. Ramesh, *Material Science and Engineering Reports: R* **2010**, 68, 89.

[51] S. B. Krupanidhi, N. Matei, M. Sayer, K. El-Assal, *J. Appl. Phys.* **1983**, 54, 6601.

[52] R. R. Das, D. M. Kim, S. H. Baek, F. Zavaliche, S.-Y. Yang, X. Ke, S. K. Streiffer, M. S. Rzchowski, R. Ramesh, C. B. Eom, *Appl. Phys. Lett.* **2006**, 88, 242904.

[53] T. O. M. Aratani, T. Oikawa, H. Funakubo, *Appl. Phys. Lett.* **2001**, 79, 1000.

[54] S. Y. Yang, F. Zavaliche, L. Mohaddes-Ardabili, V. Vaithyanathan, D.G. Schlom, Y. J. Lee, Y. H. Chu, M. P. Cruz, Q. Zhan, T. Zhao, R. Ramesh, *Appl. Phys. Lett.* **2005**, 87, 102903.

[55] R. Eason, *Pulsed Laser Deposition of Thin Films* (John Wiley & Sons, New Jersey, 2007).

[56] C. D. Theis, D. G. Schlom, *J. Crystal Growth* **1997**, 174, 473.

[57] H. M. Christen, G. Eres, *J. Phys.: Condens. Matter* **2008**, 20, 264005.

[58] J. C. Jiang, X. Q. Pan, W. Tian, C. D. Theis, D. G. Schlom, *Appl. Phys. Lett.* **1999**, 74, 2851.

[59] G.J.H.M. Rijnders, G. Koster, D.H.A. Blank, H. Rogalla, *Appl. Phys. Lett.* **1997**, 70(14), 1888.

[60] K. J. Choi, M. Biegalski, Y. L. Li, A. Sharan, J. Schubert, R. Uecker, P. Reiche, Y. B. Chen, X. Q. Pan, V. Gopalan, L. Q. Chen, D. G. Schlom, C. B. Eom, *Science* **2004**, 306, 1005.

[61] J. H. Haeni, P. Irvin, W. Chang, R. Uecker, P. Reiche, Y. L. Li, S. Choudhary, W. Tian, M. E. Hawley, B. Craigo, A. K. Tagantsev, X. Q. Pan, S. K. Streiffer, L. Q. Chen, S. W. Kirchoefer, J. Levy, D. G. Sclom, *Nature* **2005**, 430, 758.

[62] Y.-H. Chu, M. P. Cruz, C. H. Yang, L. W. Martin, P. L. Yang, J. X. Zhang, K. Lee, P. Yu, L. Q. Chen, R. Ramesh, *Adv. Mater.* **2007**, 19, 2662.

[63] R. J. Zeches, M. D. Rossell, J. X. Zhang, A.J. Hatt, Q. He, C. –H. Yang, A. Kumar, C. H. Wang, A. Melville, C. Adamo, G. Sheng, Y. -H. Chu, J. H. Ihlefeld, R. Erni, C. Ederer, V. Gopalan, L. Q. Chen, D. G. Schlom, N.A. Spaldin, L. W. Martin, R. Ramesh, *Science* **2009**, 326, 977.

[64] D. Dijkkamp, T. Venkatesan, X. D. Wu, S. A. Shaheen, N. Jisrawi, Y. H. Minlee, W.L. Mclean, M. Croft, *Appl. Phys. Lett.* **1987**, 51, 619

[65] R. Ramesh, K. Luther, B. Wilkens, D. L. Hart, E. Wang, J. M. Tarascon, A. Inam, X. D. Wu, T. Venkatesan, *Appl. Phys. Lett.* **1990**, 57, 1505.

[66] J. S. Horwitz, K. S. Grabowski, D. B. Chrisey, R. E. Leuchtner, *Appl. Phys. Lett.* **1991**, 59, 1565

[67] M. Ohring, *Materials Science of Thin Films: Deposition and Structure* (Academic Press, San Francisco, 2002).

[68] D. L. Smith, *Thin-Film Deposition: Principles and Practice* (McGraw Hill, San Francisco, 1995).

[69] E. Breckenfeld, R. Wilson, J. Karthik, A. R. Damodaran, D. G. Cahill, L. W. Martin, *Chem. Mater.* **2012**, 24(2), 331 (2012).

[70] Ohnishi, M. Lippmaa, T. Yamamoto, S. Meguro, H. Koinuma, *Appl. Phys. Lett.* **2005**, 87, 241919.

[71] D. S. Kan, Y. Shimakawa, *Appl. Phys. Lett.* **2011**, 99, 081907.

[72] L. Qiao, T. C. Droubay, V. Shutthanandan, Z. Zhu, P. V. Sushko, S. A. Chambers, *J. Phys. Condens. Matter* **2010**, 22, 312201.

[73] W. Eerenstein, N. D. Mathur, J. F. Scott, *Nature* **2006**, *442*, 759.

[74] L. W. Martin, Y.-H. Chu, R. Ramesh, *Mater. Sci. Eng. R* **2010**, *68*, 89.

[75] G. Catalan, J. F. Scott, *Adv. Mater.* **2009**, 21, 2463.

[76] F. Kubel, H. Schmid, *Acta. Cryst.* **1990**, 698, B46.

[77] F. Zavaliche, S. Y. Yang, T. Zhao, Y. –H. Chu, M. P. Cruz, C. B. Eom, R. Ramesh, *Phase Transit.* **2006**, 79, 991.

[78] J. B. Neaton, C. D. Ederer, U. V. Waghmare, N. A. Spaldin, K. M. Rabe, *Physical Review B* **2005**, 71, 014113.

[79] P. Ravindran, R. Vidya, A. Kjekshus, H. Fjellvag, *Physical Review B* **2006**, 74, 224412.

[80] J. Wang, J. B. Neaton, H. Zheng, V. Nagarajan, S. B. Ogale, B. Liu, D. Viehland, V. Vaithyanathan, D. G. Schlom, U. V. Waghmare, N. A. Spaldin, K. M. Rabe, M. Wuttig, R. Ramesh, *Science* **2003**, 299, 1719.

[81] J. R. Teague, R. Gerson, W. J. James, *Solid State Communications* **1970**, 8, 1073.

[82] P. Fischer, M. Polomska, I. Sosnowska, M. Szymanski, *J. Physics C-Solid State Physics* **1980**, 13, 1931.

[83] A. M. Kadomtseva, A. K. Zvezdin, Y. F. Popov, A. P. Pyatakov, G. P. Vorob'ev, *JETP Lett.* **2004**, 79, 571.

[84] C. Ederer, N. A. Spaldin, *Physical Review B* **2005**, 71, 060401.

[85] V. Berger, Phys. Rev. Lett. **1998**, 81, 4136.

[86] S. V. Kalinin, D.A. Bonnell, T. Alvarez, X. Lei, Z. Hu, R. Shao, J. H. Ferris, *Adv. Mater.* **2005**, 17, 795.

[87] J. Seidel, L. W. Martin, Q. He, Q. Zhan, Y.-H. Chu, A. Rother, M. E. Hawkridge, P. Maksymovych, P. Yu, M. Gajek, N. Balke, S. V. Kalinin, S. Gemming, F. Wang, G. Catalan, J. F. Scott, N. A. Spaldin, J. Orenstein, R. Ramesh, *Nature Mater.* **2009**, 8, 229.

[88] C. B. Eom, R. B. Vandover, J. M. Phillips, D. J. Werder, J. H. Marshall, C. H. Chen, R. J. Cava, R. M. Fleming, D. K. Fork, *Appl. Phys. Lett.* **1992**, 63, 2573.

[89] A. K. Tagantsev, I. Stolichnov, E. L. Colla, N. Setter, *J. Appl. Phys.* **2001**, 90, 1387.

[90] T. Morimoto, M. Takase, T. Ito, H. Kato, Y. Ohki, *Jpn. J. Appl. Phys.* **2000**, 39, 2110.

[91] G. Gerra, A. K. Tagantsev, N. Setter, K. Parlinski, *Phys. Rev. Lett.* **2006**, 96, 107603.

[92] Y.-H. Chu, Q. Zhan, L.W. Martin, M.P. Cruz, P.-L. Yang, G.W. Pabst, F. Zavaliche, S.-Y. Yang, J.-X. Zhang, L.-Q. Chen, D.G. Schlom, I.-N. Lin, T.-B. Wu, R. Ramesh, *Adv.Mater.* **2006**, 18, 2307.

[93] Z. H. Chen, A. R. Damodaran, R. Xu, S. Lee, L. W. Martin, *App. Phys. Lett.* **2014**, 104, 182908.

[94] P. Yu, W. Luo, D. Yi, J. X. Zhang, M. D. Rossell, C. H. Yang, L. You, G. Singh-Bhalla, S. Y. Yang, Q. He, Q. M. Ramasse, R. Erni, L. W. Martin, Y. –H. Chu, S. T. Pantelides, S. J. Pennycook, R. Ramesh, *Proc. Natl. Acad. Sci. U.S.A.* **2012**, 109, 9710.

[95] S.K. Streiffer, C.B. Parker, A.E. Romanov, M.J. Lefevre, L. Zhao, J.S. Speck, W. Pompe, C.M. Foster, G.R. Bai, *J. Appl. Phys.* **1998**, 83, 2742.

[96] J.X. Zhang, Y.L. Li, S. Choudhury, L.Q. Chen, Y.H. Chu, F. Zavaliche, M.P. Cruz, R. Ramesh, Q.X. Jia, *J. Appl. Phys.* **2008**, 103, 094111.

[97] Y.-H. Chu, Q. He, C.-H. Yang, P. Yu, L.W. Martin, P. Shafer, R. Ramesh, *Nano Lett.* **2009**, 9, 1726.

[98] S. V. Kalinin, B. J. Rodriguez, S. Jesse, E. Karapetian, B. Mirman, E. A. Eliseev, A. N. Morozovska, *Annu. Rev. Mater. Res.* **2007**, 37, 189.

[99] H. Chazono, H. Kishi, *Jpn. J. Appl. Phys.* **2001**, 40 (9B), 5624.

[100] E. Breckenfeld, R. Wilson, L. W. Martin, *Appl. Phys. Lett.* **2013**, 103, 082901.

[101] D. G. Cahill, W. K. Ford, K. E. Goodson, D. G. Mahan, A. Majumdar, H. J. Maris, R. Merlin, S. R. Phillpot, *J. Appl. Phys.* **2003**, 93, 793.

[102] D. G. Cahill, *Rev. Sci. Instrum.* **2004**, 75, 5119.

[103] S. Fujino, M. Murakami, S.-H. Lim, V. Nagarajan, C. J. Fennie, M. Wuttig, L. Salamanca-Riba, I. Takeuchi, *Appl. Phys. Lett.* **2008**, 92, 202904.

[104] J. X. Zhang, B. Xiang, Q. He, J. Seidel, R. J. Zeches, P. Yu, S. Y. Yang, C. H. Wang, Y-H. Chu, L. W. Martin, A. M. Minor, R. Ramesh, *Nat. Nanotechnol.* **2011**, 6, 98.

[105] C. Ederer, N. A. Spaldin, *Phys. Rev. Lett.* **2005**, 95, 257601.

[106] P. Ravindran, R. Vidya, A. Kjekshus, H. Fjellvåg, *Phys. Rev. B* **2006**, 74, 224412.

[107] D. Ricinschi, K.-Y. Yun, M. Okuyama, *J. Phys. Condens. Matter* **2006**, 18, L97.

[108] H. Béa, B. Dupé, S. Fusil, R. Mattana, E. Jacquet, B. Warot-Fonrose, F. Wilhelm, A. Rogalev, S. Petit, V. Cros, A. Anane, F. Petroff, K. Bouzehouane, G. Geneste, B. Dkhil, S. Lisenkov, I. Ponomareva, L. Bellaiche, M. Bibes, A. Barthélémy, *Phys. Rev. Lett.* **2009**, 102, 217603.

[109] B. Dupé, I. C. Infante, G. Geneste, P.-E. Janolin, M. Bibes, A. Barthélémy, S. Lisenkov, L. Bellaiche, S. Ravy, B. Dkhil, *Phys. Rev. B* **2010**, 81, 144128.

[110] D. Mazumdar, V. Shelke, M. Iliev, S. Jesse, A. Kumar, S. V. Kalinin, A. P. Baddorf, A. Gupta, *Nano Lett.* **2010**, 10, 2555.

[111] B. Noheda, D. E. Cox, G. Shirane, S.-E. Park, L. E. Cross, Z. Zhong, *Phys. Rev. Lett.* **2001**, 86, 3891.

[112] G. Xu, H. Hiraka, G. Shirane, J. Li, J. Wang, D. Viehland, *Appl. Phys. Lett.* **2005**, 86, 182905.

[113] K. Saito, A. Ulyanenkov, V. Grossman, H. Ress, L. Bruegemann, H. Ohta, T. Kurosawa, S. Ueki, H. Funakubo, *Jpn. J. Appl. Phys.* **2006**, 45, 7311.

[114] D. H. Kim, H. N. Lee, M. D. Biegalski, H. M. Christen, *Appl. Phys. Lett.* **2008**, 92, 012911.

[115] J. H. Nam, H. S. Kim, A. J. Hatt, N. A. Spaldin, H. M. Christen, arXiv:1010.0254v1 [cond-mat.mtrl-sci]

[116] A. Kumar, S. Denev, R. J. Zeches, E. Vlahos, N. J. Podraza, A. Melville, D. G. Schlom, R. Ramesh, V. Gopalan, *Appl. Phys. Lett.* **2010**, 97, 112903.

[117] A. R. Damodaran, C.-W. Liang, Q. He, C.-Y. Peng, L. Chang, Y.-H. Chu, L. W. Martin, *Adv. Mater.* **2011**, 23, 3170.

[118] R. K. Vasudevan, Y. Liu, J. Li, W.-I. Liang, A. Kumar, S. Jesse, Y.-C. Chen, Y.-H. Chu, V. Nagarajan, S. V. Kalinin, *Nano Lett.* **2011**, 3346, 11.

[119] H. M. Christen, J. H. Nam, H. S. Kim, A. J. Hatt, N. A. Spaldin, *Phys. Rev. B* **2010**, 83, 144107.

[120] Z. Chen, Z. Luo, C. Huang, Y. Qi, P. Yang, L. You, C. Hu, T. Wu, J. Wang, C. Gao, T. Sritharan, L. Chen, *Adv. Funct. Mater.* **2011**, 21, 133.

[121] G. W. MacDougall, H. M. Christen, W. Siemons, M. D. Biegalski, J. L. Zarestky, S. Liang, E. Dagotto, S. E. Nagler, arXiv: 1107.2975v1.

[122] J. Kreisel, P. Jadhav, O. Chaix-Pluchery, M. Varela, N. Dix, F. Sanchez, J. Fontcuberta, arXiv: 1107.5801v1.

[123] K. Y. Choi, S. H. Do, P. Lemmens, D. Wulferding, C. S. Woo, J. H. Lee, K. Chu, C. H. Yang, arXiv: 1108.4484v1.

[124] R. Bruinsma, A. Zangwill, *J. Physique* **1986**, 47, 2055.

[125] W. D. Nix, *Metall. Trans. A* **1989**, 20, 2217.

[126] L. B. Freund, S. Suresh, *Thin Film Materials: Stress, Defect Formation, and Surface* (Cambridge University Press, New York, 2003).

[127] Y. Kuk, L. C. Feldman, P. J. Silverman, *Phys. Rev. Lett.* **1983**, 50, 511.

[128] A. T. Fiory, J. C. Bean, L. C. Feldman, I. K. Robinson, *J. Appl. Phys.* **1984**, 56, 1227.

[129] R. F. C. Farrow, *J. Vac. Sci. Tech. B* **1983**, 1, 222.

[130] R. F. C. Farrow, D. S. Robertson, G. M. Williams, A. G. Cullis, G. R. Jones, I. M. Young, P. N. J. Dennis, *J. Cryst. Growth* **1981**, 54, 507.

[131] G. A. Prinz, *Phys. Rev. Lett.* **1985**, 54, 1051.

[132] D. Lebeugle, D. Colson, A. Forget, M. Viret, P. Bonville, J. F. Marucco, S. Fusil, *Phys. Rev. B* **2007**, 76, 024116.

[133] S. Lee, T. Choi, W. Ratcliff II, R. Erwin, S.-W. Cheong, V. Kiryukhin, *Phys. Rev. B* **2008**, 78, 100101.

[134] M. K. Singh, W. Prellier, M. P. Singh, R. S. Katiyar, and J. F. Scott, *Phys. Rev. B* **2008**, 77, 144403.

[135] A. Hatt, N. A. Spaldin, C. Ederer, *Phys. Rev. B* **2010**, 81, 054109.

[136] O. Diéguez, O. E. González-Vázquez, J. C. Wojdeł, J. Íñiguez, *Phys. Rev. B* **2010**, 83, 094105.

[137] P. C. Clapp, *Phys. Stat. Sol. (b)* **1973**, 57, 561.

[138] A. Boyne, S. A. Dregia and Y. Wang, *Appl. Phys. Lett.* **2011**, 99, 063111.

[139] W. M. McGee, R. S. Williams, M. J. Ashwin, T. S. Jones, *Surf. Sci.* **2006**, 200, 194.

[140] Z. Chen, Z. Luo, C. Huang, Y. Qi, P. Yang, L. You, C. Hu, T. Wu, J. Wang, C. Gao, T. Sritharan, L. Chen, *Adv. Funct. Mater.* **2011**, 21, 133.

[141] S. A. Harrington, J. Zhai, S. Denev, V. Gopalan, H. Wang, Z. Bi, S. A. T. Redfern, S.-H. Baek, C. W. Bark, C.-B. Eom, Q. Jia, M. E. Vickers, J. L. MacManus-Driscoll, *Nature Nanotechnol*. **2011**, 6, 491.

[142] V. M. Mukhortov, Y. I. Golovko, V. M. Mukhortov, V. P. Dudkevich, *Sov. Phys. J.* **1981**, 24, 102.

[143] V. M. Mukhortov, Y. I. Golovko, V. A. Aleshin, E. V. Sviridov, V. M. Mukhortov, V. P. Dudkevich, E. G. Fesenko, *Phys. Stat. Sol. A* **1983**, 77, K37.

[144] K. Abe, S. Komatsu, N. Yanase, K. Sano, T. Kawakubo, *Jpn. J. Appl. Phys.* **1997**, 36, 5575.

[145] T. Kawakubo, S. Komatsu, K. Abe, K. Sano, N. Yanase, N. Fukushima, *Jpn. J. Appl. Phys.* **1998**, 37, 5108.

[146] D. Fu, K. Fukamachi, N. Sakamoto, N. Wakiya, H. Suzuki, M. Itoh, T. Nishimatsu, arXiv: 1102.4473.

[147] J. Sinsheimer, S. J. Callori, B. Ziegler, B. Bein, P. V. Chinta, A. Ashrafi, R. L. Headrick, M. Dawber, *Appl. Phys. Lett.* **2013**, 103, 242904.

[148] S. Tinte, K. M. Rabe, D. Vanderbilt, *Phys. Rev. B* **2003**, 68, 144105.

[149] N. Yanase, K. Abe, N. Fukushima, T. Kawakubo, *Jpn. J. Appl. Phys.* **1999**, 38, 5305.

[150] K. Abe, N. Yanase, T. Yasumoto, T. Kawakubo, *J. Appl. Phys.* **2002**, 91, 323.

[151] S. Lee, C. A. Randall, *J. Am. Ceram. Soc.* **2008**, 91, 1748.

[152] Y. Sakabe, H. Takgi, *Jpn. J. Appl. Phys*. **2002**, 41, 6461.

[153] S. B. Majumder, Y. N. Mohapatra, D. C. Agrawal, *Appl. Phys. Lett.* **1997**, 70, 138.

[154] S. Zhang, R.E. Eitel, C.A. Randall, T.R. Shrout, E.F. Alberta, *Appl. Phys. Lett.* **2005**, 86, 262904.

[155] X. Ren, *Nature Mater.* **2004**, 3, 91.

[156] D. Lee, B. C. Jeon, S. H. Baek, S. M. Yang, Y. J. Shin, T. H. Kim, Y. S. Kim, J.-G. Yoon, C.-B. Eom, T. W. Noh, *Adv. Mater.* **2012**, 24, 6490.

[157] W. Hu, Y. Liu, R. L. Withers, T. J. Frankcombe, L. Noren, A. Snashall, M. Kitchin, P. Smith, B. Gong, H. Chen, J. Schiemer, F. Brink, J. Wong-Leung, *Nature Mater.* **2013**, 12, 821.

[158] S. V. Kalinin, A. Borisevich, D. Fong, *ACS Nano* **2012**, 6, 10423.

[159] T. Ohnishi, M. Lippmaa, T. Yamamoto, S. Meguro, H. Koinuma, *Appl. Phys. Lett.* **2005**, 87, 241919.

[160] E. Breckenfeld, R. Wilson, J. Karthik, A. R. Damodaran, D. G. Cahill, L. W. Martin, *Chem. Mater.* **2012**, 24, 331.

[161] D. S. Kan, Y. Shimakawa, *Appl. Phys. Lett.* **2011**, 99, 081907.

[162] P. R. Willmott, J. R. Huber, *Rev. Mod. Phys.* **2000**, 72, 315.

[163] J. Perrière, E. Millon, W. Seiler, C. Boulmer-Leborgne, V. Craciun, O. Albert, J. C. Loulergue, J. Etchepare, *J. Appl. Phys.* **2002**, 91, 690.

[164] J.-P. Maria, S. Trolier-McKinstry, D. G. Schlom, M. E. Hawley, G. W. Brown, *J. Appl. Phys.* **1998**, 83, 4373.

[165] H. L. Tuller, S. R. Bishop, *Annu. Rev. Mater. Res*. **2011**, 41, 369.

[166] D. M. Smyth, *Ann. Rev. Mater. Sci.* **1985**, 15, 329.

[167] A. Pramanick, A. D. Prewitt, J. S. Forrester, J. L. Jones, *Crit. Rev. Solid State Mater. Sci.* **2012**, *37:4*, 243.

[168] E. Breckenfeld, A. B. Shah, L. W. Martin, *J. Mater. Chem. C* **2013**, 1, 18052.

[169] J. Karthik, A. R. Damodaran, L. W. Martin, *Adv. Mater.* **2010**, 24, 1610.

[170] N. Setter, D. Damjanovic, L. Eng, G. Fox, S. Gevorgian, S. Hong, A. Kingon, H. Kohlstedt, N. Y. Park, G. B. Stephenson, I. Stolitchnov, A. K. Taganstev, D. V. Taylor, T. Yamada, S. Streiffer, *J. Appl. Phys.* **2006**, 100, 051606.

[171] G. E. Pike, W. L. Warren, D. Dimos, B. A. Tuttle, R. Ramesh, J. Lee, V. G. Keramidas, J. T. Evans, Jr. *Appl. Phys. Lett.* **1995**, 66, 484.

[172] W. L. Warren, G. E. Pike, K. Vanheusden, D. Dimos, B. A. Tuttle, J. Robertson, *J. Appl. Phys.* **1996**, 79, 9250.

[173] J.-P. Maria, J. F. Shepard Jr., S. Trolier-McKinstry, T. R. Watkins, A. E. Payzant, *Int. J. Appl. Ceram. Technol.* **2005**, 2(1), 51.

[174] G. Arlt, H, Neumann, *Ferroelectrics* **1988**, 87, 109.

[175] A. S. Nowick, W. R. Heller, *Adv. Phys.* **1963**, 12, 251.

[176] R. Balzer, H. Peters, W. Waidelich, *Phys. Rev. B* **1974**, 9, 2746.

[177] U. Robels, G. Arlt, *J. Appl. Phys.* **1993**, 73, 3454.

[178] T. Varnhorst, O. F. Schirmer, H. Kröse, R. Scharfschwerdt, Th. W. Kool, *Phys. Rev. B* **1996**, 53, 116.

[179] H. Wu, G, Chai, B. Xu, J. Li, *Appl. Phys. A* **2013**, 113, 155.

[180] A. F. Devonshire, *Philos. Mag.* **1951**, 42, 1065.

[181] D. Sun, X. Ren, K. Otsuka, *Appl. Phys. Lett.* **2005**, 87, 142903.

[182] C. J. Tsai, P. Rozenak, H. A. Atwater, T. Vreeland, *J. Cryst. Growth* **1991**, 111, 931.

[183] G. Subramanyam, M. W. Cole, N. X. Sun, T. S. Kalkur, N. M. Sbrockey, G. S. Tompa, X. Guo, C. Chen, S. P. Alpay, G. A. Rossetti, K. Dayal, L. –Q. Chen, D. G. Schlom, *J. App. Phys.* **2013**, 114, 191301.

[184] D. Dimos, C. H. Mueller, *Annu. Rev. Mater. Sci.***1998**, 28, 397.

[185] G. Subramanyam, F. Ahamed, and R. Biggers, *IEEE Microw. Wirel. Compon. Lett.* **2005**, 15, 739.

[186] J. Nath, D. Ghosh, J. P. Maria, A. I. Kingon, W. Fathelbab, P. D. Franzon, M. B. Steer, *IEEE Trans. MTT* **2005**, 53, 2707.

[187] B. Acikel, T. R. Taylor, P. J. Hansen, J. S. Speck, R. A. York, *IEEE Microw. Wirel. Compon. Lett.* **2002**, 12, 237.

[188] A. Jamil, T. S. Kalkur, and N. Cramer, *IEEE Trans. Ultrason. Ferroelectr. Freq. Control* **2007**, 54, 222.

[189] R. Slowak, S. Hoffmann, R. Liedtke, R. Waser, *Integr. Ferroelectrics* **1999**, 24, 169.

[190] M. Y. El-Naggar, K. Dayal, D. G. Goodwin, K. Bhattacharya, *J. Appl.Phys.* **2006**,100,114115.

[191] M. W. Cole, E. Ngo, S. Hirsch, J. D. Demaree, S. Zhong, S. P. Alpay, *J. Appl. Phys*, **2007**,102, 034104.

[192] G. Catalan, B. Noheda, J. McAneney, L. J. Sinnamon, J. M. Gregg, *Phys. Rev. B* **2005**, 72, 020102.

[193] J. Zhang, R. Xu, A. R. Damodaran, Z.-H. Chen, L. W. Martin, Phys. Rev. B **2014**, 89, 224101.

[194] J. V. Mantese, S. P. Alpay, *Graded Ferroelectrics, Transpacitors, and Transponents* (Springer-Verlag, Berlin, 2005).

[195] J. V. Mantese, N. W. Schubring, A. L. Micheli, A. B. Catalan, *Appl. Phys. Lett.* **1995**, 67, 721.

[196] W. Fellberg, J. Mantese, N. Schubring, A. Micheli, *Appl. Phys. Lett.* **2001**, 78(4), 524.

[197] J. V. Mantese, N. W. Schubring, A. L. Micheli, A. B. Catalan, M. S. Mohammed, R. Naik, G. W. Auner, *Appl. Phys. Lett.* **1997**, 271(14), 2047.

[198] Z. Chen, K. Arita, M. Lim, C. A. Paz De Araujo, *Integr. Ferroelectrics* **1999**, 24, 181.

[199] J. Mendiola, M. L. Calzada, P. Ramos, M. J. Martin, F. Agullo-Rueda, *Thin Solid Films* **1998**, 195, 315.

[200] L. E. Cross, *J. Mater. Sci.* **2006**, 41, 53.

[201] W. Ma, L. E. Cross, *Appl. Phys. Lett.* **2002**, 81(18), 3440.

[202] W. Ma, L. E. Cross, *Appl. Phys. Lett.* **2006**, 88(23), 232902.

[203] B. Chu, W. Zhu, N. Li, L. E. Cross, *J. Appl. Phys.* **2009**, 106(10), 104109.

[204] J. Karthik, R. V. K. Mangalam, J. C. Agar, L. W. Martin, *Phys. Rev. B* **2013**, 87, 024111.

[205] N. Sai, B. Meyer, D. Vanderbilt, *Phys. Rev. Lett* **2000**, 84, 5636.

[206] N. Choudhury, L. Walizer, S. Lisenkov, L. Bellaiche, *Nature* **2011**, 470, 513.

[207] Z.-G. Ban, S. P. Alpay, J. V. Mantese, *Phys. Rev. B* **2003**, 67, 184104.

[208] A. L. Roytburd, J. Slutsker, *Appl. Phys. Lett.* **2006**, 89, 042907.

[209] M. Marvan, P. Chvosta, J. Fousek, *Appl. Phys. Lett.* **2005**, 86, 221922.

[210] A. K. Taganstev, *Sov. Phys. JETP* **1985**, 61(6), 1246.

[211] P. Zubko, G. Catalan, A. K. Tagantsev, *Annu. Rev. Mater. Res.* **2013**, 43, 387.

[212] T. Remmel, R. Gregory, B. Baumert, *JCPDS-International Centre for Diffraction Data* **1999.**

[213] A. Basjamin, R. C. DeVries, *J. Am. Ceram. Soc.* **1957**, 40, 373.

[214] V. N. Shut, S. R. Syrtsov, V. L. Trublovsky, B. A. Strukov *Inorganic Materials*, **2011**, 47(1), 87.

[215] W. Merz, *Phys. Rev.* **1949**, 77(7), 52.

[216] P. Günther, K. Dransfeld, *Appl. Phys. Lett.* **1992**, 61, 1137.

[217] A. Gruverman, O. Auciello, H. Tokumoto, *Annu. Rev. Mater. Sci.* **1998**, 28, 101.